

INFORMATION TO USERS

This manuscript has been reproduced from the microfilm master. UMI films the text directly from the original or copy submitted. Thus, some thesis and dissertation copies are in typewriter face, while others may be from any type of computer printer.

The quality of this reproduction is dependent upon the quality of the copy submitted. Broken or indistinct print, colored or poor quality illustrations and photographs, print bleedthrough, substandard margins, and improper alignment can adversely affect reproduction.

In the unlikely event that the author did not send UMI a complete manuscript and there are missing pages, these will be noted. Also, if unauthorized copyright material had to be removed, a note will indicate the deletion.

Oversize materials (e.g., maps, drawings, charts) are reproduced by sectioning the original, beginning at the upper left-hand corner and continuing from left to right in equal sections with small overlaps. Each original is also photographed in one exposure and is included in reduced form at the back of the book.

Photographs included in the original manuscript have been reproduced xerographically in this copy. Higher quality 6" x 9" black and white photographic prints are available for any photographs or illustrations appearing in this copy for an additional charge. Contact UMI directly to order.

U·M·I

University Microfilms International
A Bell & Howell Information Company
300 North Zeeb Road, Ann Arbor, MI 48106-1346 USA
313/761-4700 800/521-0600

Order Number 9209699

**A theoretical study of magnetosphere-ionosphere coupling
processes**

Cao, Fei, Ph.D.

University of Alaska Fairbanks, 1991

U·M·I

300 N. Zeeb Rd.
Ann Arbor, MI 48106

**A THEORETICAL STUDY OF MAGNETOSPHERE-
IONOSPHERE COUPLING PROCESSES**

**A
THESIS**

**Presented to the Faculty of the University of Alaska
in Partial Fulfillment of the Requirements
for the Degree of**

DOCTOR OF PHILOSOPHY

**By
Fei Cao, B.S., M.S.**


Fairbanks, Alaska

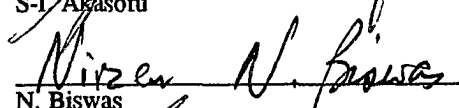
September, 1991

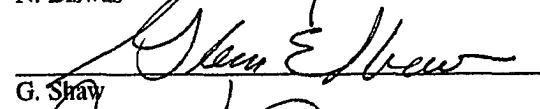
**A THEORETICAL STUDY OF MAGNETOSPHERE-
IONOSPHERE COUPLING PROCESSES**

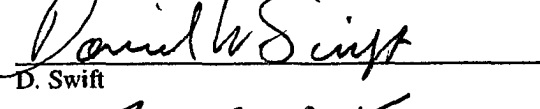
By
Fei Cao

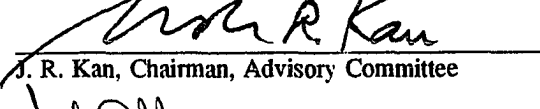
RECOMMENDED:

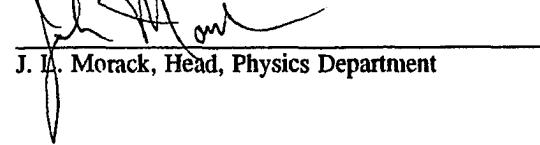

S-I Akasofu


N. Biswas



G. Shaw

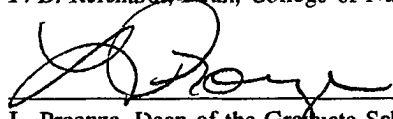

D. Swift


J. R. Kan, Chairman, Advisory Committee


J. L. Morack, Head, Physics Department

APPROVED:


P. B. Reichardt, Dean, College of Natural Sciences


L. Proenza, Dean of the Graduate School

8/1/91
Date

ABSTRACT

Magnetosphere and ionosphere are coupled electrodynamically by waves, field-aligned currents and parallel electric fields. Several fundamental coupling processes are addressed in my thesis. It is shown that the Alfvén wave is the dominant mode in transmitting field-aligned currents. Therefore, dynamic M-I coupling can be modeled by the Alfvén wave bouncing between the ionosphere and the magnetospheric boundaries. The open magnetopause, separating the solar wind and the magnetosphere, behaves like a near perfect reflector to the Alfvén wave because of the large solar wind inertia. At the plasma sheet, however, the reflection coefficient may extend over a wide range, depending on the location in the plasma sheet. As the Alfvén wave propagates back and forth between the magnetosphere and ionosphere, the field-aligned current density increases dramatically at certain locations, especially near the head of the westward traveling surge, causing potential drops to develop along magnetic field lines. It is found that the existence of parallel potential drops can distort the global convection pattern and limit the upward field-aligned current. The magnetic reconnection at the dayside magnetopause is responsible for enhancing the convection in the magnetosphere, which subsequently propagates toward the ionosphere by the Alfvén wave. The patchy and intermittent reconnection at the dayside magnetopause can be initiated by the 3-D tearing instability, leading to the isolated magnetic islands and X-line segments. The nonlinear evolution of tearing in terms of the magnetic island coalescence is also studied.

TABLE OF CONTENTS

	Page
Abstract	iii
Table of Contents	iv
List of Figures	vi
Acknowledgments	viii
1. Introduction	1
1.1 Background	3
1.2 This Work	8
2. Field-Aligned Currents in Hydromagnetic Waves	11
2.1 Ideal MHD Waves	12
2.2 Finite Wavelength Hydromagnetic Waves	17
2.3 Discussion and Summary	29
3. Reflection of Alfvén Waves From the Magnetosphere	32
3.1 Reflection of Alfvén Waves at an Open Magnetopause	33
3.1.1 Introduction	34
3.1.2 A Parameterized Open Magnetopause	37
3.1.3 Reflection and Transmission Amplitude Ratios	45
3.1.4 Summary	53
3.2 Reflection of Alfvén waves From the Plasma Sheet	54
4. Effect of Field-Aligned Potential Drops on the Magnetosphere-Ionosphere Coupling	61
4.1 Basic Equations	62
4.2 Local Effect of Field-Aligned Potential Drops	65
4.3 Global Effect of Field-Aligned Potential Drops	67
4.4 Discussion and Summary	80

5. A 3-D Tearing Model for the Dayside Reconnection	82
5.1 Introduction	82
5.2 Oblique Resistive Tearing of a Thin Current Sheet	86
5.2.1 Basic Equations	86
5.2.2 Numerical Results	91
5.3 Implications for Patchy and Intermittent Reconnection	102
5.4 Discussion and Summary	106
6. Coalescence of Magnetic Islands Created by Tearing Modes	109
6.1 Introduction	111
6.2 Tearing and Coalescence Instabilities	113
6.3 Coalescence of Magnetic Islands Created by Tearing Modes	123
6.4 Discussion and Summary	132
7. Discussions and Conclusions	136
Appendix A: Two-Fluid Equations and Dispersion Relation	144
Appendix B: Numerical Scheme for the Initial Value Problem	147
References	151

LIST OF FIGURES

		Page
Fig. 1.1	Schematic view of the structure of the magnetosphere [NASA]	2
Fig. 1.2	Large-scale pattern of the major field-aligned current systems observed by the Triad satellite	5
Fig. 1.3	Empirical convection pattern at the ionospheric heights	7
Fig. 2.1	Polar plots of phase velocities in the k - β parameter space	22
Fig. 2.2	Polar plots of field-aligned currents	24
Fig. 2.3	Polar plots of the group velocity	27
Fig. 2.4	Polar plots of compressibility	28
Fig. 3.1	Configuration of the magnetopause and coordinate system	36
Fig. 3.2	Dependence of reflection and transmission amplitude ratios on the magnetosphere-solar wind density ratio	47
Fig. 3.3	Dependence of reflection and transmission amplitude ratios on β_1 (the solar-wind thermal pressure to magnetic pressure ratio)	49
Fig. 3.4	Dependence of reflection and transmission amplitude ratios on the incident angles of Alfvén waves	52
Fig. 3.5	Reflection of Alfvén waves from the central plasma sheet	56
Fig. 4.1	Results of M-I coupling without the field-aligned potential drop	69
Fig. 4.2	Results of M-I coupling powered by a constant current generator for $\Phi_{ } \neq 0$	72
Fig. 4.3	Same as Fig. 4.2, but for $\alpha = 10 \text{ kV}/(\mu\text{A}/\text{m}^2)$	75
Fig. 4.4	Results of M-I coupling powered by a constant voltage generator for $\Phi_{ } \neq 0$	77
Fig. 4.5	Same as Fig. 4.4, but for $\alpha = 10 \text{ kV}/(\mu\text{A}/\text{m}^2)$	78

Fig. 5.1	Geometrical configuration of a magnetic reversal layer and the coordinate system	83
Fig. 5.2	The normalized growth rate $\nu\tau_A$ as a function of $\tan\theta$ for several Hall coefficients $h = l_i/\Delta = 0, 0.25, 0.5, 1., 1.5$	92
Fig. 5.3	The normalized phase velocity $\omega/(kV_A)$	94
Fig. 5.4	The normalized growth rate $\nu\tau_A$ as a function of $\tan\theta$ for several Lundquist numbers $S = 100, 500, 1000, 2000$	97
Fig. 5.5	Magnetic field lines and B_Y components for several values of h and $\tan\theta$	99
Fig. 5.6	Stream lines and V_Y components	101
Fig. 5.7	Tearing instability in a finite system	102
Fig. 5.8	3-D magnetic island structure produced by a tearing wave packet	104
Fig. 6.1	Three possible magnetic field typologies	110
Fig. 6.2	A sketch of a single magnetic island	114
Fig. 6.3	Equilibrium flux surfaces and current distributions	118
Fig. 6.4	Nonlinear evolution of flux surfaces	120
Fig. 6.5	The magnetic island structure associated with the tearing and coalescence instabilities	121
Fig. 6.6	Results of the magnetic island coalescence	129
Fig. 6.7	Magnetic islands and flow patterns associated with $\psi_t \sim -\cos kz$ and $\tilde{\psi}_{1/2} \sim \cos kz/2$ tearing modes	131
Fig. 7.1	Schematic view of the magnetosphere and the summary diagram of research domains	137

ACKNOWLEDGMENTS

It was nothing less than a thrill to finally get this thesis done and send it to the advisory committee. As you may expect, a Ph.D. thesis like this one takes a great deal of work. My thesis is an accumulation of five years of research and study in the Geophysical Institute, University of Alaska.

Like most Ph.D theses, my thesis took long hours, commitment, and special attention from many people. I'd like to take a moment to thank everyone who helped make my Ph.D project possible— I couldn't have done it without them.

The person most responsible for the inception and the guidance I received throughout my graduate study is Prof. J. R. Kan, my thesis adviser and chairman of my advisory committee. He has not only provided the financial and academic support for my prolonged study, but has also taught me a lot about the way of doing research. He has spent a great deal of time editing and vastly improving my writing since I came here as a foreign student. His invaluable help is deeply appreciated and places him apart from others. Many efforts on his part went far beyond the call of duty to help me toward a Ph.D. degree. None of the efforts that went into this thesis would have been possible without his support.

I would like to take this chance to thank the other committee members: S. Akasofu, N. Biswas, G. Shaw and D. Swift for their help and constant encouragement in carrying through my Ph.D project. I particularly thank Prof. D. Swift, who carefully reviewed the original draft of my thesis with valuable suggestions for improvements. Prof. L. Lee and Prof. G. Gislason served as the members of my advisory committee in the early years of my graduate study, Prof. E. Wescott and Prof. P. X. Quang acted as outside examiners. I would also like to record my gratitude to them.

My work has been primarily supported by The National Science Foundation. Most of my computation and printing jobs were done on UAF VAX computer and were generously supported by the University of Alaska. It is my pleasure to thank everyone in the UAF computer center, for providing excellent services. I thank Ms. L. Y. Lyu for introducing me to the fantastic Macintosh world. Some of the figures in this thesis were produced through the Apple Macintosh. Thanks are also due to C. Rohwer and D. Miller for their help in solving the computer related problems.

Finally, I am grateful to Prof. Z. F. Fu and Prof. K. K. Zhu, whose original encouragement resulted in my studying in the United States and becoming firmly committed to the Space Physics research.

This thesis was typeset using Donald Knuth's \TeX , a wonderful computer typesetting language.

CHAPTER 1

Introduction

The magnetosphere-ionosphere (M-I) coupling is one of the main subjects in space research. Continuous emission of plasma from the sun is now well established and it has been designated as the *solar wind*. As the Earth's magnetic field prevents the access of the solar wind toward the Earth, a cavity is formed around the Earth in the domain of the streaming solar plasma. The cavity, inside which field lines of the earth's magnetic field are confined, is called the *magnetosphere* of the Earth. The bounding surface of the magnetosphere, which separates the solar wind and the geomagnetic field, is defined as the *magnetopause*. The magnetic field in the magnetosphere can be traced back to the Earth as illustrated in Figure (1.1). Near the Earth, the mixture of the high-ionized and the neutral particles in the atmosphere forms a region of maximum electric conductivity transverse to the geomagnetic field lines caused by numerous ion-neutral collisions. This highly conducting region is referred to as the *ionosphere*, where the natural attractive drama *Aurora* is played. Aurora is simply a result of light emitted from excited atmospheric atoms and molecules due to bombardment of hot electrons and protons that precipitate down into the ionosphere from the magnetosphere along magnetic field lines.

It is clear that energy flow in the M-I system is primarily from the solar wind to the magnetosphere and then to the ionosphere. However the ionosphere is not a passive element in this system. The spatial distribution of ionospheric conductivity affects magnetospheric plasma transport and the configuration of the magnetospheric current systems. This interaction between the magnetosphere and the ionosphere (M-I) is important for many phenomena such as substorms, magnetospheric plasma convection, and the formation of auroral structures. This

introduction begins with some background information and the physical picture of the time-dependent magnetosphere and ionosphere coupling by the bouncing of Alfvén waves. Then, a description of the content of the remainder of this thesis will be given.

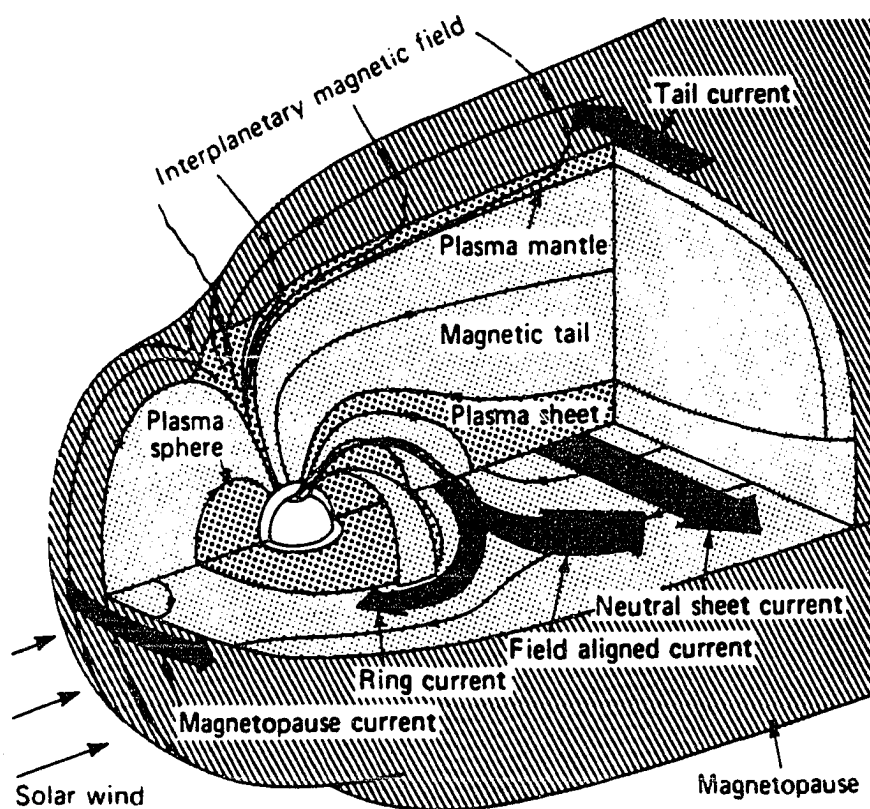


Figure 1.1 Schematic view of the structure of the magnetosphere [NASA].

1.1 Background

The coupling between the magnetosphere and ionosphere is caused by the normally high conductivity along the geomagnetic field lines that connect these regions. The ionosphere is the region consisting of both ionized and neutral particles and is characterized by numerous ion-neutral collisions. The plasma in the magnetosphere, where the density is extremely low compared with that in the ionosphere, is characterized by collision-free charged particle motion. The magnetosphere-ionosphere coupling is the interaction of different physical processes occurring in regions that are often considered as spatially separated.

Dungey [1961] noted that the existence of the magnetic field in the solar wind implies that the magnetic field lines from the Earth may be directly connected to the magnetic field in the solar wind by a process of reconnection. Through the reconnection process, solar wind energy and momentum can gain an entry directly into the magnetosphere to induce the magnetospheric convections. The plasma motion in the magnetosphere relative to the conducting ionosphere generates a magnetic shear stress that acts to reduce the relative motion. Corresponding to the magnetic stress, the field-aligned current is required to flow back and forth along the geomagnetic field that connects the two regions. As a result, the convection in the ionosphere is finally established according to the magnetospheric convection. In this sense, it can be said that the coupling between the magnetosphere and the ionosphere is carried out through the flow of field-aligned currents.

The large-scale field-aligned currents are expected to propagate along the magnetic field lines through the Alfvén wave. The Alfvén wave, which is well guided along field lines and associated with a significant field-aligned current, is known to play a major role in the time-dependent M-I coupling process. As proposed by Kan and Sun [1985], the time-dependent

M-I coupling can be modeled with the bouncing Alfvén waves known as Pi2 pulsation phenomenon. The enhanced magnetospheric convection due to the dayside magnetic reconnection can lead to launching an Alfvén wave toward the ionosphere. When the Alfvén wave enters the ionosphere, it will be partially reflected; this reflection is determined by matching the field-aligned current density of the wave to the field-aligned current density due to the divergence of the current driven in the ionosphere by the electric fields of the incident and reflected waves. The Alfvén wave reflected from the ionosphere will subsequently be reflected from the magnetospheric source region. The source region of the enhanced magnetospheric convection will be assumed to be located (1) on open field lines at the high-latitude magnetopause and (2) on closed field lines in the plasma sheet. During the transient state the Alfvén wave is damped at each reflection from the ionosphere. Successive ionospheric reflection of the Alfvén waves can produce damped oscillations in the auroral electrojet which lead to the Pi2 pulsation signature observed on the ground. As the Alfvén waves bounce back and forth between the magnetosphere and the ionosphere, the ionospheric convection is established and the field-aligned current density increases to meet with the enhanced magnetospheric convection. The large downward electron flux associated with the upward field-aligned currents can cause a parallel potential drop along the magnetic field lines. The parallel potential will further accelerate the energetic electrons associated with the upward field-aligned current. The bombardment of the precipitation of the energetic electron flux leads to enhancement of ionospheric conductivity and brightening of the curtain-like aurora, known as the *discrete* aurora.

The average large-scale patterns of ionospheric convections and field-aligned currents, based on the observation data, are now well established. The connection of the field-aligned current characteristics with the orientation of the solar wind magnetic field, substorm phases, and convective electric fields are also generally known. Figure (1.2) shows the statistical features of the large-scale field-aligned currents [Iijima and Potemra, 1976]. Figure (1.3)

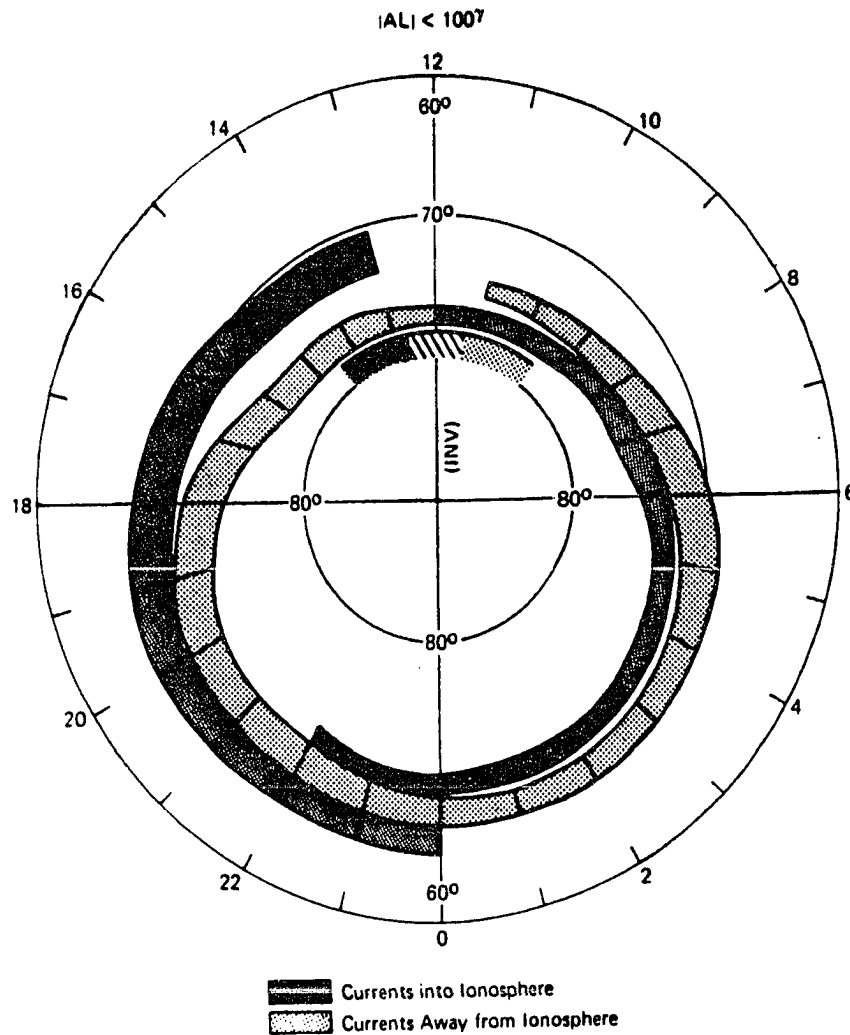


Figure 1.2 Large-scale pattern of the major field-aligned current systems observed by the Triad satellite. The principal feature of this plot is the distinguished current systems. The circumpolar region 1 field-aligned current lies poleward of the neighboring region 2 current, and the cusp current system occurs in the region spanning 10-14 hours L.T. (from Iijima and Potemra, 1976).

shows the typical convection pattern [Heppner, 1977]. The convection pattern normally has two cells with antisunward flow in the polar cap and sunward flow at lower latitudes near the auroral oval. The simple configurations shown in Figures (1.2) and (1.3) apply mainly to the large-scale and statistical features. Some characteristic features of dynamic and auroral-arc scale events associated with substorms have not been fully delineated.

On the theoretical side, much modeling has been done successfully on the ionospheric end of the magnetosphere-ionosphere system [e.g., Vasyliunas, 1970; Nisbet *et al.*, 1978; Kamide and Matsushita, 1979; Kan and Kamide, 1985]. They solve the equation of ionospheric current conservation, given models for the distributions of ionospheric conductivity and field-aligned current. To treat the magnetospheric and ionospheric coupling self-consistently, one has to include the magnetospheric dynamics in response to the ionospheric activities. A number of theoretical models have been developed to deal with the self-consistent M-I coupling [Vasyliunas, 1972; Wolf, 1975; Harel *et al.*, 1981a and 1981b; Kan and Sun, 1985; Rostoker and Eastman, 1987; Lotko *et al.*, 1987; Kan *et al.*, 1988]. Despite these efforts, none of these models is widely accepted as a global dynamic model. Dynamic, time-dependent effects are important in establishing the relationships among the regions of field-aligned current, convection field and enhanced conductivity. The time-dependent M-I coupling model developed by Kan and Sun [1985] is successful in illuminating the physics of substorm-related phenomena. However, their model has still not become quantitative in complete form, due partly to their ignorance about the detailed physics of the magnetosphere. The dynamic M-I system is extremely complicated and many outstanding issues are still unsolved. One of our interests in this thesis is to deal with two issues in M-I coupling: the reflection of Alfvén waves from the magnetospheric source region and the field-aligned potential drops in the M-I coupling. Due to the complexity of the magnetospheric structure and lack of a well-developed theory or an observational model of the magnetospheric source regions, it is difficult to determine the interaction of the Alfvén wave

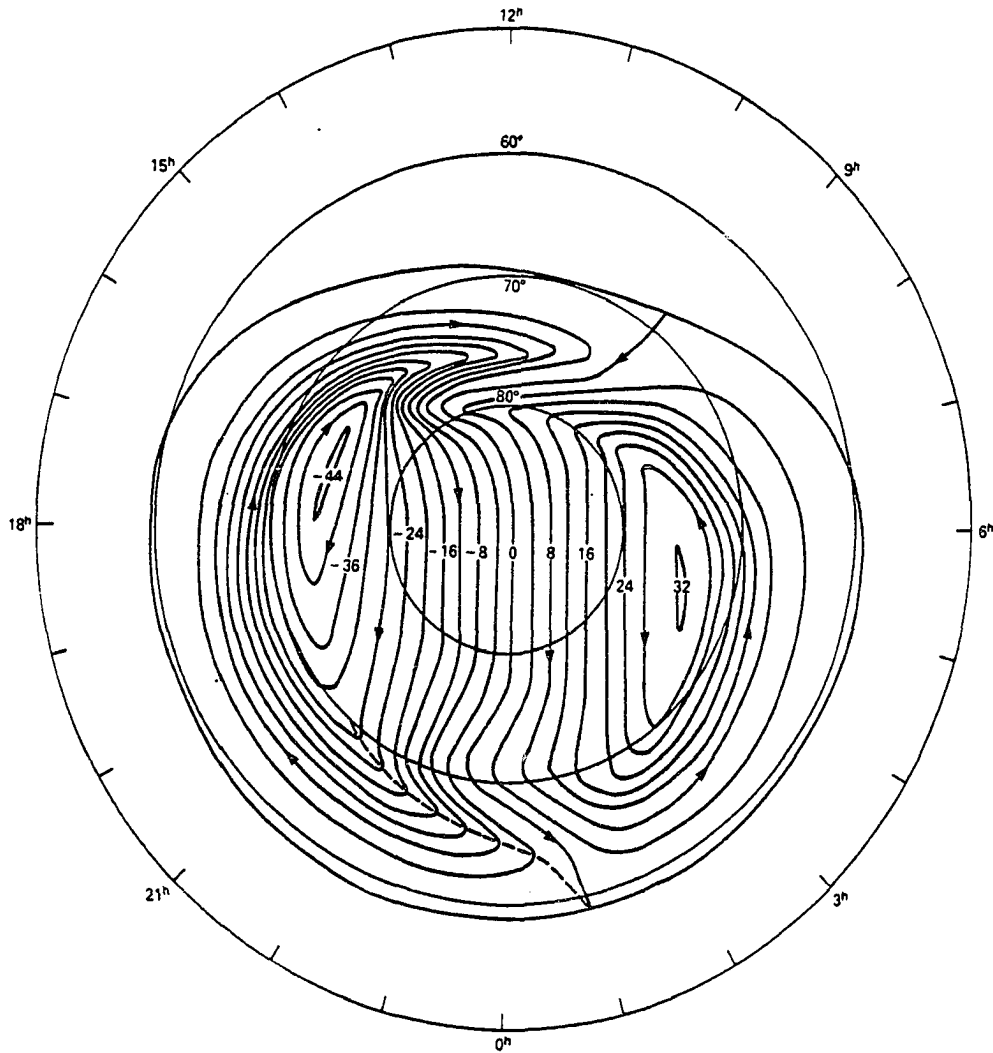


Figure 1.3 Empirical convection pattern at the ionospheric heights (from Hopper, 1977).

with the magnetospheric source regions. With some simplified models, the reflection of the Alfvén waves from the magnetosphere is quantitatively determined in this thesis. The field-aligned currents that achieve the long-range transfer of shear stresses from the magnetospheric boundary to the ionosphere may be limited by the set-up of field-aligned potential drops. It is very interesting to know what is the effect of the field-aligned potential drops on the global M-I coupling.

The magnetic reconnection is responsible for the direct entry of the solar wind energy to the M-I system and sets up the magnetospheric convection. In spite of the extensive studies, the reconnection process is yet far from being completely understood. There is much evidence of a transient nature of the reconnection process [Paschmann *et al.*, 1976; Russell and Elphic, 1978; Haerendel *et al.*, 1978; Russell and Elphic, 1979] and the term *intermittent and patchy* reconnection has been introduced. The understanding of this process has not advanced far enough as to explain why in the real world reconnection should exist at all. The large-scale spontaneous reconnection may develop by the tearing mode instability of a reversal magnetic field configuration and grow through coalescence of magnetic islands [Finn and Kaw, 1977]. However, there seems to exist no simple mechanism for the coalescence of magnetic islands created by the tearing mode. Some misleading concepts have prevailed for such a long time that it is necessary to get them clarified.

1.2 This Work

My thesis deals largely with some unsolved issues in the theoretical study of M-I coupling. The main work in this thesis consists of five chapters. Each of the chapters covers a specific topic.

Chapter 2 introduces the finite-wavelength effect on field-aligned currents in hydromagnetic waves. Within the MHD approximation in which the plasma dispersion lengths are much smaller than the wave length, the Alfvén mode is the only hydromagnetic wave mode in which the field-aligned current can be nonzero. When the wavelength is comparable to the ion inertial length or the ion gyroradius, it is found that there exist the field-aligned currents in the fast and slow modes and the compressibility in the Alfvén mode. These results are useful in understanding the time-dependent field-aligned current sheets associated with auroral arcs with thickness down to the ion inertial length or ion gyroradius.

Chapter 3 contains a quantitative study of Alfvén wave reflection from the magnetospheric boundaries. I have investigated the reflection of the Alfvén waves incident on the open magnetopause and the plasma sheet from the magnetospheric side. The open magnetopause including the plasma mantle is described as a parameterized discontinuity. The results show that the electric fields of reflected Alfvén wave are mainly controlled by the magnetosphere-solar wind density ratio and the bending of magnetic field lines. Under conditions representing the open magnetopause, it turns out that the open magnetopause behaves like a near perfect reflector. The corresponding reflection amplitude coefficient for the wave electric fields can be approximated by $R_E = E^r/E^i \approx -1$. Reflection of the Alfvén from the plasma sheet is largely due to the field line curvature near the Equator. In the near-Earth plasma sheet, where the field lines are less bent near the Equator, the Alfvén wave can propagate through the plasma sheet without reflection. As the field lines in the plasma sheet become increasingly distended toward the magnetotail, the Alfvén wave must negotiate the strong field curvature, leading to a total reflection.

Chapter 4 brings up a steady global magnetosphere-ionosphere coupling model including the effect of field-aligned potential drop. Specifically I examine the effects of field-aligned potential on the convection pattern, the field-aligned current distribution and the ionospheric

conductance in a self-consistent calculation under the assumption of either a constant current generator or a constant voltage generator.

Chapter 5 describes a three-dimensional tearing mode for the dayside reconnection that is responsible for the entry of solar wind energy into the magnetosphere. The enhanced magnetospheric convection, which leads to launching of Alfvén waves toward the ionosphere, is established and maintained by the dayside reconnection between the solar wind and geomagnetic fields. In this chapter, the results of the oblique resistive tearing in a thin current sheet are presented. Implications of these results on the patchy and intermittent reconnection of the finite-size current sheet at the dayside magnetopause and on the M-I coupling, are discussed.

Chapter 6 discusses the nonlinear tearing development in terms of island coalescence. I focus on the basic mechanisms for the tearing instability, the coalescence instability and the coalescence of the tearing-generated islands. The results will be compared with the MHD and particle simulations. In this chapter, I attempt to clear up some misleading concepts and puzzles in the tearing-reconnection studies.

Chapter 7 summarizes the principal results of this thesis. Appendix A is relevant to the material of Chapters 2 and 5. In this appendix, the two-fluid equations and the general dispersion relation for all frequency and wavelength are derived. Finally, Appendix B contains a description of the algorithm upon which the numerical calculation in Chapter 5 is based.

CHAPTER 2

Field-Aligned Currents in Hydromagnetic Waves

Generation of field-aligned currents in magnetized plasmas is an issue of fundamental importance in space physics. Several authors have addressed this important problem based on the momentum equation and the current conservation law [Vasyliunas, 1970, 1984; Boström, 1975; Sato and Iijima, 1979; Hasegawa and Sato, 1980; Sonnerup, 1980; Troshichev, 1982; Kan, 1987].

The importance of the field-aligned currents arises in the magnetosphere and ionosphere coupling where the plasma of the magnetosphere is found in the motion relative to the conducting ionosphere. The magnetic field plays the role of an elastic medium in MHD and a magnetic shear stress is generated which acts to reduce the relative motion. In order that the magnetic shear force acts equally and oppositely in the two plasmas, the associated electrical current must link both bodies. The current is therefore required to flow back and forth parallel to the magnetic field that connects the two regions. A fundamental approach to understanding the generation of time-dependent field-aligned currents would be to start from a study of field-aligned currents associated with hydromagnetic waves. These propagation waves may be attached to one or the other or both of the coupled plasmas. It can be easily shown, under the MHD approximation, that field-aligned currents are identically zero in the fast and slow waves. This means the time-dependent field-aligned current can propagate only by Alfvén waves in the MHD approximation. Since the MHD Alfvén wave is incompressible, field-aligned currents in Alfvén waves are independent of the plasma pressure. This is in contrast to the steady state field-aligned current generated in the plasma sheet from the plasma pressure gradient [e.g., Vasyliunas, 1970, 1972; Southwood, 1977; Harel *et al.*, 1981a, b; Wolf *et al.*, 1982; Karty *et*

al., 1983]. This apparent conflict raises a question about the assumption commonly made in the magnetosphere-ionosphere coupling models that the Alfvén waves are solely responsible for initiating and transmitting the field-aligned currents [Maltsev *et al.*, 1974; Miura and Sato, 1980; Goertz and Boswell, 1979; Lysak and Dum, 1983; Kan and Sun, 1985].

The purpose of this chapter is to determine under what condition and to what extent the time-dependent field-aligned current and the plasma pressure are related. By means of the two-fluid equation, it is shown that the finite-ion-inertial-length (FIIL) and the finite-ion-temperature (FIT) effects are responsible for the field-aligned currents in the fast and slow modes and for the compressibility in the Alfvén mode. Individually, these results are by no means new from the linear wave point of view; in the context of time-dependent field-aligned currents, they improve our understanding of the thin auroral field-aligned current sheet [Sugiura *et al.*, 1983] down to the ion gyroradius scale embedded in the large scale region I and region II field-aligned currents [Iijima and Potemra, 1976].

In the first part of this chapter I shall present the basic properties associated with ideal MHD waves. The second section will discuss the field-aligned current and the compressibility of the finite-wavelength hydromagnetic waves, whose wavelengths are comparable to the ion inertial length and the gyroradius. The third section will summarize the principal results of this chapter.

2.1 Ideal MHD Waves

It is well known that there exist three fundamental modes of wave propagation in plasmas involving low-frequency ion oscillations in the presence of a magnetic field. Under the infinite conductivity assumption, the magnetic field lines will move with the plasma. The plasma particles thus bound to the magnetic field lines provide an added inertia, which lowers the

frequency of an electromagnetic oscillation of the given wavelength. The magnetic forces are equivalent to a magnetic pressure $B^2/8\pi$, combined with a tension $B^2/4\pi$ along the field lines. The restoring force of an Alfvén wave is derived solely from the shear tension $B^2/4\pi$ of the magnetic field lines. Analogy with the theory of stretched strings suggests that this tension may lead to the transverse waves along the field lines, with a velocity V_A given by

$$V_A = \sqrt{\frac{B^2}{4\pi\rho}} \quad (2.1)$$

where ρ is the mass density of the fluid. The possibility of such a wave was first established by Alfvén in 1942. The wave is now known as the shear (or intermediate) Alfvén wave with a linear dispersion $\omega/k = V_A \cos \theta$ where θ is the angle between the wavevector \mathbf{k} and the background field \mathbf{B}_0 . The Alfvén wave is incompressible and transverse in nature since the plasma displacement is always perpendicular to the direction of wave propagation and thus does not compress the plasma.

The other two modes of propagation are associated with the compressibility and are given by the upper and lower signs of the dispersion relation [e.g., Stringer, 1963; Formisano and Kennel, 1969]

$$V_{F,S}^2 = \frac{\omega^2}{k^2} = \frac{1}{2} \left\{ (C_S^2 + V_A^2) \pm \sqrt{(C_S^2 + V_A^2)^2 - 4C_S^2 V_A^2 \cos^2 \theta} \right\} \quad (2.2a)$$

where $C_S = \sqrt{\gamma P_0/\rho_0}$ is the sound speed, V_A defined in (2.1) is the Alfvén speed and θ is the angle between the equilibrium magnetic field direction and the wave propagation direction. In the short perpendicular wavelength limit ($\cos^2 \theta \ll 1$), the dispersion relation (2.2a) may be simplified to the following

$$\begin{aligned} V_F &= \sqrt{C_S^2 + V_A^2} \\ V_S &= \frac{C_S V_A}{C_S^2 + V_A^2} \cos \theta = C_{SL} \cos \theta \end{aligned} \quad (2.2b)$$

where $C_{SL} = C_S V_A / (C_S^2 + V_A^2)$ is the slow mode speed. The incompressible Alfvén wave

induces a shear of the magnetic field lines without changing the field magnitude. In comparison, the compressional waves do have a component B parallel to the background field B_0 and the compression of the magnetic field lines contributes to the restoring force along with the kinetic pressure. The mode with a fast speed given by the upper signs in (2.2a) is known as the fast magnetosonic wave, in which the plasma and magnetic pressures vary in the same phase and act together as a restoring force. The mode with the lower signs is known as the slow magnetosonic wave, in which the plasma pressure varies out of phase with the magnetic pressure.

The most striking property of the Alfvén wave is that its group velocity is in one direction only and along the magnetic field lines. Thus, the Alfvén wave suffers no geometric attenuation with distance, i.e., it does not spread out three-dimensionally around a source of disturbance that leads to a spherical attenuation. Moreover, the densities in the earth's magnetosphere are so low that attenuation due to collisional effects becomes negligible over relevant length scales. The discovery of Alfvén waves in an incompressible medium is also a very important and highly interesting phenomenon since the energy can be transmitted without large-scale exchanges of the fluid elements. The field-aligned current results from the shear magnetic stress. It is readily shown that the only MHD wave capable of initiating and propagating an electrical current parallel to the magnetic field is the Alfvén wave. Therefore, the Alfvén wave, which is incompressible, well guided along field lines and associated with a large shear magnetic field, can be recognized as the dominant mode in transporting energy from the magnetosphere to the ionosphere and plays a major role in the time-dependent large-scale magnetosphere-ionosphere coupling.

Field-aligned Current

The field-aligned current initiated by an Alfvén wave can be readily expressed in terms of the electric field [e.g., Kan *et al.*, 1982; Kan and Sun, 1985]. It is well known that the fluid velocity \mathbf{V} and the shear magnetic field \mathbf{b} of a nonlinear Alfvén wave related by [Alfvén and Falthammar, 1963]

$$\mathbf{V} = \pm \frac{\mathbf{b}}{\sqrt{4\pi\rho_0}} \quad (2.3)$$

where the plus sign is for propagation antiparallel to \mathbf{B}_0 , and minus sign is for parallel propagation. ρ_0 is the mass density assumed uniform. The electric field of an Alfvén wave is given by the frozen-in condition $\mathbf{E} = -\mathbf{V} \times \mathbf{B}_0/c$. The nonlinear Alfvén wave solution in (2.3) is identical to the linear solution except the circular-polarization requirement imposed on the nonlinear Alfvén wave. Taking curl of (2.3) yields the current density of the Alfvén wave

$$\mathbf{J}_A = \pm \Sigma_A [-\hat{\mathbf{e}}_B (\nabla \cdot \mathbf{E}) + (\hat{\mathbf{e}}_B \cdot \nabla) \mathbf{E}] \quad (2.4)$$

where $\hat{\mathbf{e}}_B = \mathbf{B}_0/B_0$, $\Sigma_A = c^2/(4\pi V_A)$ is the characteristic conductance of the plasma seen by the Alfvén wave. The first term in (2.4) is the field-aligned current in the Alfvén wave ($J_{\parallel A} = \mp \Sigma_A \nabla \cdot \mathbf{E}$), and the second term is the polarization current flowing across field lines along the wave front. $\nabla \cdot \mathbf{J}_A = 0$ from (2.4) indicates that the field-aligned current of the Alfvén wave is self-consistently closed across field lines by the polarization current along the wave front. The sense of the currents with respect to the perturbation electric field depends on the propagation direction of the wave. As a result, it should be pointed out that (2.4) holds separately for each of the two possible propagation directions. If $\nabla \cdot \mathbf{E}$ is seen as an accumulated charge density, the generation of Alfvén waves in the magnetosphere and ionosphere coupling process can be understood as a discharge process and the field-aligned current initiated by the Alfvén wave is simply due to the flow of charge along the field lines.

Reflection and Transmission

The propagation and properties of the ideal Alfvén wave in the previous discussion are for a constant uniform magnetic field. In many cases, however, the magnetic field, though constant in time, is not uniform, and the magnetic field lines are in general not straight lines. The question then naturally arises in the magnetosphere and ionosphere coupling as to how the transverse electric fields and associated field-aligned sheet currents of Alfvén waves propagate along a magnetospheric flux tube that consists of the magnetic field lines.

The perturbation electric field is perpendicular to the magnetic field and field-aligned sheet currents flow at its two edges. These field-aligned currents flow to supply the polarization current associated with the Alfvén wave within the flux tube. By integrating $J_{\parallel A} = \mp \Sigma_A \nabla \cdot \mathbf{E}$ perpendicular to the field lines, the field-aligned sheet currents I flowing at the boundaries are related to the transverse wave electric field E by the wave Ohm's law

$$I = \Sigma_A E \quad (2.5)$$

where Σ_A is wave conductance as defined in Equation (2.4). As the wave propagates, the flux tube within which it is confined changes its cross section. This geometrical effect influences the magnitudes of the electric field and sheet current by the usual mapping process. The Alfvén speed also varies owing to changes in plasma density and magnetic field. The Alfvén wave conductance Σ_A , which is inversely proportional to the local Alfvén speed, is a function of position along the flux tube. When the coupling between Alfvén waves and the compressional waves due to the plasma nonuniformity is neglected, the propagation of an Alfvén wave along the magnetic flux tube is the same as that in transmission line theory. The reflection and transmission coefficients in this transmission line theory can be calculated for a given distribution of Alfvén wave conductivity Σ_A [Mallinckrodt and Carlson, 1978].

For simplicity, we consider here reflection and transmission of an Alfvén wave incident on a discontinuity that separates two magnetized uniform plasmas with the wave conductance Σ_{A1} and Σ_{A2} . The boundary conditions require the continuity of the total electric field and the total field-aligned current. These boundary conditions combined with the wave Ohm's law (2.5) gives the following reflection coefficient R_E and the transmission coefficient T_E of the wave electric field E

$$R_E = \frac{\Sigma_{A2}/\Sigma_{A1} - 1}{\Sigma_{A2}/\Sigma_{A1} + 1} \quad (2.6)$$

$$T_E = \frac{2}{\Sigma_{A2}/\Sigma_{A1} + 1} \quad (2.7)$$

where the incoming Alfvén wave is assumed to be incident on the discontinuity from the side 2.

If the magnetic field line rotates across the discontinuity, the bending of magnetic field lines will couple the incompressible Alfvén wave to the compressional waves, so that the propagation of an Alfvén wave along a curved magnetic field line is usually no longer analogous to the transmission line theory. In chapter 3, I shall further discuss the reflection and transmission of Alfvén waves at the open magnetopause and the plasma sheet, where the magnetic field lines are sharply bent due to the existence of the current sheets.

2.2 Finite Wavelength Hydromagnetic Waves

When the wavelength becomes comparable to the ion inertial length or the ion gyroradius, ions can no longer follow the magnetic line of force, whereas electrons are still attached to the field line because of their small gyroradius. The finite-ion-inertial-length (FIIL) and the finite-ion-temperature (FIT) effects on hydromagnetic waves are fully retained in the kinetic dielectric tensor derived from the Vlasov equation [e.g., Stix, 1962] from which the kinetic Alfvén waves can be derived [Hasegawa and Uberoi, 1982]. On the other hand the FIIL

and FIT effects on hydromagnetic waves can be approximated by the guiding-center dielectric tensor derived from a guiding-center Vlasov equation [Fejer and Kan, 1969]. The FIIL and FIT effects will not only modify the phase velocity, but will also introduce a weak Landau damping in oblique Alfvén waves [Stepanov, 1958; Fejer and Kan, 1969; Stéfant, 1970; Hasegawa and Uberoi, 1982; Gary, 1986]

The two-fluid equations exclude the Landau damping but retain the FIIL and FIT effects in hydromagnetic waves as have been shown by Formisano and Kennel [1969]. For studying the field-aligned currents in the finite-wavelength (FW) hydromagnetic waves, we follow Formisano and Kennel [1969] using the two-fluid plasma equations in the following discussion. In this sense, the present study is an extension of the Formisano-Kennel paper to bring out the field-aligned current aspect of the finite-wavelength (FW) hydromagnetic waves. The study is important for understanding the time-dependent auroral current sheets with thickness down to the ion inertial length and the ion gyroradius scale.

Emphasizing in so far as possible the relation of the two-fluid equations to the more familiar hydromagnetic equations, we combine the two-fluid equations into the one-fluid equations as shown in Appendix A.

$$\frac{\partial \rho}{\partial t} + \rho_0 \nabla \cdot \mathbf{V} = 0 \quad (2.8)$$

$$\rho_0 \frac{d\mathbf{V}}{dt} = -\nabla p + \frac{1}{c} \mathbf{J} \times \mathbf{B}_0 \quad (2.9)$$

$$\frac{\partial p}{\partial t} + \rho_0 C_s^2 \nabla \cdot \mathbf{V} = 0 \quad (2.10)$$

$$\mathbf{E} + \frac{1}{c} \mathbf{V} \times \mathbf{B}_0 = \frac{M_i}{e} \frac{d\mathbf{V}}{dt} + \frac{1}{ne} \nabla p_i \quad (2.11)$$

With a quasineutrality approximation and neglecting the electron mass m_e , the above one-fluid equations are equivalent to the two-fluid equations, which are rigorous consequences of the Vlasov equation except the particle-wave interaction [Vasyliunas, 1975]. Equation (2.11) is

known as the generalized Ohm's law, which is nothing more than the ion equation of motion since the assumption of negligible electron mass ensures the equivalence of the total fluid flow \mathbf{V} and the ion flow. If the right-hand side of the generalized Ohm's law (2.11) were zero, the Ohm's law would be that of hydromagnetics. Since hydromagnetics contains no basic scale-length, hydromagnetic waves must be nondispersive. The terms on the right-hand side of (2.11) create dispersive wave propagation at the appropriate wavelengths. The second to the last term in the right-side of Equation (2.11) is due to a finite ion inertia and its associated non-MHD effect is referred to as the finite-ion-inertial-length (FIL) effect, while the last term is due to a finite ion temperature (FIT) which is associated with the finite-ion-gyroradius effect. These non-MHD effects are expected to be important when the wavelength is of order of the ion inertial length or ion gyroradius.

The general dispersion relation valid for all frequencies and all wavelengths in a warm two-fluid plasma is given in Appendix A. For low-frequency waves ($\omega \gtrsim \Omega_i$), the quasi-neutrality approximation is adequate so that $\nabla \cdot \mathbf{J} \simeq 0$. Since the electron inertial length is much smaller than the ion inertial length, the electron inertia can also be neglected compared with the finite-ion-inertial-length effect. Therefore, the one-fluid equations (2.8)-(2.11), which result from the two-fluid equations by neglecting the electron inertia and assuming the quasineutrality, are adequate to describe the finite-wavelength hydromagnetic wave with a normalized wavevector $kL_i \gtrsim 1$ (L_i : ion inertial length). Upon linearizing (2.8)-(2.11) about an infinite homogeneous equilibrium with a uniform magnetic field and assuming harmonic perturbations of the form $\sim \exp[i(\mathbf{k} \cdot \mathbf{r} - \omega t)]$, one arrives at a dispersion relation for the three wave modes retained by the above approximations identical to that found by Stringer [1963] and Formisano and

Kennel [1969]

$$\begin{aligned} & (1 - k^2 V_A^2 \cos^2 \theta / \omega^2) [(1 - k^2 C_S^2 / \omega^2) - (k^2 V_A^2 / \omega^2) (1 - k^2 C_S^2 \cos^2 \theta / \omega^2)] \\ & = \left[(k^2 V_A^2 / \omega^2) (k^2 V_A^2 / \Omega_i^2) - (k^2 V_A^2 / \omega^2)^2 (k^2 C_S^2 / \Omega_i^2) \right] \cos^2 \theta \end{aligned} \quad (2.12)$$

where the ion gyrofrequency $\Omega_i = eB_0/(m_i c)$, and θ is the propagation angle between \mathbf{k} and B_0 . The sound speed C_S and the Alfvén speed V_A are the same as defined in the previous section. The ion inertial length $L_i = V_A/\Omega_i = c\sqrt{M_i/(4\pi n_o e^2)}$, while the ion gyroradius $R_i = L_i\sqrt{\beta} = C_s/\Omega_i$. The first term on the right side of (2.12) represents the finite-ion-inertial-length effect, and the second term on the right side represents the finite-ion-gyroradius effect. In the MHD limit (kL_i and $kR_i \rightarrow 0$), the terms on the right side of (2.12) may be neglected and the above dispersion relation is reduced to one for the ideal MHD waves as discussed in previous section.

The wave magnetic and electric fields and the pressure, density, and velocity perturbations can all be calculated from the linearized equations of motion together with the dispersion relation. In this study, I display but a few of these results. One interesting parameter is the ratio of wave field-aligned current to wave electric field. The field-aligned current density can be written as

$$J_{\parallel} = \mathbf{J} \cdot \frac{\mathbf{B}_0 + \mathbf{b}}{\sqrt{B_0^2 + b^2}} \quad (2.13)$$

where \mathbf{b} is the perturbation field. For linear waves $J_{\parallel} \simeq \mathbf{J} \cdot \mathbf{B}_0$ to the lowest order. This ratio can be expressed in the form below:

$$J_{\parallel}/J_N = \left(\frac{kV_A}{\Omega_i} \right) \left(\frac{kV_A}{\omega} \right) \frac{\sin \theta \sin \phi}{\sqrt{1 + R^2 \sin^2 \phi}} \quad (2.14)$$

where the current density is normalized by $J_N = \sigma_N E$ with $\sigma_N = \Omega_i c^2 / (4\pi V_A^2)$ and E is the magnitude of the wave field. The dimensionless ratio R and the angle ϕ are defined by

$$R = \frac{\Omega_i}{\omega} \left(\frac{\omega^2}{k^2 V_A^2} - \cos^2 \theta \right) \frac{1}{\cos \theta} \quad (2.15)$$

$$\cot \phi = \tan \theta \left[1 - \frac{\gamma_e T_e}{\gamma_e T_e + \gamma_i T_i} \frac{1 - k^2 V_A^2 \cos^2 \theta / \omega^2}{1 - \omega^2 / (k^2 C_s^2)} \right] \quad (2.16)$$

The angle ϕ is between \mathbf{k} and \mathbf{E}_p , the component of \mathbf{E} in the \mathbf{k} - \mathbf{B}_0 plane as defined in Appendix A.

Another interesting parameter is the compressibility of a wave mode. The compressibility can be measured by $\nabla \cdot \mathbf{V}$ and written as

$$\frac{\nabla \cdot \mathbf{V}}{AE} = -\frac{k V_A}{\omega} \frac{1 - k^2 V_A^2 \cos^2 \theta / \omega^2}{1 - k^2 C_s^2 / \omega^2} \frac{\sin \phi \tan \theta}{\sqrt{1 + R^2 \sin^2 \phi}} \quad (2.17)$$

where the normalization constant $A = c\Omega_i / (4B_0 V_A)$. The normalization by E is chosen to measure the compressibility in terms of the electric field.

Figure (2.1) shows the Friedrichs diagrams (for the phase velocity) to illustrate the dispersive nature (k dependence) and the β ($= C_s^2 / V_A^2$) dependence of the finite wavelength hydromagnetic waves. This display of wave dispersion has been used previously by Formisano and Kennel [1969] in the ω - β parameter space. Each of the Friedrichs diagrams illustrates the dependence of the phase velocity upon the propagation angle θ in a polar plot whose angle is that of wave propagation relative to the magnetic field \mathbf{B}_0 and whose radius vector is the magnitude of the phase velocity for given kL_i and β . For visual convenience, the scale of the polar diagrams has been adjusted; the dashed circles, which have a radius equal of the Alfvén speed V_A , provide a convenient reference. The horizontal axis is parallel to the external magnetic field \mathbf{B}_0 . The three solid curves in each panel show the phase velocities of the three wave modes. The solid curve with the largest radius is for the fast waves. The solid curve with intermediate radius is for the Alfvén waves. The solid curve with the smallest radius is for the slow waves.

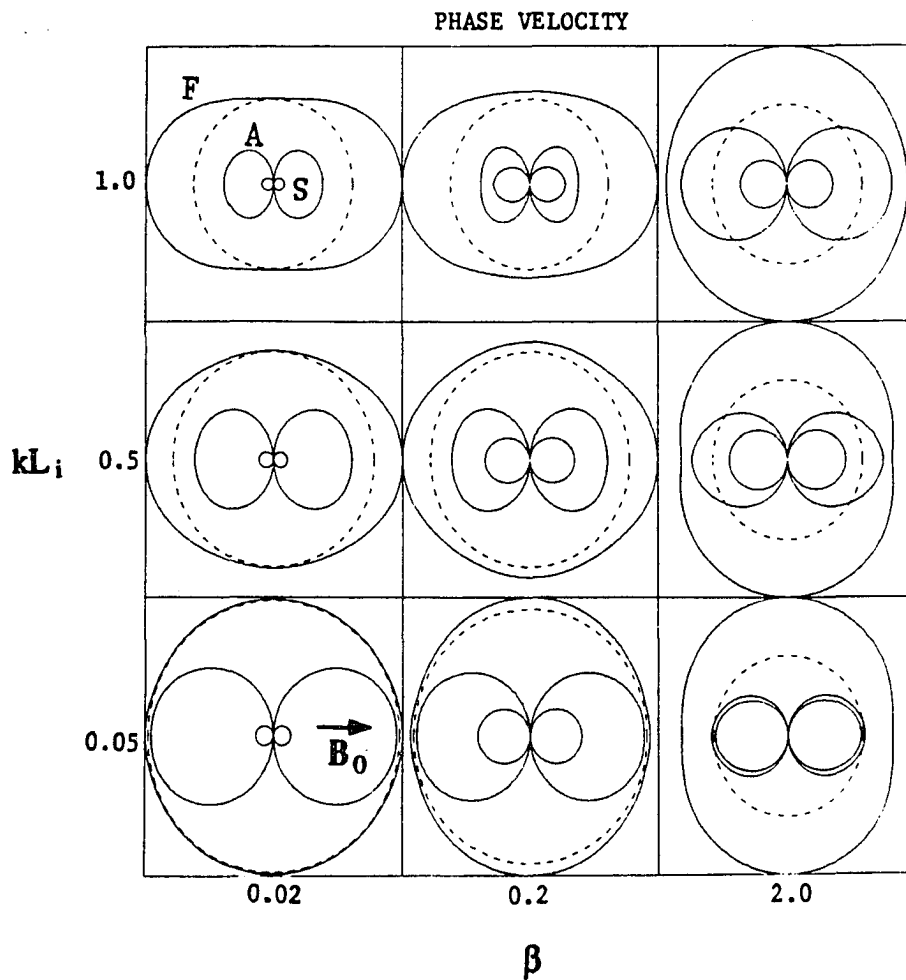


Figure 2.1 Polar plots of phase velocities in the k - β parameter space. k is the wave number, β is the ratio of plasma to magnetic pressures and L_i is the ion inertial length. The directionality in the figure is for the wave vector relative to the magnetic field B_0 , which is along the horizontal axis. The three solid curves in each panel show the phase velocities of the three wave modes. The solid curve with the largest radius is for the fast waves. The solid curve with intermediate radius is for the Alfvén waves. The solid curve with the smallest radius is for the slow waves. The dashed circle, which has a radius equal of the Alfvén speed V_A , provide a convenient reference (from Cao and Kan, 1987).

The phase velocities in the MHD limit are shown in the bottom panels ($kL_i = 0.05 \ll 1$). The normalized ion-inertial length (kL_i) increases from the bottom panels to the top panels, while the normalized ion gyroradius ($kR_i = kL_i\sqrt{\beta}$) increases from the left panels to the right panels. When the wavelength is comparable to the ion inertial length, the ions no longer completely follow the oscillations of the field lines. The motion is as if the ions were attached to the field lines, not rigidly but by a flexible coupling. For the right-hand polarized fast mode, the ions, whose gyromotion is in the left-hand sense, perform oscillations at a reduced amplitude. Because any motion of the field lines leads to a smaller motion of the ions, the inertia loading of the ions is correspondingly reduced and the wave velocity increases. In contrast, the Alfvén mode in $\beta < 1$ plasmas is polarized in the left-hand sense and evolves from the MHD Alfvén wave into the ion-cyclotron wave. Motion of the field lines produces progressively larger amplitude ion motion that resonates at Ω_i . Therefore, as the wavelength decreases towards the ion inertial length, the increasing inertia loading of the field lines progressively reduces the velocity in such a way that ω tends asymptotically to Ω_i . In $\beta > 1$ plasmas, the Alfvén wave electric field is highly elliptically polarized and in the right-handed sense, so that the ion cyclotron resonance is not possible in the $\beta > 1$ regime and the phase velocity increases in the same way as that of fast waves. When the wavelength is comparable to the ion gyroradius, the pressure force becomes important so that it becomes possible for the Alfvén mode to evolve into an ion acoustic wave. The finite-ion-inertial-length (FIIL) effect has little or no impact on the phase velocity of the slow mode. However, the slow wave, which is almost a longitudinal wave in $\beta < 1$ plasmas becomes an electromagnetic wave in $\beta > 1$ plasmas and the wave speed changes from the sound speed to the Alfvén speed.

Figure (2.2) shows the polar plots of the normalized field-aligned currents defined in (2.14) for the three finite-wavelength (FW) hydromagnetic waves. The radius of each curve shows the magnitude of the normalized field-aligned current; the radius vector is in the direction of

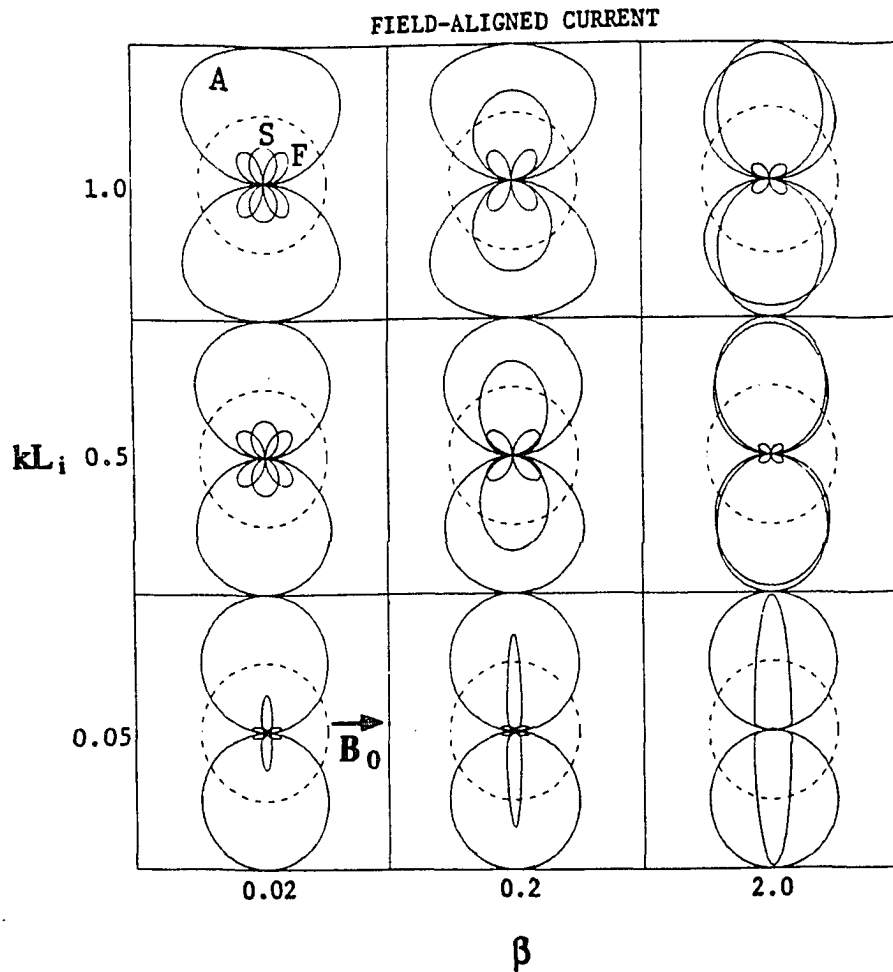


Figure 2.2 Polar plots of field-aligned currents of the finite-wavelength hydro-magnetic waves in the k - β parameter space (see Figure 2.1 caption). The radius of each curve represents the magnitude of field-aligned current and the radius vector is in the direction of the wavevector. The dashed circle is a reference circle of radius kL_i . Each solid curve is identified with one wave mode as explained in the text (from Cao and Kan, 1987).

the wavevector. The external magnetic field is parallel to the horizontal axis. The solid curve with the largest radius in each panel is for the FW Alfvén mode. The curve that goes to zero at $\theta = 0^\circ$ and 90° (parallel and perpendicular to B_0) is for the FW fast mode (where θ is the angle measured for the horizontal axis along B_0). The curve that peaks at $\theta = 90^\circ$ and goes to zero at $\theta = 0^\circ$ is for the FW slow mode. The dashed circle is a reference circle of radius kL_i that illustrates how the field-aligned current increases with decreasing wavelength $\lambda = 2\pi/k$ on the plots.

As indicated in equation (2.14) and Figure (2.2), the ratio of the field-aligned current to the electric field increases in proportion to the normalized wavelength kL_i . This result is consistent with observations [Sugiura *et al.*, 1983] that the thin auroral field-aligned current sheets are more intense than the large scale region I and region II field-aligned currents. It is seen from Figure (2.2) that the field-aligned current is predominantly associated with the Alfvén mode in $\beta \ll 1$ plasmas. When the plasma β increases, the slow mode wave, which is almost an electrostatic wave in the MHD limit, becomes increasingly electromagnetic and the field-aligned current in the slow mode also increases. In comparison, the fast mode still has insignificant amount of field-aligned currents. The field-aligned current in both the Alfvén and slow modes goes to zero at $\theta = 0^\circ$ and peaks at $\theta = 90^\circ$. It means the field-aligned current is primarily related to the highly oblique ($\theta \sim 90^\circ$) Alfvén and slow mode waves. In the magnetosphere and ionosphere coupling, the characteristic wavelength along the magnetic field lines is of order of the distance between the ionosphere and magnetopause. This distance is about 20 earth radii. The perpendicular wavelength is either determined in the ionosphere by the convection scale length ranging from 10's km to a few 1000 km, or measured in the magnetosphere with a few earth radii. Therefore, the short perpendicular wavelength limit $k_{\parallel} \ll k_{\perp}$, required in the magnetosphere and ionosphere coupling process, does support a highly oblique wave. Since the slow waves are heavily Landau damped especially for highly

oblique propagation [Barnes, 1966], the slow mode cannot propagate a long distance away from a source of disturbance, so that the slow mode is not expected to be a dominant mode in the energy transport process for the magnetosphere and ionosphere coupling. However, in some local regions of the plasma or field nonuniformity, the slow mode wave may be coupled to the dominant Alfvén mode to modify the local field-aligned current and the compressibility. This issue will be further addressed in chapters 3.

Figure (2.3) shows the group velocities of the three finite-wavelength (FW) hydromagnetic waves. In each region is the polar plot whose radius is the magnitude of group velocity and whose angle is the angle of group velocity relative to the magnetic field \mathbf{B}_0 . The dashed circle is a reference circle of radius V_A (Alfvén speed). The curve with largest radius is for the FW fast mode. The curve of the smallest radius is for the FW slow mode. The remaining curve is for the FW Alfvén mode. Notice that the group velocity in Figure (2.3) is significantly different with the phase velocity shown in Figure (2.1). The group velocities of FW Alfvén and slow modes are highly parallel to the external magnetic field even when the wave vector is highly oblique to the field lines. Thus, the wave energy of these two modes is well guided along field lines. In contrast, the group velocity of the FW fast mode is somewhat isotropic, so that the energy associated with the fast mode will spread out in all directions around a source of disturbance. The fast mode with a wavelength down to the ion inertial length cannot be very important in the energy transport process for the magnetosphere and ionosphere coupling, since the fast mode suffers a serious geometric attenuation with distance and the distance between the magnetosphere and the ionosphere is much larger than the characteristic convection scale perpendicular to the magnetic field. When the wavelength is much smaller than the ion inertial length $kL_i \gg 1$, the fast mode is known to become a whistler wave that is well guided along the field lines. However, the whistler with a wavelength much smaller than the ion inertial length is of no interest in this study and its group velocity is not shown in Figure (2.3).

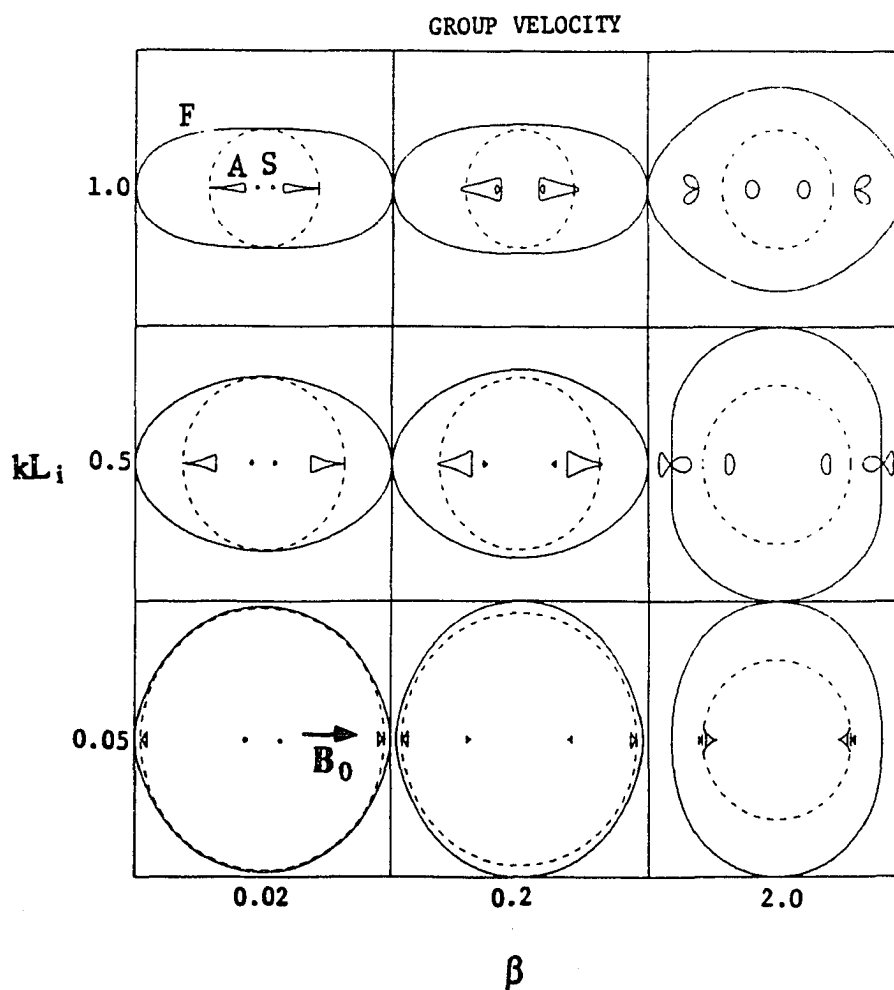


Figure 2.3 Polar plots of the group velocity in the k - β parameter space [see Figure (2.1) caption]. The directionality in this figure is for the group velocity relative to the magnetic field \mathbf{B}_0 , while the directionality in the other three figures is for the wave vector. The identification of each curve with a wave mode is given in the text (from Cao and Kan, 1987).

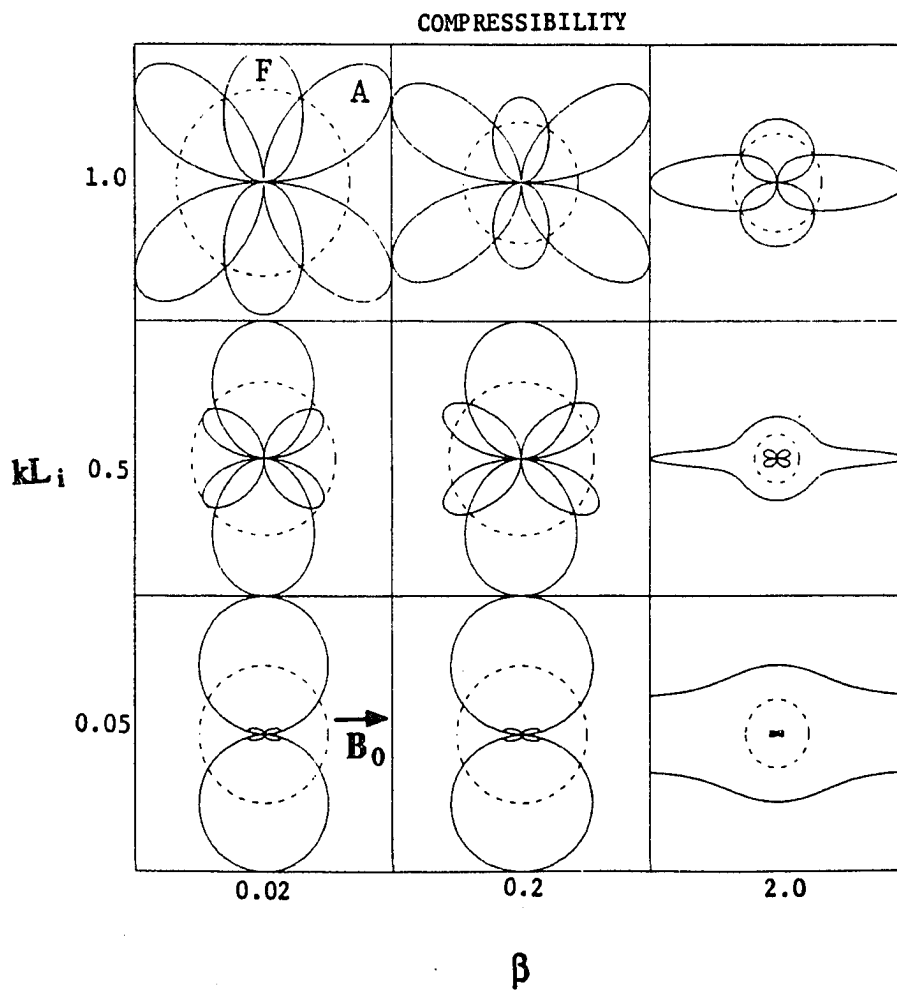


Figure 2.4 Polar plots of compressibility of the finite-wavelength fast and Alfvén modes. The dashed circle is a reference circle of radius kL_i (from Cao and Kan, 1987).

Figure (2.4) shows the compressibility of the finite-wavelength (FW) fast and Alfvén modes. The compressibility of slow mode (not shown) is similar to the sound wave, which is much more compressive than the fast and Alfvén waves. The radius vector is in the direction of the wave vector. The radius shows the magnitude of $\nabla \cdot \mathbf{V}$ normalized by the wave electric field and the dashed circle is a reference circle of radius kL_i . When the wavelength decreases, Alfvén waves become increasingly more compressive. The compressibility of Alfvén waves is highly directional going to zero at $\theta = 0^\circ$ and 90° , and peaking in between, except for the plot on the top-right corner where the normalized ion gyroradius $kR_i = kL_i\sqrt{\beta} > 1$ and the compressibility peaks at $\theta = 0^\circ$.

2.3 Discussion and Summary

I have presented the results of the three finite-wavelength hydromagnetic modes ($kL_i \lesssim 1$) based on the two-fluid plasma equations. The results show that the time-dependent field-aligned current can be propagated predominantly by the highly oblique Alfvén waves. The group velocities of Alfvén waves are well guided along field lines even in the finite-wavelength regime ($kL_i \lesssim 1$). These properties indicate that the Alfvén mode should play a dominant role in initiating field-aligned currents and in transporting energy on all spatial scales down to the ion inertial length and the ion gyroradius scale. Both the finite-ion-inertial and finite-ion-temperature effects are responsible for the compressibility in the FW Alfvén mode, and the compressibility increases steadily with the wavelength decrease. The fast mode is strongly compressive in an oblique propagation, but related only to a small field-aligned current. Since it is not guided along field lines, the fast mode cannot be important in the magnetosphere-ionosphere coupling. The slow mode is compressive, well guided along field lines and related to a significant amount of field-aligned currents in the finite-wavelength regime. However, the

slow mode is heavily Landau damped [Barnes, 1966] and therefore cannot be as important as the Alfvén mode in transporting energy from the magnetosphere to the ionosphere.

In conclusion, the results in this study confirm that the Alfvén mode is the dominant mode in the magnetosphere and ionosphere coupling process for initiating and transmitting time-dependent field-aligned currents down to the auroral arc scale length in the magnetosphere-ionosphere coupling. The time-dependent field-aligned currents and the convection electric fields evolve self-consistently through the bouncing of Alfvén waves and approach to a steady state as the Alfvén waves damp out [Kan and Sun, 1985]. The compressible Alfvén wave in the finite-wavelength regime not only is responsible for initiating the field-aligned currents but may also modify the plasma pressure gradient with a scale length down to the ion inertial length and the ion gyroradius. The region II steady state field-aligned current is proposed to be generated by the pressure gradient in the inner edge of the plasma sheet [e.g., Vasyliunas, 1970; Southwood, 1977; Harel *et al.*, 1981a, b; Wolf *et al.*, 1982]. The large pressure gradient in the inner edge of the plasma sheet results from the formation of the ring current, which acts as a shield tending to isolate the middle and low-latitude ionosphere and the plasmasphere from the externally imposed dawn-to-dusk electric field, and to confine the magnetospheric convection to high latitudes [e.g., Karlson, 1962, 1963; Schield *et al.*, 1969; Vasyliunas, 1972; Senior and Blanc, 1984]. The basic principle of the shielding comes from the polarization charges accumulated at the edge of the ring current, creating a secondary electric field that approximately cancels the effect of the imposed electric field and preventing the plasma from convection into the low-latitude regions. The shielding layer is very thin. As shown by Karlson [1963], the thickness of the shielding layer is of order of $1 R_e$ measured in the equatorial plane, which corresponds to a scale length of a few 10 km in the ionosphere. Therefore, the finite-wavelength Alfvén wave may play a key role in discharging the polarization current and in smoothing the pressure gradient piled up in the inner edge of the plasma sheet. However, on

the larger convection scale, the finite-ion-inertial-length (FIIL) and the finite-ion-temperature (FIT) effects are unimportant as far as the compressibility of Alfvén mode is concerned. To relate the time-dependent pressure gradient, one must consider the plasma nonuniformity on the convection scale as a possible cause of compressibility in the Alfvén mode. Due to the nonuniformity of the plasma and the magnetic field, the Alfvén wave may be coupled to the fast and slow modes, resulting the modification of the field-aligned current and pressure distributions in some local regions. This issue will be further discussed in chapter 3.

CHAPTER 3

Reflection of Alfvén Waves From the Magnetosphere

The interaction of Alfvén waves with the magnetospheric boundaries is an important issue particularly in connection with the magnetosphere and ionosphere (M-I) coupling processes [e.g., Kan and Sun, 1985; Scholer, 1970; Mallinckrodt and Carlson, 1978; Lysak and Dum, 1983]. The Alfvén wave has been identified in chapter 2 as a dominant mode in the M-I coupling processes. The enhanced dayside reconnection leads to an enhanced magnetospheric convection, which must propagate toward the ionosphere by Alfvén waves. These Alfvén waves subsequently reflect off the ionosphere and then propagate toward the magnetospheric boundaries. Thus, the dynamic M-I coupling may well be modeled in terms of the Alfvén wave bouncing between the ionosphere and magnetospheric boundaries.

In magnetosphere-ionosphere (M-I) coupling, it proves convenient to formulate the coupling problem in terms of electric fields and field-aligned currents, i.e., the M-I coupling occurs through the flow of field-aligned currents and mapping of electric fields. Reflection of Alfvén waves from the ionosphere has been well studied [e.g., Kan and Sun, 1985]. The ionosphere can be approximated as a height-integrated conducting plate. Reflection of Alfvén waves from the ionosphere is determined by matching the field-aligned current of the incident and reflected Alfvén waves to the divergence of the ionospheric current, which is directly related with the electric field by a simple Ohm's law. In comparison, the magnetospheric plasmas are highly collisionless and there exist no explicit relationships between the electric field and current. A difficulty thus arises in determining the Alfvén wave reflection at the magnetospheric

boundaries. The physics governing magnetospheric reflection of Alfvén wave is further complicated by a wide range of the background inhomogeneity, caused by the different physical mechanisms.

The study in this chapter is a theoretical investigation of the Alfvén wave reflection from the magnetospheric boundaries. The chapter is organized as follow. Section (3.1) discusses reflection of Alfvén waves at an open magnetopause. Section (3.2) is concerned with the wave reflection from the central plasma sheet due to field curvature near the equatorial plane. Section (3.3) contains a qualitative description of the wave reflection at the low-latitude boundary.

3.1 Reflection of Alfvén Waves at an Open Magnetopause

The open magnetopause, whose structure is different from the standard rotational discontinuity, is assumed to be a parameterized discontinuity with a nonzero normal field component. Due to the bending of magnetic field lines at the open magnetopause, the incompressible Alfvén wave incident on the open magnetopause not only generates the reflected and transmitted Alfvén waves, but also brings about the compressible fast and slow waves. These emanating waves can be analyzed using linearized MHD conservation relations across the magnetopause, together with Snell's law. The results show that the electric fields of emanating Alfvén waves depend mainly on the number density and the magnetic field jumps across the magnetopause. Under conditions representing the open magnetopause, it turns out that the open magnetopause behaves like a near perfect reflector. The corresponding reflection amplitude ratio for the wave electric fields can be approximated by $R_E = E^r/E^i \approx -1$ as has been deduced by Kan and Sun [1985] based on physical arguments.

In the first section I will briefly review some existing work on the interaction of hydro-magnetic waves with the magnetopause. The second section will introduce the basic equations,

which are used to describe the open magnetopause and to determine the amplitude of emanating waves. In the third section, I will present the numerical results and discuss the dependence of reflection and transmission amplitude ratios on different parameters. The final section will summarize the main results.

3.1.1 Introduction

The magnetopause marks the transition between the solar-wind magnetic field and the geomagnetic field. The earth's magnetopause has been under constant study both theoretically and observationally. It is generally believed that solar wind entry and energy transfer into the magnetosphere from the magnetosheath are directly controlled by the magnetic field configuration at the magnetopause, especially by the normal component of magnetic field B_n . The magnetopause is considered closed if the normal field component is zero, i.e., $B_n = 0$. Reflection and transmission of MHD waves incident on the closed magnetopause have been studied by several authors [McKenzie, 1970; Verzariu, 1973; Wolfe and Kaufmann, 1975]. They showed that the closed magnetopause, represented by a plane hydromagnetic tangential discontinuity, can reflect the incident wave almost completely, and therefore is a near perfect reflector.

The magnetopause is considered open if the normal field component is nonzero, i.e., $B_n \neq 0$. The dayside magnetopause has been observed to be open on several occasions [Russell and Elphic, 1978; Sonnerup and Ledley, 1979; Sonnerup *et al.*, 1981; Berchem and Russell, 1982a]. The magnetic field changes its magnitude as it rotates across the dayside open magnetopause. Indeed, the structure of the open magnetopause is often different from that of the standard MHD rotational discontinuity solution [Landau and Lifshitz, 1960]. Several ideas have been proposed to explain the discrepancy between the observed magnetopause structures

and the standard rotational discontinuity. For example, Coroniti and Kennel [1979] suggested that the MHD slow mode wave can change the magnetosheath plasma conditions to the mantle and tail lobe plasma conditions. Swift and Lee [1982, 1983], Siscoe and Sanchez [1987] and Sanchez *et al.* [1990a, b] argued that the rotational discontinuity and the slow mode wave act together to form the dynamo action. Recently, Lyu and Kan [1989] identified the S-shaped magnetic hodograms observed at the magnetopause [Berchem and Russell, 1982a] with the Alfvén shock hodograms obtained from a two-fluid simulation model.

Reflection and transmission of MHD waves at the standard rotational discontinuity have been studied by Lee [1982] and Kwok and Lee [1984]. They showed that Alfvén waves in the solar wind can easily transmit across the open magnetopause if the magnetopause is assumed to be a rotational discontinuity. However, reflection of MHD waves from the observed type of open magnetopause structures has not yet been studied to my knowledge.

The purpose of the present study is to examine reflection and transmission of Alfvén waves at the open magnetopause. On the basis of a simple physical consideration, Kan and Sun [1985] argued that an Alfvén wave incident on the open magnetopause from the magnetospheric side should be reflected as if the solar wind is an infinite energy source capable of maintaining a constant convection electric field on open field lines. They concluded that the reflection amplitude ratio for the wave electric field should be $R_E = E^r/E^i \approx -1$ so that the open magnetopause can be treated as a constant voltage source. It will be shown quantitatively in this study that the open magnetopause behaves increasingly more like a constant voltage source as the density jump or the magnetic field jump increases across the magnetopause.

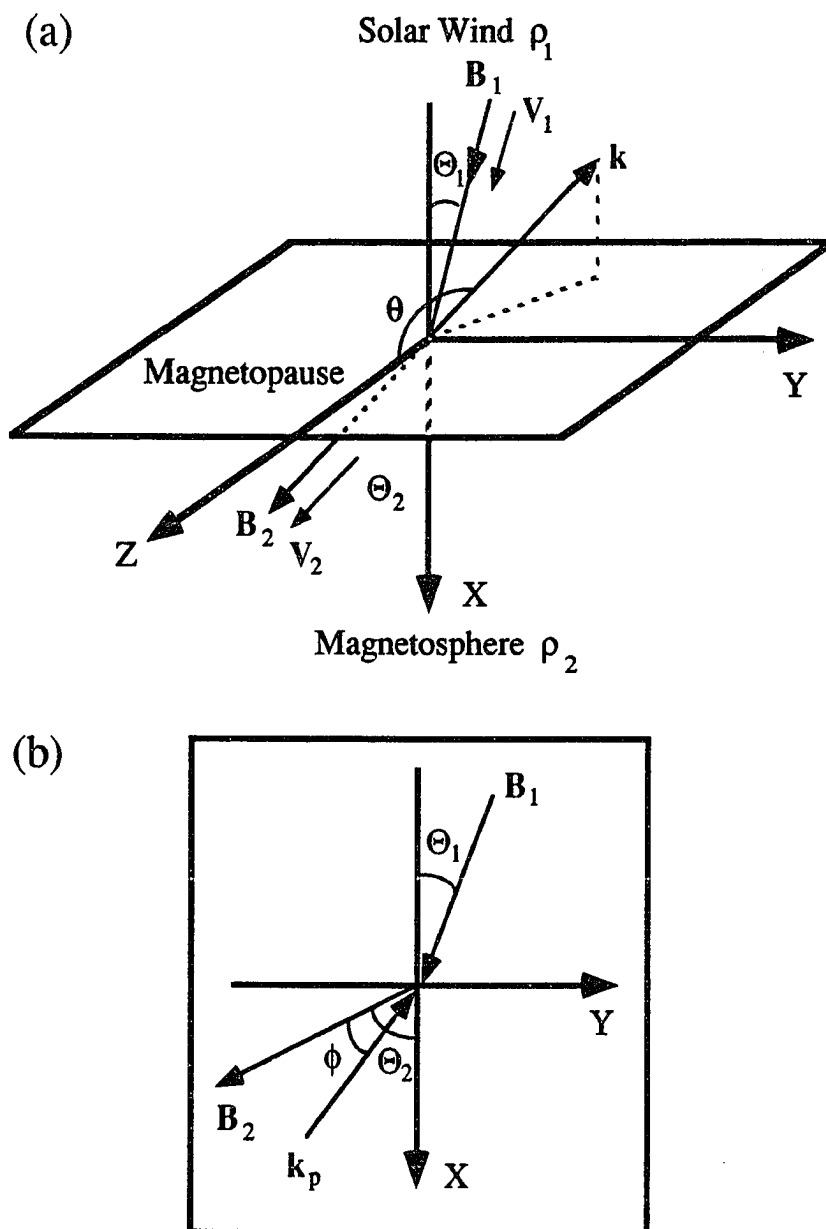


Figure 3.1 Configuration of the magnetopause and coordinate system. The magnetopause is represented by the $y-z$ plane at the interface of region 1 (solar-wind) and region 2 (magnetosphere). The ambient magnetic field \mathbf{B} and the fluid velocity \mathbf{V} are parallel to each other in the de Hoffmann-Teller frame and are assumed to lie on the $x-y$ plane. The field normal angles Θ_1 and Θ_2 are respectively the angles of the magnetic fields B_1 and B_2 to the normal y direction of the magnetopause. Wavevector of the incident Alfvén wave from the magnetosphere is denoted by the vector \mathbf{k} with a wave normal angle θ measured from the z -axis and an azimuthal angle ϕ between the magnetic field B_2 and the k_p , which is a projection of \mathbf{k} on the $x-y$ plane. (A) A three-dimensional view. (B) Projection on $x-y$ plane.

3.1.2 A Parameterized Open Magnetopause

Figure (3.1) shows the configuration of the open magnetopause along the high-latitude magnetotail. The solar-wind (side 1) and magnetosphere (side 2) are separated by the open magnetopause on the y - z plane, upon which an incident Alfvén wave from the magnetosphere is considered. The solar-wind is assumed to be a uniform magnetized warm plasma under the MHD approximation, while the magnetosphere is assumed to be a cold plasma since the temperature in the magnetotail lobe is low compared with that in the magnetosheath [Rosenbauer *et al.*, 1975; Sckopke and Paschmann, 1978].

Jump Conditions Across the Open Magnetopause

Along the high-latitude magnetotail, the solar-wind can flow across the open magnetopause to form the plasma mantle in which the plasma density is reduced to about 5 percent of its solar wind value. The open field lines can also rotate across the open magnetopause into the tail lobe [Rosenbauer *et al.*, 1975; Sckopke and Paschmann, 1978; Sibeck and Siscoe, 1985]. The open magnetopause, characterized by this abrupt change in the plasma density and magnetic field along the high-latitude magnetotail, often differs from the characteristics of the standard MHD rotational discontinuity. The structure of the open magnetopause along the magnetotail can be expected to be modified by the dynamo process action that slows down the magnetosheath plasma flow due to the line-tying effect of the resistive ionosphere. Several attempts have been made to understand this dynamo process on the open magnetopause [e.g., Swift and Lee, 1982, 1983]. However, a well-developed theory or an observational model of the dynamo process at the magnetopause is not yet available. To make the algebra more tractable, while at the same time retaining the essential physics, we will assume that the open magnetopause is a discontinuity satisfying the jump conditions required by the conservation laws of mass and momentum fluxes and the continuity of the tangential electric field.

For the sharp boundary approximation treated in this study to be valid, the wavelength considered in this study must be much greater than the thickness of the magnetopause. The thickness of the open magnetopause, including the plasma mantle, ranges from 0.2 to 4 earth radii in a near-earth distance and expands to the dimension of the magnetosphere in the distant magnetotail [Rosenbauer *et al.*, 1975; Sckopke and Paschmann, 1978; Hardy *et al.*, 1975; Sibeck and Siscoe, 1985]. The wavelength along the magnetic field lines is of the order of the distance between the magnetopause and the ionosphere that is about 20 earth radii. This wavelength for the bouncing Alfvén waves can be expected to be much greater than the thickness of the near-earth magnetopause including the plasma mantle. However, since the mantle thickness increases rapidly with tailward distance, the conditions for the sharp boundary assumption are likely violated at a tailward distance greater than lunar orbit (60 earth radii). At that distance, the structure of the open magnetopause has to be taken into account. The open magnetopause may be treated as an inhomogeneous continuous medium with monotonically increasing density and decreasing magnetic field from the magnetosphere to the solar-wind.

The imposed jump conditions which relate quantities on the two sides of an open magnetopause can be written as follows [e.g., Landau and Lifshitz, 1960]

Conservation of normal mass flux

$$[\rho U_n] = 0 \quad (3.1)$$

Conservation of tangential electric field

$$[U_n \mathbf{B}_t - \mathbf{U}_t B_n] = 0 \quad (3.2)$$

Conservation of tangential momentum

$$[\rho U_n \mathbf{U}_t - B_n \mathbf{B}_t / 4\pi] = 0 \quad (3.3)$$

Conservation of normal momentum

$$[p + \rho U_n^2 + (B_t^2 - B_n^2) / 8\pi] = 0 \quad (3.4)$$

where ρ is the fluid density, \mathbf{B} the ambient magnetic field, \mathbf{U} the fluid velocity; the subscripts n and t denote respectively the normal and tangential components of a perturbed vector at the boundary, and $[A] = (A)_1 - (A)_2$.

Note that we leave out the jump condition on the energy flux across the magnetopause so that the open magnetopause can be modeled with more independent parameters than allowed by the MHD rotational discontinuity. The discontinuity including the plasma mantle, described by the model equations (3.1)-(3.4), is referred to as a parameterized open magnetopause. Although the parameterized discontinuity is consistent with observations that the plasma expands and cools as it passes from the low field region of the solar-wind into the higher field region of the magnetotail lobe, it says nothing about the energy transfer process at the open magnetopause. In the one-dimension model, the energy flux is not necessarily constant in passing from the solar-wind to the magnetosphere. However, the model does not violate the energy conservation law because the excess energy flux can flow antisunward within the expanding

plasma mantle. Corresponding to the requirement of the energy conservation, there would be a certain relationship among the magnetopause parameters. Examination of this relationship is beyond the study in this section and will have to wait the development of a more realistic two-dimension model.

In this study, we choose the de Hoffmann-Teller frame in which the electric field vanishes and the fluid moves parallel to the magnetic field. By writing $\mathbf{U} = \mathbf{U}_0 + \delta\mathbf{U}$, $\rho = \rho_0 + \delta\rho$, ..., where the subscript 0 denotes the unperturbed zero-order quantities and $\delta\mathbf{U}$, $\delta\rho$... denote the first order perturbations, the first order equations of (3.1)-(3.4) can be written as (the subscript 0 for the zero-order quantities are dropped hereafter):

$$[\rho\delta U_n + U_n\delta\rho] = 0 \quad (3.5)$$

$$[U_n\delta\mathbf{B}_t + \mathbf{B}_t\delta U_n - B_n\delta\mathbf{U}_t - \mathbf{U}_t\delta B_n] = 0 \quad (3.6)$$

$$[\rho U_n\delta\mathbf{U}_t + \mathbf{U}_t(\rho\delta U_n + U_n\delta\rho) - (B_n\delta\mathbf{B}_t + \mathbf{B}_t\delta B_n)/4\pi] = 0 \quad (3.7)$$

$$[\delta p + 2\rho U_n\delta U_n + U_n^2\delta\rho + (\mathbf{B}_t \cdot \delta\mathbf{B}_t - B_n\delta B_n)/4\pi] = 0 \quad (3.8)$$

The analysis can be simplified by choosing a coordinate system in which the x-y plane contains the unperturbed velocity and magnetic field vectors as shown in Fig. (3.1). We assume perturbations of the form $\exp[i(\mathbf{k} \cdot \mathbf{r} - \omega t)]$ and take the magnetopause distortion to be of the same form $x = \eta \exp[i(k_y y + k_z z - \omega t)]$. Following the derivation given by McKenzie and Westphal [1970], we obtain the system of equations in matrix form from the first order jump

equations (3.5)-(3.8),

$$\vec{T}_2 \cdot \mathbf{Y}_2 + \mathbf{R} \delta U_s = \vec{T}_1 \cdot \mathbf{Y}_1 \quad (3.9)$$

$$\vec{T} = \begin{pmatrix} U_x & \rho & 0 & 0 & 0 & 0 & 0 \\ 0 & \frac{B_y}{B_x} & -1 & 0 & -\frac{U_y}{V_{Ax}} & \frac{U_x}{V_{Ax}} & 0 \\ 0 & 0 & 0 & -1 & 0 & 0 & \frac{U_x}{V_{Ax}} \\ \frac{U_y}{\rho} & \frac{U_y}{U_x} & 1 & 0 & -\frac{V_{Ay}}{U_x} & -\frac{V_{Ax}}{U_x} & 0 \\ 0 & 0 & 0 & 1 & 0 & 0 & -\frac{V_{Ax}}{U_x} \\ \frac{\gamma p / \rho + U_x^2}{\rho U_x} & 2 & 0 & 0 & -\frac{V_{Ax}}{U_x} & \frac{V_{Ay}}{U_x} & 0 \end{pmatrix} \quad (3.10)$$

$$\mathbf{R} = \begin{pmatrix} [\rho(1 - U_y k_y / \omega)] \\ [B_y / B_x] \\ 0 \\ [U_y / U_x] + [U_x - U_y^2 / U_x + V_{Ay}^2 / U_x] k_y / \omega \\ [U_x] k_z / \omega \\ 0 \end{pmatrix} \quad \mathbf{Y} = \begin{pmatrix} \delta \rho \\ \delta U_x \\ \delta U_y \\ \delta U_z \\ \delta V_{Ax} \\ \delta V_{Ay} \\ \delta V_{Az} \end{pmatrix} \quad (3.11)$$

where $\delta U_s = \partial x / \partial t$ is the perturbation velocity of the magnetopause and $\delta V_A = \delta \mathbf{B} / \sqrt{4\pi\rho}$ is the perturbed magnetic field; $\mathbf{V}_a = (V_{Ax}, V_{Ay}) = \mathbf{B} / \sqrt{4\pi\rho}$. Subscripts x, y and z denote x-, y- and z-components in the de Hoffmann-Teller frame; Subscripts 1 and 2 denote side 1 and side 2. The elements in the matrix \vec{T} and the vector \mathbf{R} are given by the zero-order quantities, and the vector \mathbf{Y} contains the perturbations in the density, velocity and magnetic field.

The zero-order equations of (3.1)-(3.4) relate the unperturbed quantities in terms of three independent parameters:

$$\begin{cases} \Theta_1, & \text{the normal angle of the solar-wind field } \mathbf{B}_1 \text{ to x-axis;} \\ \beta_1 = 8\pi p_1 / B_1^2, & \text{the solar-wind thermal pressure to magnetic pressure ratio;} \\ \rho_r = \rho_2 / \rho_1, & \text{the magnetosphere-solar wind density ratio.} \end{cases}$$

With given parameters Θ_1 , β_1 and $\rho_r = \rho_2 / \rho_1$, Equations (3.1) to (3.4) may be combined to give the normal angle Θ_2 , which is the angle of the ambient magnetic field \mathbf{B}_2 in the

magnetosphere to the normal of the magnetopause.

$$(\tan \Theta_2 - \rho_r \tan \Theta_1) [\tan^2 \Theta_2 - (1 + \beta_1) \tan^2 \Theta_1 - \beta_1] + 2(1 - \rho_r)(\tan \Theta_2 - \tan \Theta_1) = 0 \quad (3.12)$$

Since the magnetic field in the solar-wind must rotate across the open magnetopause towards the earth, we require $\Theta_2 \geq \Theta_1$ with which there is only one solution of Equation (3.12). When the density ratio $\rho_r = \rho_2 / \rho_1 = 1$, we obtain from the jump conditions (3.1)-(3.4) the standard MHD rotational discontinuity. Since the normal flow velocity component is equal and opposite to the Alfvén speed based on the normal field component at the rotational discontinuity, an incident Alfvén wave can not propagate toward the magnetopause from the magnetospheric side. Therefore, the governing equations for the reflection of Alfvén waves at the magnetopause become singular. In the following calculations, the magnetosphere-solar wind density ratio ρ_r will be less than 1 and the normal plasma flow speed will be assumed to be less than the Alfvén normal speed, so that an Alfvén wave in the magnetosphere can propagate against the plasma flow and reach the magnetopause.

Amplitudes of Reflected and Transmitted Waves

In a uniform plasma there are only three wave modes: the Alfvén waves, the fast and slow magnetosonic waves. If the plasma is cold, the slow magnetosonic wave will disappear. When an Alfvén wave impinges on the open magnetopause, the outgoing perturbation is composed of five emanating waves, Alfvén and fast waves in the cold tail lobe plasma; Alfvén, fast and slow waves in the warm magnetosheath plasma.

In equations (3.9)-(3.11), the vectors Y_2 and Y_1 , representing perturbed quantities due to wave motions in the magnetosphere and in the magnetosheath, can be treated as sums of hydromagnetic eigenwave perturbations. The perturbed quantities associated with each

eigenwave are interrelated; when one is known, the rest can be determined. When Y_2 and Y_1 are expressed in terms of eigenwave perturbations of the electric field, they can be written as

$$Y_2 = Y_{2A}^d + Y_{2F}^d + Y_{2A}^i = F_{2A}^d \delta E_{2A}^d + F_{2F}^d \delta E_{2F}^d + F_{2A}^i \delta E_{2A}^i \quad (3.13)$$

$$Y_1 = Y_{1A}^d + Y_{1F}^d + Y_{1S}^d = F_{1A}^d \delta E_{1A}^d + F_{1F}^d \delta E_{1F}^d + F_{1S}^d \delta E_{1S}^d \quad (3.14)$$

where δE is defined as the magnitude of a certain wave electric field. The vector F , which relates the perturbations Y in density, velocity and magnetic field with δE , is an expression describing eigenwave properties. A quantity associated with an incident wave carries a superscript i and that with an outward propagating wave d . The subscripts A, F and S denote the Alfvén, fast and slow waves, respectively. The subscripts 1 and 2 again stand for the solar wind and the magnetosphere. For example, Y_{2A}^d , which expresses the density, velocity and magnetic field perturbations associated with the emanating Alfvén wave in the magnetosphere, can be determined by the magnitude of the wave electric field.

$$Y_{2A}^d = F_{2A}^d \delta E_{2A}^d \quad \text{where:} \quad F_{2A}^d = \frac{1}{B_2 |\mathbf{e}_B \times \mathbf{e}_k|} \begin{pmatrix} 0 \\ \mathbf{e}_B \times \mathbf{e}_k \\ -\mathbf{e}_B \times \mathbf{e}_k \end{pmatrix} \quad (3.15)$$

where \mathbf{e}_B and \mathbf{e}_k are unit vectors for the ambient magnetic field and the wavevector, respectively. The expressions of the vector F for other wave modes have been given by McKenzie and Westphal [1970].

Substituting (3.13) and (3.14) into (3.9), we obtain a system of six linear inhomogeneous equations for the amplitudes of the emanating wave electric field and the perturbed layer velocity δU_s in terms of the amplitudes of the incident waves.

$$\vec{T}_2 \cdot \mathbf{F}_{2A}^i \delta E_{2A}^i = \begin{pmatrix} \delta E_{2A}^d \\ \delta E_{2F}^d \\ \delta E_{1A}^d \\ \delta E_{1F}^d \\ \delta E_{1S}^d \\ \delta U_s \end{pmatrix} \cdot \begin{pmatrix} -\vec{T}_2 \cdot \mathbf{F}_{2A}^d, & -\vec{T}_2 \cdot \mathbf{F}_{2F}^d, & \vec{T}_1 \cdot \mathbf{F}_{1A}^d, & \vec{T}_1 \cdot \mathbf{F}_{1F}^d, & \vec{T}_1 \cdot \mathbf{F}_{1S}^d, & -R \end{pmatrix}. \quad (3.16)$$

Equation (3.16) is in a matrix form $\mathbf{C} = \vec{\mathbf{A}}\mathbf{X}$ where $\vec{\mathbf{A}}$ is a 6×6 matrix and \mathbf{X} is a column vector containing the six unknowns to be solved in terms of \mathbf{C} , a column vector specified by the incident wave.

The formal solution (3.16) must be supplemented by Snell's law, which determines e_k the directions of the reflected and transmitted waves in terms of the incident angles. These laws follow from the continuity of the frequency ω and the tangential wavenumber k_t at the magnetopause.

$$\omega = \mathbf{k}^i \cdot (\mathbf{U}_2 - \mathbf{V}_{A2}) = \begin{cases} \mathbf{k}^d \cdot (\mathbf{U}_\alpha \mp \mathbf{V}_{A\alpha}), & \text{Alfvén waves;} \\ k^d V_{F,S}^{ph} + \mathbf{k}^d \cdot \mathbf{U}_\alpha, & \text{Fast and slow waves.} \end{cases} \quad (3.17)$$

where $\alpha = 1, 2$ and again subscript 1 and 2 denote side 1 and side 2; the wavevector \mathbf{k}^i is for the incident Alfvén wave and \mathbf{k}^d for emanating waves; V_A is the Alfvén speed, $V_{F,S}^{ph}$ is the phase velocity for the fast and slow waves given in Chapter 2 by Equation (2.2).

Equations (3.16) along with Snell's law (3.17) are the governing equations developed to calculate the reflection and transmission amplitude ratios of emanating waves. These equations form a system of six linear inhomogeneous algebra equations that will be solved numerically with the given parameters Θ_1 , β_1 and ρ_2/ρ_1 .

3.1.3 Reflection and Transmission Amplitude Ratios

Kan and Sun [1985] proposed that an enhanced magnetosphere convection, due to enhanced dayside reconnection, propagates toward the ionosphere by Alfvén waves. These waves subsequently reflect from the ionosphere. The reflected Alfvén wave from the ionosphere is taken to be the incident wave at the open magnetopause. Thus, Alfvén waves are bouncing between the ionosphere and magnetopause. The wavelength along the magnetic field lines is of order of the distance between the ionosphere and the magnetopause. The perpendicular wavelength in the ionosphere is determined by the convection scale length that ranges from 10's km to a few 1000 km. The short perpendicular wavelength indicates that $k_{||} \ll k_{\perp}$, so that the typical wave normal angle for the incident Alfvén wave $\theta = \arctan(k_{||}/k_{\perp}) \sim 5^\circ$. The electric field associated with such an Alfvén wave is primarily in the dawn to dusk direction, which is along the z axis in Figure (3.1). The amplitudes of the emanating waves depend on the incident angles (θ, ϕ) and three independent magnetopause parameters ($\rho_r = \rho_2/\rho_1$, Θ_1 and β_1) which determine the configuration of the open magnetopause. The magnetopause parameters vary greatly depending on solar-wind parameters and tailward position along the high-latitude open magnetopause. In our calculations, we have chosen a particular value of $\Theta_1 (= 5^\circ)$, i.e., the magnetic field B_1 in the solar wind is assumed to be almost normal to the magnetopause.

The transient behavior of the magnetosphere-ionosphere (M-I) coupling is known to be governed by Alfvén waves [e.g., Kan and Sun, 1985]. For the M-I coupling, only the reflection and transmission amplitude ratios of the Alfvén wave electric fields will be presented, although the formulation and solution schemes are applicable to other emanating waves. Numerical results are presented in graphic form in which the electric field amplitudes of reflected and transmitted Alfvén waves are plotted against one parameter, while holding other parameters constant.

Figure (3.2) shows the dependence of Alfvén wave reflection characteristics on the density ratio ρ_2/ρ_1 of the magnetosphere and solar wind densities, for an Alfvén wave incident from the magnetospheric side. The fixed parameters and incident conditions are $\Theta_1 = 5^\circ$, $\beta_1 = 2.5$, $\theta = 5^\circ$ and $\phi = 0^\circ$.

Panel (3.2a) shows the normal angle Θ_2 as a function of the density ratio ρ_r . Θ_2 , the angle of the ambient magnetic field B_2 in the magnetosphere to the normal of the magnetopause, is determined from equation (3.12) with given parameters ρ_r , Θ_1 and β_1 . Θ_2 does not change very much as the density ratio ρ_r varies. The magnetic field B_1 , near normal to the magnetopause ($\Theta_1 = 5^\circ$) in the solar-wind, is sharply bent to B_2 towards the magnetopause in the magnetosphere ($\Theta_2 \sim 50^\circ$).

Panel (3.2b) shows the reflection amplitude ratio of the Alfvén wave electric field $R_E = \delta E_{A2}^d / \delta E_{A2}^{in}$ (the electric field of the reflected Alfvén wave normalized by the electric field of the incident Alfvén wave). The modulus $|R_E|$ is given by the solid curve lying between 0 and 1, and the phase α measured in degrees is given by the dashed line on a scale ranging from 0° and 180° . The modulus $|R_E|$ of reflection amplitude ratio decreases monotonically from 1 to 0 as the density ratio ρ_2/ρ_1 increases from 0 to 1. Since the electric field carried by a transverse Alfvén wave lies on the B-k plane and is perpendicular to the magnetic field B, the electric fields of both the incident and reflected Alfvén wave are primarily along the

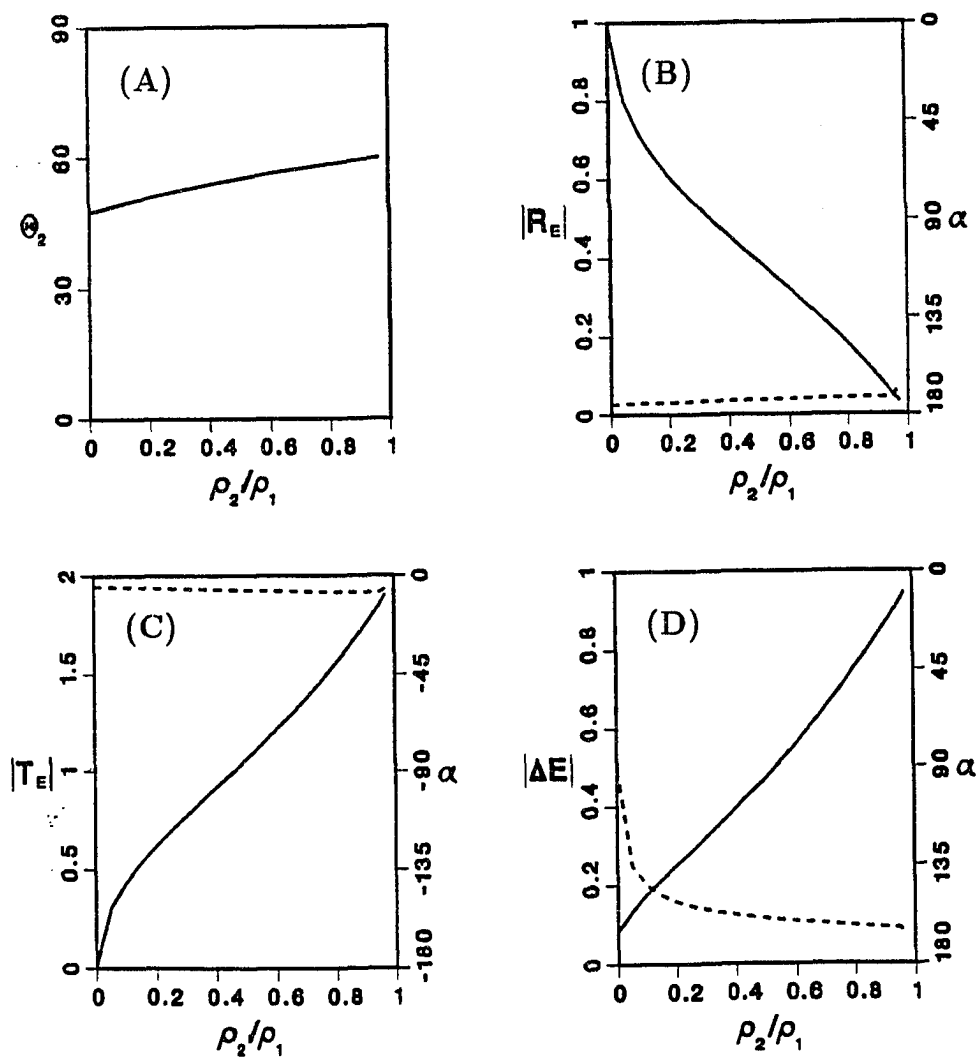


Figure 3.2 Dependence of reflection and transmission amplitude ratios on the magnetosphere-solar wind density ratio ρ_2/ρ_1 , for fixed values of $\Theta_1 = 5^\circ$, $\beta_1 = 2.5$, $\theta = 5^\circ$ and $\phi = 0^\circ$. (A) The field normal angle Θ_2 (In degrees) of the open magnetopause structure as a function of the density ratio ρ_r . (B) The Alfvén wave reflection amplitude ratio $R_E = (\text{Electric field of the reflected Alfvén wave})/(\text{Electric field of the incident Alfvén wave})$. The solid curve is for the modulus $|R_E|$; the dashed curve is for the phase α (In degrees). (C) The Alfvén wave transmission amplitude ratio $T_E = (\text{Electric field of the transmitted Alfvén wave})/(\text{Electric field of the incident Alfvén wave})$, using the same notation as in (B). (D) Changes of Alfvén wave electric fields across the open magnetopause $\Delta E = 1 + R_E - T_E$ explained in the text (from Cao and Kan, 1990).

z-axis when the incident wave normal angle θ is very small. The phase angle α , which is near 180° for the density ratio ranging from 0 to 1, indicates that the electric field of the reflected Alfvén wave is almost anti-parallel to that of the incident Alfvén wave. When the density ratio ρ_2/ρ_1 approaches zero, the reflection amplitude ratio R_E becomes equal to -1. This tendency is understandable. The magnetosphere-solar wind density ratio $\rho_2/\rho_1 \sim 0$ ($\rho_1 \gg \rho_2$) means the solar-wind inertia is much larger than that in the magnetosphere so that the electric field in the solar-wind is somehow unchanged by the impinging Alfvén wave from the magnetosphere and the total Alfvén wave reflection occurs.

Panel (3.2c) shows the transmission amplitude ratio of the Alfvén wave electric field $T_E = \delta E_{A1}^d / \delta E_{A2}^{in}$ (the electric field of the transmitted Alfvén wave normalized by the electric field of the incident Alfvén wave). The dependence of the transmission amplitude ratio T_E on the density ratio ρ_2/ρ_1 is in contrast with that of the reflection amplitude ratio R_E . The modulus $|T_E|$ represented by the solid line increases monotonically from 0 to 2 as the density ratio increases from 0 to 1. The phase α , which is near zero degrees, indicates that the electric field associated with the transmitted wave is parallel to that of the incident wave.

Panel (3.2d) shows a change of the Alfvén wave electric fields across the open magnetopause $\Delta E = 1 + R_E - T_E$. This electric field change is associated with the incident, reflected and transmitted Alfvén waves. Since the total tangential electric field is conserved across the magnetopause, the change of electric fields ΔE associated with the Alfvén waves also measures the amplitude of emanating fast and slow waves.

Figure (3.3) shows the dependence of wave reflection characteristics on β_1 , the solar-wind thermal pressure to magnetic pressure ratio, for an Alfvén wave incident from the magnetospheric side. The reflection and transmission are computed for β_1 ranging from 0 to 10, with the density ratio $\rho_2/\rho_1 = 0.05$. Other parameters and incident conditions are kept the same as in Figure (3.2). At the magnetopause, the thermal pressure in the solar-wind is balanced

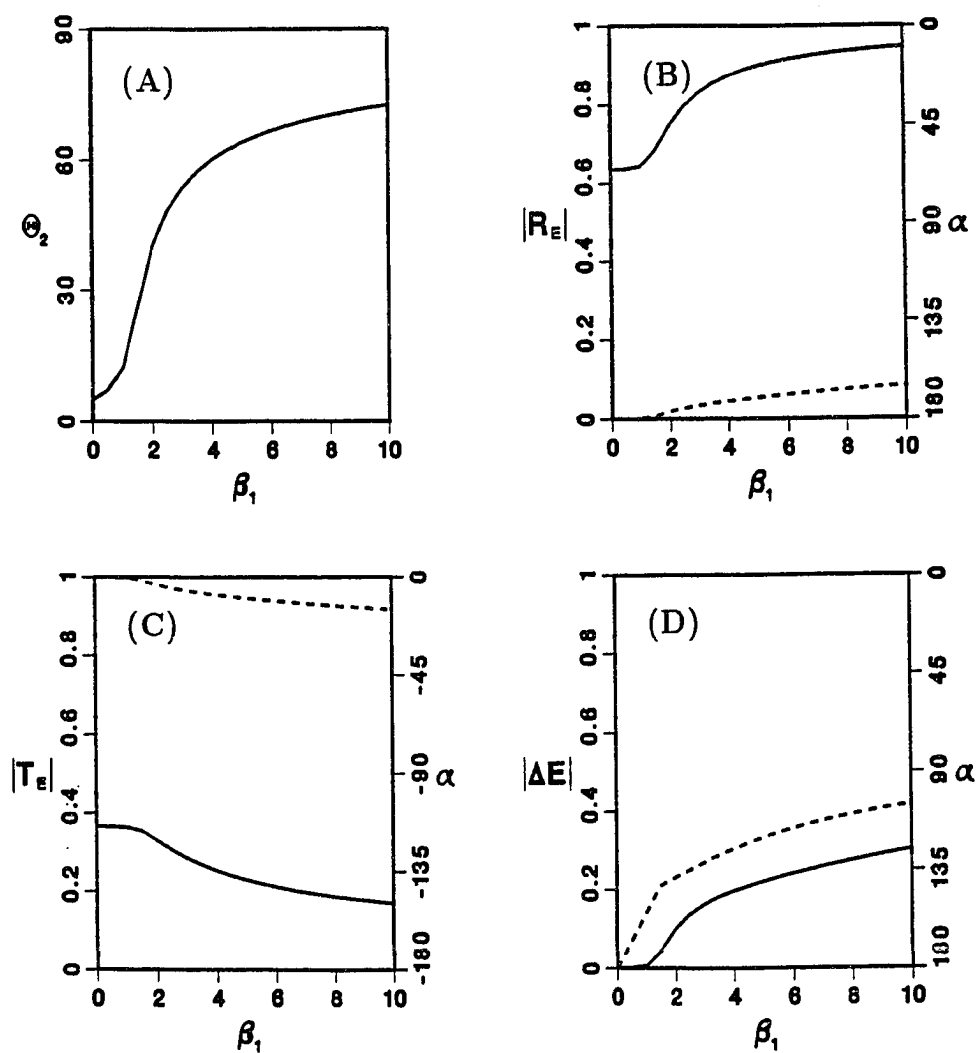


Figure 3.3 Dependence of reflection and transmission amplitude ratios on β_1 (the solar-wind thermal pressure to magnetic pressure ratio) for a given density ratio $\rho_2/\rho_1 = 0.05$. Same as Figure (3.2), except showing the dependence on β_1 (from Cao and Kan, 1990).

primarily by the magnetic pressure in the magnetosphere. As β_1 in the solar-wind increases from 0, the magnetic field lines bend increasingly toward the magnetopause on the magnetospheric side. This is shown in Panel (3.3a) as the normal angle Θ_2 increases and approaches 90° . Panel (3.3b) shows the reflection amplitude ratio of the Alfvén wave electric field R_E . When $\beta_1 = 0$, the ambient magnetic field lines go through the magnetopause without bending ($\Theta_2 \approx \Theta_1 = 5^\circ$) and the reflection amplitude ratio R_E is about -0.63 . As β_1 increases, the magnetic field lines bend more and more as shown in Panel (3.3a), and R_E approaches -1 . The more the magnetic field is bent at the magnetopause, the closer R_E is to -1 . The phase angles, which are close to 180° , suggest that the electric fields of reflected and incident Alfvén waves are almost anti-parallel.

The dependences of reflection amplitude ratios on the density ratio and the bending of magnetic field may be understood in a simplified situation as discussed below. When there are no emanating fast waves and no plasma flows, the Alfvén wave reflection at a discontinuity is the same as that in transmission line theory [Budden, 1985] and is given in chapter 2 by equation (3.18)

$$R_E = \frac{\Sigma_{A2}/\Sigma_{A1} - 1}{\Sigma_{A2}/\Sigma_{A1} + 1} \quad (3.18)$$

where $\Sigma_A = c^2/(4\pi V_A) = c^2\sqrt{\rho}/4\pi/B$ is the conductance of Alfvén wave, i.e., the current perpendicular to the ambient magnetic field $\mathbf{J}_\perp = \Sigma_A \mathbf{E}$ [e.g., Mallinckrodt and Carlson, 1975]. The continuity of the normal magnetic field at the magnetopause requires $B_n = B_2 \cos \Theta_2 = B_1 \cos \Theta_1$ so that the conductance ratio of two media in Equation (3.18) can be written as

$$\frac{\Sigma_{A2}}{\Sigma_{A1}} = \frac{\sqrt{\rho_2}/B_2}{\sqrt{\rho_1}/B_1} = \sqrt{\frac{\rho_2 \cos \Theta_2}{\rho_1 \cos \Theta_1}} \quad (3.19)$$

when the density ratio ρ_2/ρ_1 is much smaller than 1 or the ambient magnetic field bending becomes greater ($\cos \Theta_2 \ll \cos \Theta_1$), the conductance of the solar wind Σ_{A1} is much larger than the conductance Σ_{A2} in the magnetosphere and R_E in Equation (3.18) goes to -1 .

Panel (3.3c) shows the dependence of transmission amplitude ratio T_E on β_1 . T_E decreases monotonically as β_1 increases. Panel (3.3d) shows the dependence of electric field change due to the generation of emanating fast and slow waves. When $\beta_1 = 0$, there are no fast and slow waves generated at the magnetopause ($\Delta E = 0$). As β_1 increases, the magnetic field line is bent increasingly at the open magnetopause. The curvature of the magnetic field line couples the Alfvén wave to the fast and slow waves, resulting in the generation of emanating fast and slow waves and the increase of ΔE .

Figure (3.4) shows the dependence of the reflection and transmission amplitude ratios on the incident angles (θ, ϕ) with the fixed magnetopause parameters $\Theta_1 = 5^\circ, \rho_2/\rho_1 = 0.05$ and $\beta_1 = 2.5$. Panels (3.4a) and (3.4b) show respectively the reflection and transmission amplitude ratios as a function of the incident wave normal angle θ , with an incident wavevector \mathbf{k} on x - z plane (the azimuthal angle $\phi = -\Theta_2$). When $\theta = 90^\circ$, the ambient magnetic fields and the incident wavevector \mathbf{k}^i are coplanar with the x -axis normal to the magnetopause, and the incompressible Alfvén waves do not couple to the compressional fast and slow waves. The corresponding reflection and transmission amplitude ratios are equal to -0.63 and 0.37 , which are the same as those of Panels (3.3b) and (3.3c) in the case of $\beta_1 = 0$ in which there are no bending of magnetic field lines and no compressional waves. When θ is not equal to 90° , Alfvén waves are no longer decoupled with the compressional fast and slow waves. The emanating fast and slow waves would carry away part of incident wave electric field and result in the sharp decrease in the amplitudes of reflected and transmitted Alfvén waves. As the incident wave normal angle θ decreases further toward a smaller value, the fast wave generated by an incident Alfvén wave at the magnetopause must be evanescent and its amplitude will drop exponentially with distance away from the magnetopause [Budden, 1985; McKenzie and Westphal, 1970]. As a result, the amplitudes of emanating Alfvén waves will rise up to a new level. Although the electric profiles shown in Panels (3.4a) and (3.4b) are for a special

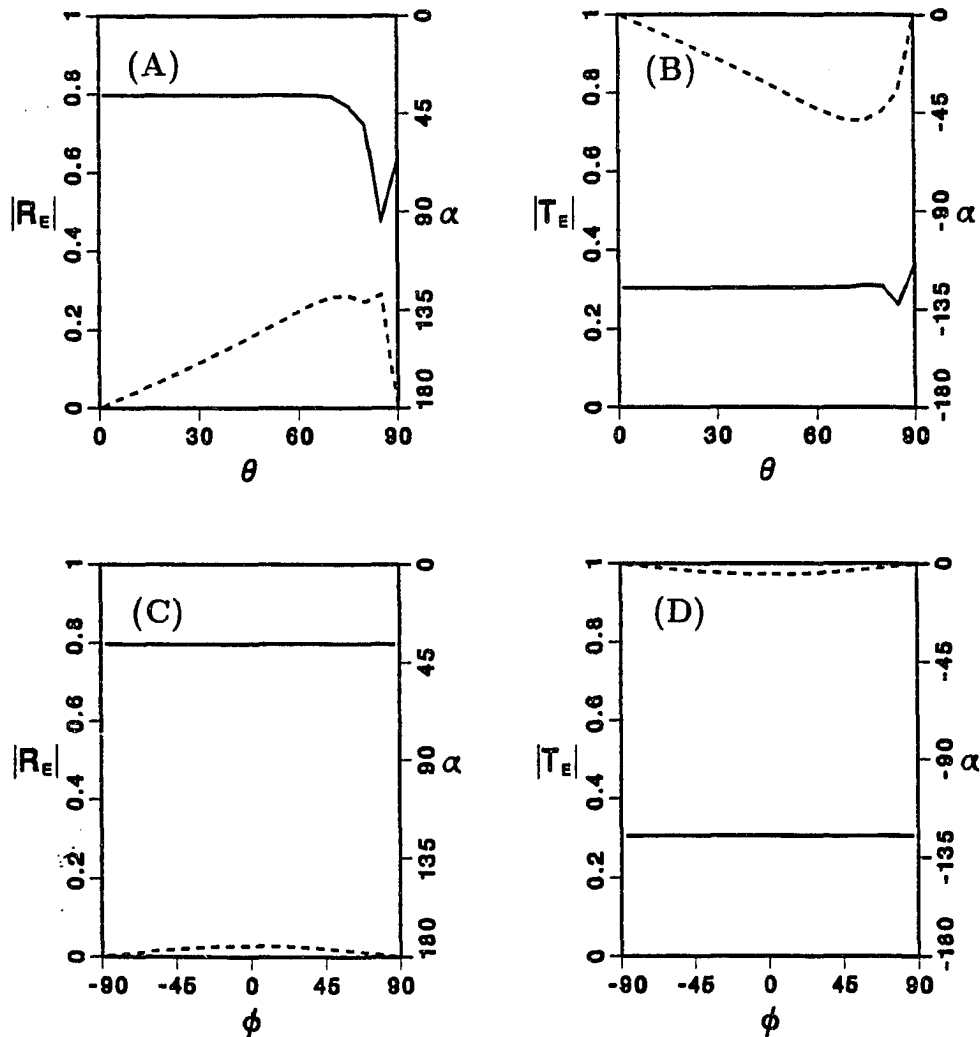


Figure 3.4 Dependence of reflection and transmission amplitude ratios on the incident angles of Alfvén waves (θ and ϕ in degrees). The magnetopause parameter values are $\rho_2/\rho_1 = 0.05$, $\beta_1 = 2.5$, $\Theta_1 = 5^\circ$. (A) and (B), using the same notation as in Fig. (3.2B) and (3.2C), show respectively the reflection and transmission amplitude ratios for the Alfvén wave electric field as a function of the incident wave normal angle θ with an incident wavevector on the x - z plane ($\phi = -\Theta_2$). (C) and (D) are the same as (A) and (B), except showing the dependence on the azimuthal angle ϕ for a given wave normal angle $\theta = 5^\circ$ (from Cao and Kan, 1990).

case in which the incident wavevector is on the x - z plane, the computer results have shown similar features for other cases. Panels (3.4c) and (3.4d) show the dependence of reflection and transmission amplitude ratios on the azimuthal angle ϕ for a given wave normal angle $\theta = 5^\circ$. Both reflection and transmission amplitude ratios are insensitive to the azimuthal angle change.

3.1.4 Summary

In summary, I have presented a linear analysis of reflection and transmission of the Alfvén wave incident on the open magnetopause from the magnetospheric side. The results show that the electric fields of reflected Alfvén waves are mainly controlled by the magnetosphere-solar wind density ratio, the bending of magnetic field lines and the incident wave normal angle θ . When the change in the plasma density and the change in the magnetic field across the magnetopause become larger, the magnetopause behaves increasingly more like a perfect reflector to the Alfvén wave incident from the magnetosphere because the Alfvén wave conductance in the solar-wind is much greater than the wave conductance in the magnetosphere. At the near-earth open magnetopause, the magnetosphere-solar wind density ratio is around 0.05, and the magnetic field is expected to rotate more than 45° . The corresponding reflection amplitude ratio of the Alfvén wave electric field R_E ranges from -0.8 to -1.0 . This means that a large part of the incident wave electric field must be canceled by the reflected Alfvén wave field, so that the electric field in the solar-wind is more or less unchanged by the presence of the Alfvén wave incident on the magnetopause from the magnetospheric side.

3.2 Reflection of Alfvén waves From the Plasma Sheet

In this section, reflection of an Alfvén wave from the plasma sheet on closed field lines is investigated. In the previous section, I have discussed the Alfvén wave reflection at the open magnetopause. On open field lines the solar wind inertia is sufficiently large so that the solar wind flow is largely unchanged by the presence of the Alfvén wave incident on the open magnetopause. Thus the amplitude reflection coefficient of the wave electric field is near -1 . Reflection from the plasma sheet on closed field lines is quite different since the density change across the plasma sheet is somewhat smaller. The existence of the cross-tail current in the plasma sheet causes a sharp bending of the magnetic field line near the equatorial plane. The field curvature near the equatorial plane can couple the incompressible Alfvén wave to a compressional slow wave, resulting in partial reflection of Alfvén waves from the plasma sheet. The reflection mechanism described in this section is purely due to field curvature near the equatorial plane.

The best observational evidence for the Alfvén and slow wave coupling is the magnetotail vortices first discovered by Hones *et al.* [1978]. The vortices manifest themselves with the large rotations in plasma flow direction in the Earth's magnetotail. The extensive analyses of observational data from *ISEE* spacecraft [Hones *et al.*, 1983; Saunders *et al.*, 1981; 1983] have indicated that the vortices are a hybrid form of MHD wave. Some of their characteristics are those associated with the Alfvén wave, but in other respects they resemble slow mode signals. To explain the hybrid polarization of MHD wave detected in the magnetotail vortices, Southwood and Saunders [1985] proposed the curvature coupling mechanism, which could well be important in the region where the vortex events have been reported. When the Alfvén wave from the ionosphere propagates through the plasma sheet, the curvature coupling near the Equator will lead to the reflected Alfvén wave propagating back towards the ionosphere and

the hybrid signal near the Equator. The characteristics of the wave reflection and the hybrid vortices depend on the field line curvature, which is expected to change with the tailward distance as the field lines become increasingly distended. The main purpose of the study in this section is to determine the dependence of the wave characteristics on the tailward distance.

Figure (3.5a) is a sketch of the closed magnetic field line in the meridian plane. The important features are the large curvature near the equatorial plane and the straighter field off the Equator as a consequence of the distended configuration. Consider a pair of identical but oppositely propagating Alfvén waves incident on the plasma sheet simultaneously from opposite ionospheres. One can expect that two reflected Alfvén waves, identical but opposite in the direction, should propagate back toward the conjugate ionospheres. The net reflected wave in one hemisphere consists of the reflected wave due to an incident wave from the same hemisphere, and the transmitted wave due to an incident wave from the opposite hemisphere. It should be noted that the effect is the same as if the plasma sheet had an equivalent reflection coefficient equal to 1 when the incident Alfvén wave from one hemisphere propagates across the plasma sheet to the other hemisphere without reflection.

The equilibrium field configuration is maintained by plasma pressure

$$\nabla p = \mathbf{J} \times \mathbf{B} = -\nabla_{\perp} \frac{B^2}{8\pi} + \frac{B^2}{4\pi R_c} \mathbf{n} \quad (3.20)$$

where R_c is the radius of the field line curvature and \mathbf{n} is the unit vector perpendicular to the field line. In the equatorial plane the pressure gradient is predominantly balanced by the field curvature force, the second term on the right side of equation (3.20). In the nearly straight field region off the equatorial plane, the curvature force may be neglected and the pressure is balanced mainly by the magnetic pressure. Figure (3.5b) shows a simplified field line, consisting of the straight line segment and the field line arc near the equatorial plane.

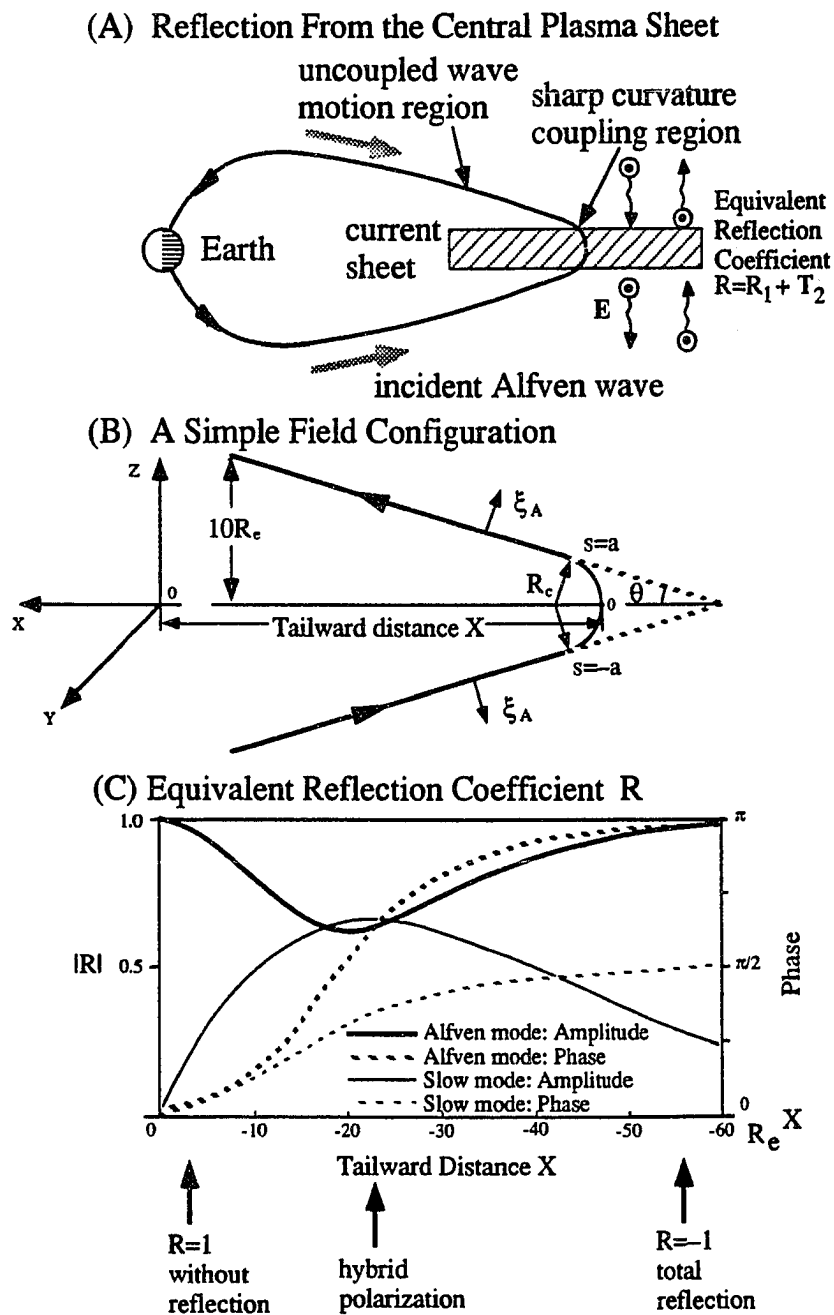


Figure 3.5 Reflection of Alfvén waves from the central plasma sheet. (A) Sketch of the closed magnetic field lines in the central plasma sheet. (B) A simple field line consisting of the straight line off the equatorial plane and the field line arc near the equatorial plane. s is the coordinate along the field line, θ is the incline angle of the straight field line to the equatorial plane and ξ_A denotes the Alfvén shear displacement. X is the distance of field line crossings from the Earth. (C) The reflection coefficients of Alfvén waves and the amplitudes of slow waves.

As discussed in the previous section, the Alfvén wave from the ionosphere has a short perpendicular wavelength compared to the parallel wavelength along the magnetic field lines, so that the wave electric field is primarily in the dawn-dusk direction. In the short perpendicular wavelength limit the fast wave becomes evanescent. Therefore, the incompressible Alfvén mode may be coupled only to the compressional slow mode in the short perpendicular wavelength limit. The coupling can be simply understood. In the short perpendicular wavelength out of the meridian, the Alfvén wave electric field is along the dawn-dusk direction out of the meridian, and the wave displacement ξ_A is perpendicular to the field line in the meridian as shown in Figure (3.5b). Displacement vectors ξ_A perpendicular to the magnetic field converge if the field bends in the meridian. Even if the displacement does not vary in amplitude the vector has a finite divergence. Thus, in the sharply curved field near the equatorial plane an Alfvén wave meridional motion creates a compression that serves as a source of the slow mode wave. The coupling is entirely due to field curvature. In a straight field geometry off the equatorial plane there is no coupling.

The governing equations describing the curvature coupling of Alfvén and slow mode waves were first derived by Southwood and Saunders [1985], to explain the hybrid polarization of MHD wave detected in the magnetotail vortices by *ISEE* spacecraft [Hones *et al.*, 1983; Saunders *et al.*, 1981; 1983]. The similar equations were used later by Miura *et al.* [1990] to investigate the ballooning instability for a curved magnetic field line configuration. Let δp stand for the plasma pressure perturbation and ξ_A for the plasma perpendicular displacement in the meridian plane. The coupling equation can be written as

$$\rho \left(\omega^2 + V_A^2 \frac{\partial^2}{\partial s^2} \right) \xi_A = \frac{2}{R_c} \delta p \quad (3.21)$$

$$\left(\frac{\omega^2}{C_S^2} + \frac{\partial^2}{\partial s^2} \right) \delta p = -\frac{\rho \omega^2 V_A^2 - C_S^2}{R_c C_S^2} \xi_A - \frac{\rho V_A^2}{R_c} \frac{\partial^2}{\partial s^2} \xi_A \quad (3.22)$$

where ρ is the plasma mass density, ω is the wave frequency, R_c is the radius of field line curvature and s is a coordinate along the background magnetic field line. Same as those defined in chapter 2, V_A is the Alfvén velocity, C_S is the sound speed, C_{SL} is the slow mode wave speed and $\omega^2 = V_A^2 k_{\parallel}^2$ is the dispersion relation for the incident Alfvén wave. The coupling equations (3.21) and (3.22) are similar to those given by Miura *et al.* [1990]. Note that the factor 2 in (3.21) and the last term in (3.22) are missing in the coupling equations given by Southwood and Saunders [1985].

The left side of equation (3.21) describes the Alfvén wave, which is characterized by the shearing motion ξ_A . The term on the right side indicates a coupling of the Alfvén wave motion and pressure oscillation. The left side of equation (3.22) is slow mode wave equation. The term on the right side shows that any Alfvén wave motion represented by ξ_A drives a slow mode wave. The coupling terms on the right sides of equations (3.21) and (3.22) are inversely proportional to the radius of field line curvature. Evidently the Alfvén waves with long wavelengths are most effectively coupled to the slow mode waves along the sharply bent field line.

Near the equatorial plane the incident Alfvén waves are coupled to the slow mode waves in a field arc segment ranging from $s = -a$ to $s = a$, as shown in Figure (3.5b). Along the straight field line off the equatorial plane, the incident Alfvén wave, reflected Alfvén wave and slow mode wave can propagate without coupling. The coupled equations (3.21) and (3.22) can be combined into a single differential equation for the displacement ξ_A . This fourth-order differential equation for ξ_A may be written in a dimensionless form

$$\left[\frac{\partial^4}{\partial \bar{s}^4} + \left(\frac{2\beta + 1}{\beta} \delta + \frac{2}{\delta} \right) \frac{\partial^2}{\partial \bar{s}^2} + \frac{\beta + 1}{\beta} \delta^2 + 2 \frac{1 - \beta}{\beta} \right] \xi_A = 0 \quad (3.23)$$

where the normalized coordinate $\bar{s} = s \sqrt{k_{\parallel} / R_c}$, the ratio of the plasma pressure to the magnetic pressure $\beta = C_S^2 / V_A^2$, and the normalized parallel wavevector $\delta = k_{\parallel} R_c$. The

normalized half-thickness of the current sheet $\bar{a} = a/R_c$. With given parameters of β and δ , the equation (3.23) may be solved analytically. The amplitudes of the reflected waves in the straight line regions can be determined by matching the solution of equation (3.23) at the boundaries $s = \pm a$ through the continuity of the displacement and its first derivative.

The amplitudes of reflected waves depend on the current thickness \bar{a} and the two parameters of δ and β . In the plasma sheet, the field line curvature is expected to increase with the tailward distance. For the simple field line configuration shown in Figure (3.5b), the half thickness of the current sheet $\bar{a} = a/R_c = \pi/2 - \theta$, where θ is an inclined angle of the straight field line to the equatorial plane. The parallel wavelength of incident Alfvén wave is about the length of the straight field line, $\lambda_{||} \sim 10R_e/\sin \theta$. Assuming the half thickness of current sheet a equal to 2 Earth radii, one can determine the parameter $\delta = k_{||}R_c = (k_{||}a)(R_c/a) \approx \sin \theta/(\pi/2 - \theta)$. The analysis in this section doesn't require an explicit field model. However, without the explicit field model, it is uncertain what is the relationship among θ , β and the tailward distance x of field line crossings. In this study, θ and β will be treated as two independent parameters.

The inclination angle θ is expected to be a function of the tailward distance x of field line crossings, as the field lines become increasingly distended in the magnetotail. As an estimation, I assume the β ($= 0.5$) is constant and the inclination angle $\theta = \pi/2 \exp(x/20)$, where the distance x of field line crossings is measured in Earth's radii. The inclination angle θ ranges from $\pi/2$ near the Earth to 0 far down magnetotail. $\theta \approx \pi/2$ near the Earth means the field line is a straight line. $\theta \approx 0$ corresponds to the reversal field configuration in the magnetotail. The coupling equations are then solved numerically as a function of the tailward distance x .

Figure (3.5c) shows the calculated reflection coefficient as a function of tailward distance x of field line crossings. In Figure (3.5c), the solid curves are for the amplitudes of equivalent

reflection coefficients, and the dashed lines are for the phase angles. The thick curves represent those for the reflected Alfvén waves. Near the Earth, the magnetic field lines are almost straight and the radius of field line curvature is much larger than the wavelength. Thus, the Alfvén wave can propagate through the near-Earth plasma sheet without reflection ($R_1, R_2 = 0; T_1, T_2 = 1$). The net reflected wave in one hemisphere consists of the reflected wave due to an incident wave from the same hemisphere, and the transmitted wave due to an incident wave from the opposite hemisphere. Therefore, the equivalent reflection coefficient of the plasma sheet $R = R_1 + T_2 = 1$. In contrast, the incident Alfvén wave must negotiate a sharply bent portion of the field line in the magnetotail, resulting in a total reflection ($R_1, R_2 = -1; T_1, T_2 = 0$). Correspondingly, the equivalent reflection coefficient $R = R_1 + T_2 = -1$. The amplitude of slow mode wave peaks near 20 Earth radii in compensation with the minimum amplitude of reflected Alfvén wave.

In summary, the results in this section show that the Alfvén wave reflection coefficients range from 1 to -1 depending on which portion of the plasma sheet is considered. In the near-earth plasma sheet where the magnetic field lines are less bent, the incident Alfvén wave from the ionosphere can propagate across the plasma sheet almost without reflection. On the other hand, in the magnetotail region, the incident Alfvén wave negotiating a sharply bent portion of the field line causes a total reflection. The corresponding reflection coefficient for the wave electric field is near -1 . The strong coupling of the Alfvén and slow mode waves is found to occur at a tailward distance of $20R_e$, where the amplitudes of the Alfvén and slow waves are comparable. This result is especially helpful in predicting the occurrence of the magnetotail vortices, which have the hybrid polarizations of both Alfvén and slow mode waves and have been widely observed in the magnetotail.

CHAPTER 4

Effect of Field-Aligned Potential Drops on the Magnetosphere-Ionosphere Coupling

The purpose of the study in this chapter is to examine the effect of field-aligned potential drops on the magnetosphere-ionosphere (M-I) coupling on a global scale in a steady state. The time-independent global model developed in this study is an important step toward the development of the time-dependent global M-I coupling model.

It is well known that the ionosphere and magnetosphere are coupled as a consequence of field-aligned currents. Due to an enhanced magnetospheric convection, the field-aligned currents are enhanced as required by the ionosphere to overcome the ion drag and to speed up the ionospheric convection. For the upward field-aligned current density at the ionospheric altitude to exceed the loss cone limit on precipitating magnetospheric electron flux, potential drops along field lines are required to accelerate the electrons and thereby to increase the downward electron flux inside the loss cone [Knight, 1973]. As the accelerated auroral electrons impinge on the atmosphere, the ionization and hence the ionospheric conductivities are enhanced. On the other hand, the enhanced field-aligned currents lead to the enhanced cross-field currents in the magnetospheric dynamo region, exerting a loading effect on the magnetospheric convection.

In this chapter, we examine the effects of field-aligned potential drops on the convection pattern, the field-aligned current distribution and the ionospheric conductance in self-consistent calculation under the assumption of either a constant current generator or a constant voltage generator. A number of global ionospheric convection models have been developed in recent years, but none has included the effect of field-aligned potential drops explicitly in the model. These include the time-independent convection models developed by Vasyliunas [1970; 1972],

Yasuhara *et al.* [1983], Kan and Kamide [1985], Barbosa [1985] and Atkinson [1986] as well as the time-dependent models developed by Harel *et al.* [1981], Miura and Sato [1980] and by Kan and Sun [1985]. The only model that includes field-aligned potential drops due to an anomalous resistivity is the model developed by Lysak and Dum [1983] and modified later by Lotko *et al.* [1987; 1988], but it is a local model that is complementary to the global model discussed in the present study.

The principal elements of our model include: (1) an ionospheric response characterized by an Ohm's law and current continuity, (2) a magnetospheric convection field supported either by the constant current generator or by the constant voltage generator, (3) a linear current-voltage relation characterizing the plasma response in the intervening region along the magnetic field, (4) the auroral conductivity enhancement in regions of strong upward field-aligned currents. The main contribution of this study is to bring the above ideas together and thereby to investigate the effect of field-aligned potential drops on the global magnetosphere and ionosphere coupling. The chapter is organized as follows. In section 1 the basic model equations are developed. In section 2 the consequence of field-aligned potential drops for the local convection and field-aligned current density is briefly discussed. Section 3 contains the numerical results that show the effect of field-aligned potential drops on the global magnetosphere-ionosphere coupling. Finally, section 5 contains a summary and further discussion of the results.

4.1 Basic Equations

In this section a set of equations is derived for modeling the effect of field-aligned potential drops on the magnetosphere-ionosphere (M-I) coupling. In the present study, we attribute the potential drops along magnetic field lines to the enhanced magnetospheric convection, irrespective of how the field-aligned potential drops are supported. The field-aligned potential

drops are included by assuming the potential difference between the magnetosphere and the ionosphere depends on the field-aligned current at the ionosphere through a linear current voltage relationship [e.g. Lyons, 1980; Lotko *et al.*, 1987; Lotko and Schultz, 1988; Kan and Cao, 1988]

$$\begin{aligned}\Phi_{\parallel} &= \alpha(J_{\parallel} - J_0) & \text{if } J_{\parallel} > J_0 \\ \Phi_{\parallel} &= 0 & \text{if } J_{\parallel} < J_0\end{aligned}\tag{4.1}$$

where the parameter α may be viewed as a constant resistivity which ranges from 1 to 10 kV/(\(\mu\text{A}/\text{m}^2\)). The offset current J_0 is the electron thermal flux in the loss cone and is set to 0.1 \(\mu\text{A}/\text{m}^2\). We have chosen $J_{\parallel} > 0$ for upward currents flowing away from the ionosphere. In a steady state $\nabla \times \mathbf{E} = 0$, so that the electric field can be written in terms of a scalar potential, *i.e.*,

$$\Phi_{\parallel} = \Phi_i - \Phi_m\tag{4.2}$$

where $\Phi_{\parallel} > 0$ is for potential rise toward the ionosphere, Φ_m and Φ_i are the potentials on the magnetospheric and ionospheric sides of the intervening region where the field-aligned potential drop Φ_{\parallel} exists. The sign conventions for J_{\parallel} and Φ_{\parallel} are chosen to ensure that the parallel electric field E_{\parallel} is upward when the field-aligned current J_{\parallel} is upward on the magnetic field lines.

The phenomenological relation (4.1) applies primarily to currents in "inverted V" precipitation regions [Frank and Ackerson, 1971], where the net field-aligned current is directed out of the ionosphere. In these regions the current is carried primarily by accelerated kilovolt electrons, and the parameter α lies in the range 1 to 10 kV/(\(\mu\text{A}/\text{m}^2\)) [Knight, 1973; Fridman and Lemaire, 1980] as we have assumed. Currents near the edges of auroral precipitation regions or in narrow channels may not, however, be adequately described by this relation. The linear current-voltage relation (4.1) is clearly an oversimplification of the problem; its use here should be regarded as a first step toward a more detailed analysis.

The field-aligned current density $J_{||}$ in the ionosphere is related to the ionospheric electric field \mathbf{E}_i through the current continuity and the Ohm's law

$$-J_{||} = \nabla \cdot \mathbf{I}_i \quad (4.3)$$

$$\mathbf{I}_i = \Sigma_p \mathbf{E}_i + \Sigma_h \cdot \mathbf{B}_0 \times \mathbf{E}_i / B_0$$

where the field-aligned current $J_{||}$ is chosen positive upward, \mathbf{I}_i is the height-integrated ionospheric current, $\mathbf{E}_i = -\nabla\phi_i$ is the transverse electric field in the ionosphere, B_0 is the geomagnetic field assumed uniform in the ionosphere, Σ_p and Σ_h are the ionospheric height-integrated Pedersen and Hall conductances. Note that the geomagnetic field \mathbf{B}_0 is assumed to be perpendicular to the ionosphere. This approximation is reasonable at latitudes higher than 60° . Otherwise, a factor of $\cos \Theta$ would arise on the left side of (4.3), where Θ is the zenith angle of the magnetic field relative to the normal direction of the ionosphere.

The ionospheric height-integrated conductance consists of the solar conductance Σ_s , the diffuse auroral conductance Σ_d and the discrete auroral conductance Σ_a . By balancing the ionization production rate with the recombination rate in the continuity equation in the ionosphere, the aurora-enhanced ionospheric Hall conductance can be written as [e.g., Kan and Kamide, 1985]

$$\begin{aligned} \Sigma_h &= [\Sigma_0^2 + \gamma J_{||} \Phi_{||}]^{1/2} & J_{||} > J_0 \\ \Sigma_h &= \Sigma_0 & J_{||} < J_0 \end{aligned} \quad (4.4)$$

where $\Sigma_0 = [\Sigma_s^2 + \Sigma_d^2]^{1/2}$ is the background conductance consisting of the solar conductance Σ_s and the diffuse auroral conductance Σ_d , and J_0 is the offset current chosen to be the same as that in (4.1). The enhanced conductivity is proportional to the energy flux $J_{||} \Phi_{||}$ of precipitating electrons. γ is a constant relating to the ionization efficiency and is set to $120 \text{ mho}^2/(\text{kV} \cdot \mu\text{A}/\text{m}^2)$. The ratio of Hall to Pedersen conductances is assumed for simplicity to

be constant ($\Sigma_h/\Sigma_p = 1.5$) in the model, although it is known to depend on the energy of the precipitation electrons.

Equations (4.1) to (4.4) are the governing equations of the proposed steady-state M-I coupling model including the field-aligned potential drop effect. These equations form a system of nonlinear differential equations that will be solved numerically by an iteration scheme.

4.2 Local Effect of Field-Aligned Potential Drops

For the perfect magnetosphere-ionosphere coupling, in which there is no voltage drop along the field lines, the distribution of the electric field perpendicular to the magnetic field in the ionosphere must be an image of the magnetospheric field distribution and vice versa. The presence of the field-aligned potential drops affects the magnetosphere and ionosphere coupling in at least three aspects: (1) in mapping electric fields from the ionosphere to the magnetosphere, (2) in estimating the global distributions of Σ_p and Σ_h , and (3) in calculating magnetospheric pressure distributions. In a qualitative way, the third point may be seen by reflection on the dependence of $J_{||}$ on $\Phi_{||}$, as shown in (4.1).

To understand the field-aligned potential drop effects, we assume a constant conductivity without any enhancement so that Equations (4.1)-(4.4) are simplified considerably. The field-aligned current and potential in the ionosphere can be related directly to the magnetospheric potential in the local upward field-aligned current region by combining the governing equations (4.1)-(4.3). This provides

$$(1 - \lambda_c^2 \nabla^2) \Phi_i = \Phi_m \quad (4.5)$$

$$\alpha(1 - \lambda_c^2 \nabla^2) J_{||} = \lambda_c^2 \nabla^2 \Phi_m \quad (4.6)$$

where $\lambda_c = \sqrt{\alpha \Sigma_p}$ is the characteristic length for the magnetosphere-ionosphere coupling introduced by Chiu and Cornwall [1980] and Lyons [1980], and the field-aligned current is

related to the field-aligned potential drop by $\Phi_{\parallel} = \alpha J_{\parallel}$. The characteristic length λ_c is estimated to range from 50 km to 500 km for typical Σ_p and α values. As an example, taking $\Sigma_p = 5$ mhos and $\alpha = 2$ kV/(\mu A/m²), the characteristic length $\lambda_c = \sqrt{\alpha \Sigma_p} = 200$ km, which is comparable with the typical latitudinal width of inverted-V precipitation regions. Equation (4.5) is a typical diffusion equation with the diffusion length equal to λ_c and the magnetospheric potential Φ_m acting as an external source. On this basis, Lyons [1980] and Chiu and Cornwall [1980] pointed out that small scale ($\lambda_c/\lambda \gg 1$, λ : scale length associated with the field gradient) magnetospheric structure is filtered out of the ionospheric field while large scale ($\lambda_c/\lambda \ll 1$) electric fields are fully impressed on the ionosphere. Alternatively, Equation (4.6) shows that the largest potential drops and upward field aligned currents are generated at the smallest scale lengths. When the (mapped) scale length λ of the magnetospheric field is much less than λ_c , the first term on the left side of equation (4.6) can be neglected, so that $J_{\parallel} \approx \Phi_m/\alpha$ and the magnitude of the field-aligned potential drop is nearly equal to the magnitude of the magnetospheric potential Φ_m . In contrast, the field-aligned potential and its associated field-aligned current go to zero for the imposed magnetospheric field of an extremely large scale. The implication is that large scale magnetospheric structure is manifested in the ionosphere in the ionospheric electric field, whereas small scale magnetospheric structure is manifested in the electron precipitation pattern, at least in regions of upward field aligned current. These predictions have been confirmed by the DE observations [Weimer, *et al.*, 1985; 1987]. It should be noted that small-scale auroral structure such as that associated with discrete auroral arcs (10's km in latitudinal width) cannot be explained as a natural consequence of the simple current-voltage relation (4.1) without imposing structure in the magnetospheric electric field distribution.

The connection between the potential drop and the local upward field-aligned current intensity leads to the significant prediction that the auroral field-aligned potential structure has

a unique perpendicular scale length of about 100 km, intermediate between auroral arc scales (10's km) and global magnetosphere-ionosphere coupling scales (more than 100's km in latitudinal width). On the scales discussed, the role of field-aligned potential drops is not expected to be significant for the global convection pattern except for some intermediate-scale "boundary regions" such as the convection reversals and Harang discontinuity whose scale lengths are comparable to λ_c . However, the upward field-aligned current density may be significantly reduced due to an additional loading of field-aligned potentials. The conductivity enhancement due to the electron precipitation will modify the field-aligned potential structure by increasing the perpendicular scale length $\lambda_c = \sqrt{\alpha \Sigma_p}$ so that the intermediate-scale magnetospheric structure can be smoothed out and the field-aligned current density can be further decreased. The existence of the nonuniform Hall conductance will certainly lead to a deformation of the convection and current distribution patterns as consequences of a blockage of the Hall current from closure in the magnetosphere via field-aligned currents [Kan and Kamide, 1985]. As a result, the plasma flows in such a way to avoid the high conductivity regions.

4.3 Global Effect of Field-Aligned Potential Drops

The global convection pattern is believed to be governed not only by the external conditions in the solar wind, but also by the internal conditions in the magnetosphere and the ionosphere. The external condition that is known to have a strong influence on the convection pattern is the interplanetary magnetic field (IMF) as demonstrated by Heppner [1977], Heelis [1984] and more recently by Heppner and Maynard [1987]. The internal conditions that can modify the convection pattern include the ionospheric conductance and the field-aligned potential drop along magnetic field lines. In section 4.1, the governing equations of the M-I coupling model including the field-aligned potential drop effect has been proposed. These

equations, with an assumed external driving force, can be solved numerically to determine the convection pattern, field-aligned current and the ionospheric conductivity distribution.

The external driving "force" of the M-I coupling can be either a constant current generator, a constant voltage generator or a combination of the two. Indeed, Kan and Sun [1985] showed that the driving force of the M-I coupling is a combination of a constant voltage generator on open field lines in the polar cap and a constant current generator on closed field lines in the plasma sheet. A constant-voltage source by definition is an infinite energy source of zero internal resistance. Under such conditions the potential across the source region can be shown to stay constant, regardless of how the load changes with time. From the wave propagation standpoint, the voltage across the source region stays constant if the incident and reflected wave electric fields cancel each other at the source region, as indicated in Chapter 3 by the results of the Alfvén wave reflection at the open magnetopause. In comparison with a voltage source, a constant-current source with an infinite internal resistance delivers a constant current regardless of how the load changes with time. It will be shown in appendix C that the near-Earth plasma sheet may be viewed as a constant current source where the field-aligned currents of the incident and reflected Alfvén waves cancel each other. In the context of the present steady-state model, we will assume the driving force to be either a constant voltage generator or a constant current generator on all field lines, for simplicity. Thus, a constant voltage generator assumes that the entire magnetospheric potential is given externally and held constant in time, while a constant current generator assumes that the field-aligned current density is completely predetermined and held constant in time externally by the solar wind. The effect of field-aligned potential drops on the M-I coupling under these two types of generators will be examined individually as given below by the numerical results.

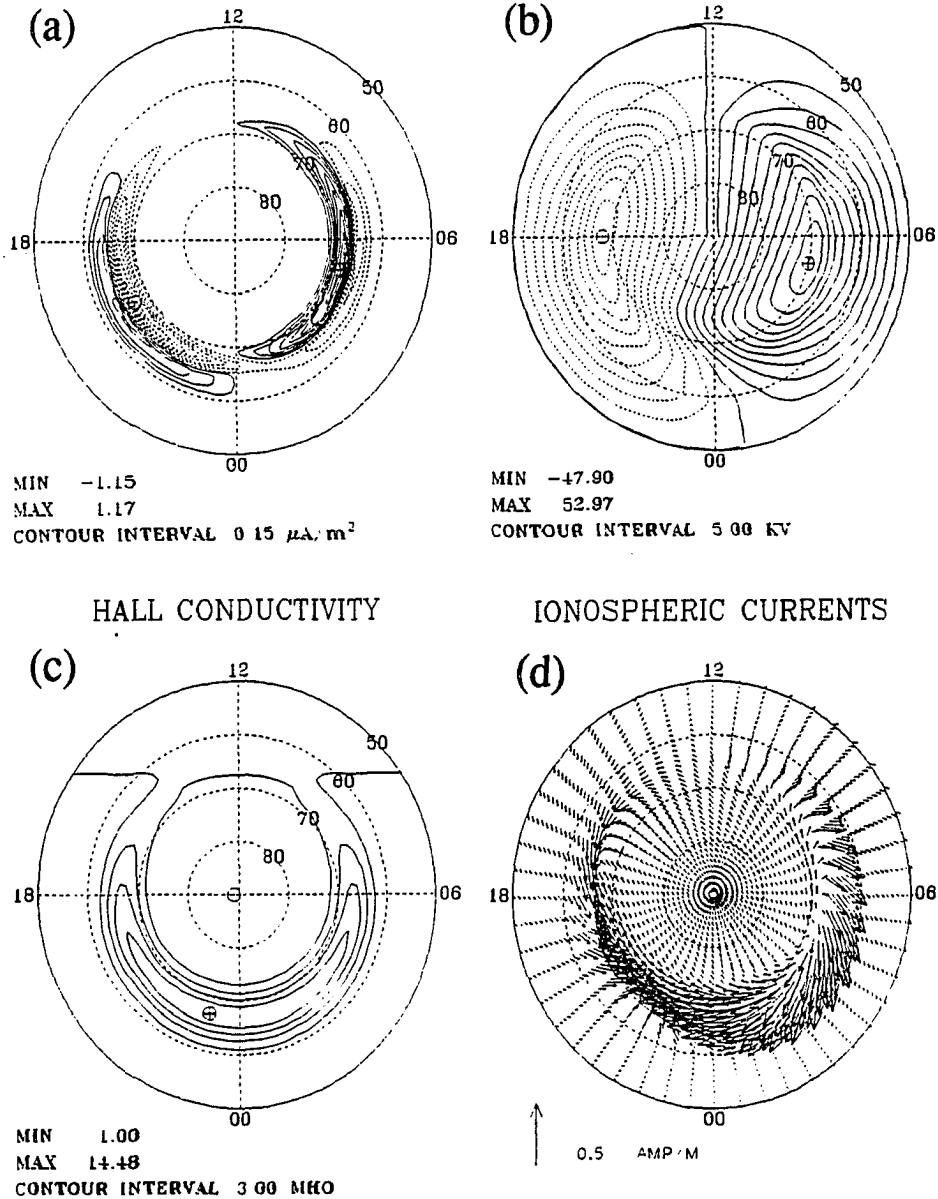


Figure 4.1 Results of M-I coupling without the field-aligned potential drop. (a) Contours of constant field-aligned current density given externally by the generator. Upward current is denoted by the dashed curves; downward current is shown by the solid curves. (b) Equal-potential contours of the resulting potential in the magnetosphere and the ionosphere. The solid and dashed contour lines are for positive and negative potential value, respectively. The polar cap potential is given by the difference between the maximum and minimum potential indicated on the lower left-hand corner. (c) Contours of the background Hall conductivity, consisting of the solar conductance and the diffuse auroral conductance. (d) Ionospheric current vectors. These results are useful in bringing out the effects of the field-aligned potential drop.

Constant Current Source Without $\Phi_{||}$

Figure 4.1 shows the results of M-I coupling without field-aligned potential drops (by choosing $\alpha = 0$). Numerical solutions of the model are obtained in the plane polar coordinate system (r, θ) , divided into grids of size 1° in latitude (*i.e.*, the radial dimension) and 7.5° in longitude (*i.e.*, the azimuthal dimension). The boundary condition chosen for the model is $\Phi = 0$ at the 50° latitude. Figure 4.1a shows the assumed field-aligned current produced externally by a constant current generator. Figure 4.1c shows the distribution of the background ionospheric conductance that consists of the solar conductance and the diffuse auroral conductance. The magnetospheric potential, projected along field lines onto the polar ionosphere, is obtained by solving (4.3) and is shown in Figure 4.1b. Without the field-aligned potential drop, the ionospheric potential is identical to its magnetospheric counterpart. The ionospheric current vectors are shown in Figure 4.1d. These results of M-I coupling under $\Phi_{||} = 0$ will be used as a reference point in comparison with the M-I coupling results under $\Phi_{||} \neq 0$.

The distribution of the large-scale region I and II field-aligned currents, displayed in Figure 4.1a with a maximum current density around $1 \mu\text{A}/\text{m}^2$, is consistent with the pattern described extensively by Iijima and Potemra [1976] based on the observational data. The rotated field-aligned current distribution in Figure 4.1a is chosen to produce the potential pattern in Figure 4.1b, which is consistent with the pattern given by Heppner and Maynard [1987]. Since the convection pattern on the dayside is known to depend on the IMF B_y direction, the rotation of the field-aligned distribution can be expected to depend on the sign of IMF B_y component. Such rotation will be averaged out in statistical data analysis as in Iijima and Potemra [1976]. The diffuse auroral conductance belt in Figure 4.1c is similar to the Hall conductivity belt deduced statistically by Hardy *et al.* [1987] based on electron precipitation data under high K_p conditions, and has been shown by Cheng *et al.* [1987] to be a reasonable representation of the diffuse auroral luminosity and to give rise to a reasonable current distribution in the M-I

coupling model. It should be emphasized that the field-aligned distribution, the polar-cap size, and the distribution of diffuse auroral conductance are interrelated to each other in the real magnetosphere-ionosphere system. The parameters in Figure 4.1 were chosen to approximate such relations, and this particular choice we made is what we consider to be a representative one. The field-aligned current distribution and the magnetospheric potential patterns in Figure 4.1 will be used as the input patterns for the constant-current generator and the constant-voltage generator, respectively.

Constant Current Source With $\Phi_{||}$ Effect

The constant current generator is modeled by a given field-aligned current distribution maintained constant externally. The background ionospheric conductance (*i.e.*, the solar conductance and the diffuse aurora conductance) is also assumed given externally. The field-aligned potential $\Phi_{||}$ in this case is completely predetermined since the field-aligned current is given externally. The potentials Φ_m , Φ_i and the enhanced ionospheric conductance will be determined from the governing equations (4.1) to (4.4).

Figure 4.2 shows the M-I coupling results of a constant current generator with a field-aligned potential drop (by choosing $\alpha = 5\text{kV}/\mu\text{A}$). For a given value of α , the field-aligned potential is specified by the constant current generator due to the $J_{||}$ and $\Phi_{||}$ relationship in (4.1). Figure 4.2a shows the field-aligned current density of a constant current generator assumed to be identical to that of Figure 4.1. The background ionospheric conductance is also assumed to be the same as in Figure 4.1c. The magnetospheric potential projected onto the ionosphere is shown in Figure 4.2b, while the ionospheric potential is shown in Figure 4.2d. The difference between the magnetospheric and ionospheric potentials reflects the presence of the field-aligned potential drop whose distribution is the same as that of the upward field-aligned currents shown by the dashed lines in Figure 4.2a. The maximum field-aligned potential drop

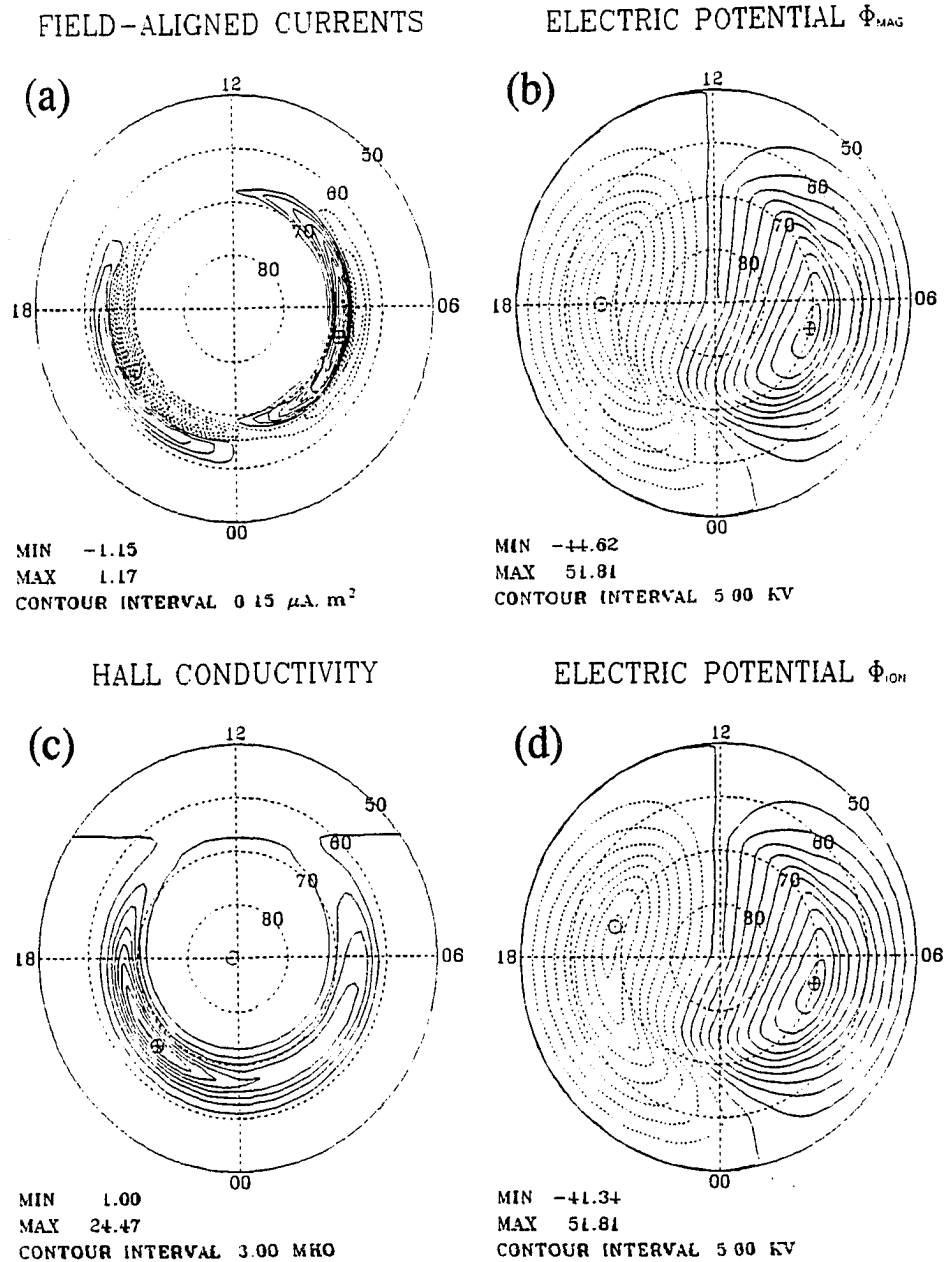


Figure 4.2 Results of M-I coupling powered by a constant current generator for $\Phi_{||} \neq 0$. α is set to $5 \text{ kV}/(\mu\text{A}/\text{m}^2)$. (a) The input field-aligned current density that is identical to that of Figure 4.1a. The field-aligned potential drop, which has not been shown here, is proportional to the upward field-aligned current density and has a same distribution as the dashed pattern in (a). (b) The resulting magnetospheric potential Φ_m that has been projected along field lines onto the ionosphere. (c) The enhanced ionospheric Hall conductance. (d) The ionospheric potential Φ_i .

is 5.25 kV associated with the maximum upward current in the evening sector. There is a 1.5 kV field-aligned potential drop associated with the upward current in the dawn sector. The ionospheric conductance shown in Figure 4.2c is enhanced above the background level due to the field-aligned potential and the upward field-aligned current.

Since the field-aligned potential drop is usually much smaller than the polar cap potential, the potential values in both the magnetosphere and the ionosphere are not expected to be changed significantly. Comparing Figures 4.1 and 4.2, it can be seen that the polar cap potential, which is the difference of the maximum and minimum potential values, is reduced from ~ 100 kV in Figure 4.1b to ~ 96 kV in Figure 4.2b due to additional loading by the field-aligned potential including the resulting enhancement of the ionospheric conductance. The polar cap potential in the ionosphere is ~ 93 kV in Figure 4.2d. The difference between the magnetospheric and ionospheric polar cap potentials is 3.28 kV, which is less than the maximum field-aligned potential drop of 5.25 kV. This is understandable because the field-aligned potential drop depends on the potential on a given flux tube, while the polar cap potential drop depends on potentials across different flux tubes. Although the maximum field-aligned potential drop is only about 5% of the polar cap potential, the convection pattern is noticeably distorted in the region where the field-aligned potential drop occurs. From Figures 4.2b and 4.2d, it is seen that the field-aligned potential drop broadens the ionospheric convection reversal relative to its magnetospheric counterpart in the evening sector. It can be also noticed that the ionospheric convection reversal boundary in the evening sector shifts toward the afternoon sector and equatorward as well. The feature of the convection reversal broadening due to the effect of field-aligned potential drops is consistent with the discussion in the previous section about the local effect of field-aligned potential drops, while the shifting of

the convection reversal is a global phenomenon due to the loading effect of the field-aligned potential and the enhancement of the ionospheric conductivity.

Figure 4.3 is the same as Figure 4.2, except that a large α ($=10 \text{ kV}\cdot\text{m}^2/\mu\text{A}$) value is chosen. Figure 4.3a shows the field-aligned current density of a constant current generator assumed to be identical to that of Figures 4.1a and 4.2a. With an increase in α , the field-aligned potential drop is increased, resulting in further enhancement of the ionospheric conductivity and further distortion of the convection pattern. The field-aligned potential drop has a distribution the same as that of the upward field-aligned current shown by the dashed lines in Figure 4.3a. The maximum field-aligned potential drop is 10.50 kV, which is associated with the maximum upward current in the evening sector. Comparing Figures 4.2b and 4.3b, it can be seen that the convection reversal in the magnetosphere becomes somewhat sharper with the increase in α although the polar cap potential in the magnetosphere doesn't change much. The maximum Hall conductivity increases from 24.47 mho in Figure 4.2c to 31.89 mho in Figure 4.3c due to the increase in Φ_{\parallel} . The ionospheric potential in Figure 4.3d has a more smooth convection reversal than that in Figure 4.2d, and the polar potential is further reduced from $\sim 93 \text{ kV}$ in Figure 4.2d to $\sim 88 \text{ kV}$ in Figure 4.3d. It can be also noticed that the convection reversal in the magnetosphere shifts toward the evening sector, while the convection reversal in the ionosphere moves further toward the afternoon sector.

When the field-aligned potential drop is included in the M-I coupling powered by a constant current generator, the polar cap potentials in both the magnetosphere and the ionosphere are reduced and the convection patterns are distorted from the $\Phi_{\parallel} = 0$ case. The ionospheric potential on the dusk side in Figures 4.2d and 4.3d is less negative than its magnetospheric counterpart in Figures 4.2b and 4.3b, which is necessary for supporting the resulting field-aligned potential drop. The electron precipitation associated with the upward field-aligned current results in the enhancement of ionospheric conductances as shown in Figures 4.2c and

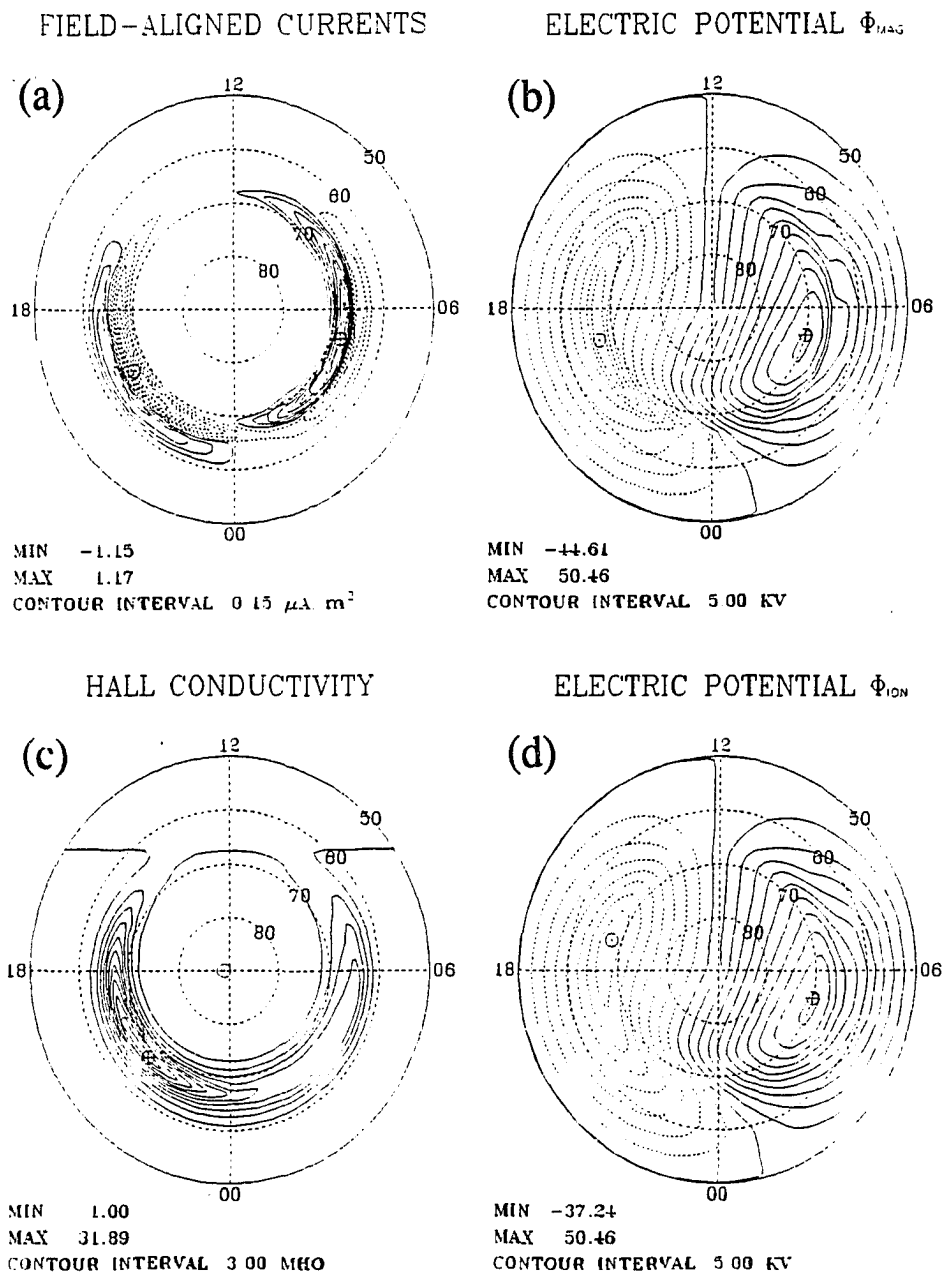


Figure 4.3 Same as Fig. 4.2, but for $\alpha = 10 \text{ kV}/(\mu A/m^2)$.

4.3c. With the conductivity increase, the convection electric field in the ionosphere has to be reduced to maintain the constant field-aligned current. A significant decrease of convection fields near the convection reversal is indicated in Figures 4.2d and 4.3d by smoothing and shifting of the convection reversal in the evening sector. The reduction of the magnetospheric convection potential is due to the additional loading by the field-aligned potential and the distortion of the magnetospheric convection potential is produced to maintain the field-aligned current density given externally by the current generator.

Constant Voltage Source With ϕ_{\parallel} Effect

The constant voltage generator is specified in the M-I coupling model by assuming that the magnetospheric convection potential Φ_m is given and fixed externally. The background ionospheric conductance is also assumed given externally.

Figure 4.4 shows the results of M-I coupling powered by a constant voltage generator with a field-aligned potential drop (by choosing $\alpha = 5 \text{ kV}/\mu\text{A}$). Figure 4.4a shows the generator that is chosen to be identical to the magnetospheric potential in Figure 4.1b. Figure 4.4b shows the field-aligned current, which is substantially reduced from the $\Phi_{\parallel} = 0$ case in Figure 4.1a. The reduction in the field-aligned current is due to the additional loading by the field-aligned potential and the enhancement of the ionospheric conductance. The distribution of field-aligned potential drops is the same as that of the upward field-aligned currents shown by the dashed lines in Figure 4.4b and the maximum field-aligned potential drop is 2.25 kV in the evening sector. Figure 4.4c shows the ionospheric potential, which is only slightly reduced from its magnetospheric counterpart. Figure 4.4d shows the enhanced ionospheric conductance starting from the background conductance in Figure 4.1c.

Figure 4.5 is the same as Figure 4.4, except that a larger $\alpha (=10 \text{ kV}\cdot\text{m}^2/\mu\text{A})$ value is chosen. When the parameter α is viewed as a resistivity along the magnetic field lines, it is

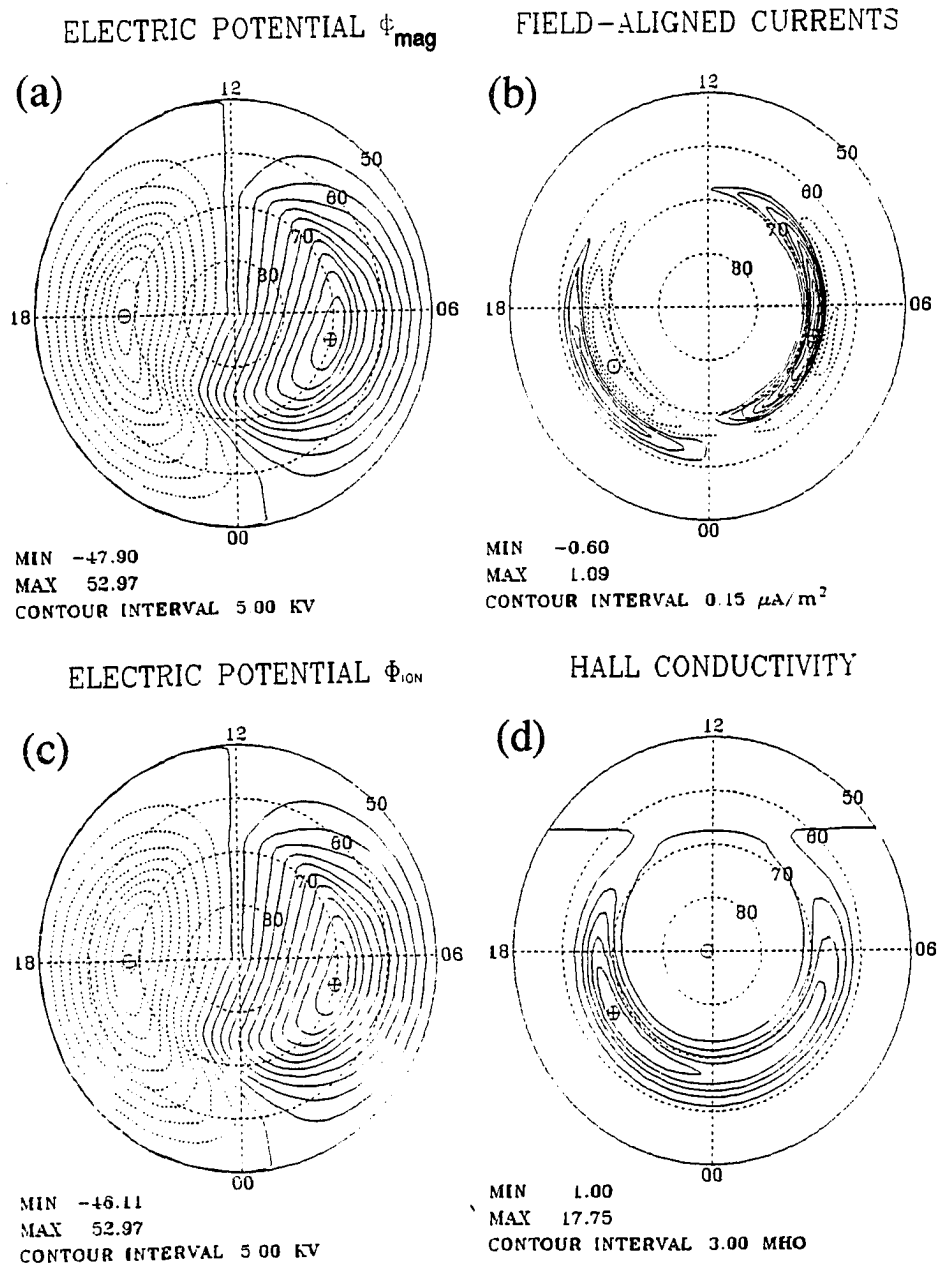


Figure 4.4 Results of M-I coupling powered by a constant voltage generator for $\Phi_{\parallel} \neq 0$. α is set to $5 \text{ kV}/(\mu\text{A}/\text{m}^2)$. (a) The input magnetospheric potential that is identical to that of Figure 4.1b. (b) The resulting field-aligned current density. (c) The ionospheric potential. (d) The enhanced ionospheric Hall conductance.

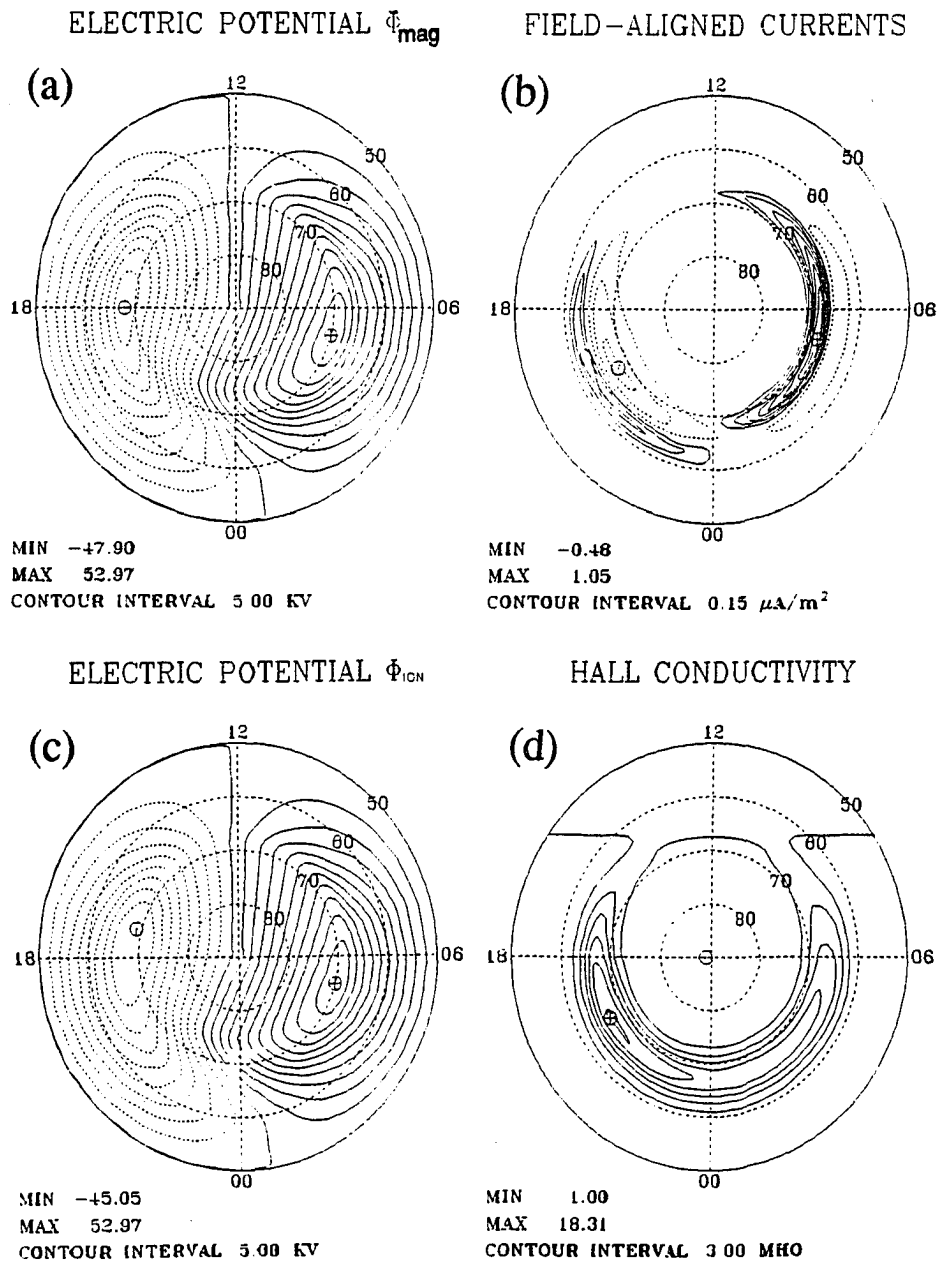


Figure 4.5 Same as Fig. 4.4, but for $\alpha = 10 \text{ kV}/(\mu\text{A}/\text{m}^2)$.

understandable that the additional loading by increasing α can reduce the field aligned current and the potential in the ionosphere. The maximum upward field-aligned current density is reduced from $0.6 \mu\text{A}/\text{m}^2$ in Figure 4.4b to $0.48 \mu\text{A}/\text{m}^2$ in Figure 4.5b. The negative potential in the ionosphere is only slightly reduced. The difference between the magnetospheric and ionospheric polar cap potentials in Figure 4.5 is 2.85 kV, which is comparable to the maximum field-aligned potential drop 3.8 kV in the evening sector. The convection reversal broadens and shifts toward the afternoon sector in the same way as in the constant current generator case, although the distortion of potential patterns is less significant in the constant voltage generator case.

It is noticed that the field-aligned current and the field-aligned potential drop in the constant voltage generator cases (Figures 4.4 and 4.5) are substantially lower than those of the constant current generator case (Figures 4.2 and 4.3), even though the polar cap potential in the constant voltage generator case is somewhat greater than that of the constant current generator case. This result can be understood by comparing the magnetospheric convection patterns in the two cases. The magnetospheric convection reversal in the evening sector of the constant current generator case is somewhat sharper than that of the constant voltage generator case. The sharpness of a convection reversal is a direct measure of the vorticity of the convection, which is an important factor for the magnetospheric closure of the region I field-aligned current (see, for example, Kan [1987]). It is found that a constant current generator allows the vorticity of the magnetospheric convection to adjust so that the field-aligned current can be kept constant under the loading influence of the field-aligned potential including the resulting enhancement of the ionospheric conductance. On the other hand, a constant voltage generator cannot adjust the vorticity of the magnetospheric convection to maintain the field-aligned current. Thus, the field-aligned current in the constant voltage generator case is reduced under the loading influence of the field-aligned potential.

4.4 Discussion and Summary

We have shown the effects of field-aligned potential drops on the global magnetosphere-ionosphere coupling powered either by a constant current generator or by a constant voltage generator. It is found that a potential drop of a few kV along the magnetic field lines can significantly distort the convection pattern near the convection reversal in the evening sector although the polar cap potential in the ionosphere is only slightly reduced from that in the magnetosphere. The field-aligned potential drop has the effect of broadening the ionospheric convection reversal region relative to its magnetospheric counterpart in the evening sector and shifting the reversal toward the afternoon sector. It is also shown that a constant current generator can support a larger field-aligned potential drop than a constant voltage generator under comparable or even somewhat greater polar cap potential drop. The magnetospheric convection pattern is distorted more in the constant current generator case than in the constant voltage generator case. The reason for the characteristic difference between the constant current generator and the constant voltage generator lies in the generator's ability to adjust the vorticity of the convection. A constant current generator allows the vorticity of the magnetospheric convection to adjust so that the field-aligned current can be kept constant under the loading influence of the field-aligned potential (including the enhancement of the ionospheric conductance). A constant voltage generator by definition cannot adjust the vorticity of the magnetospheric convection so that the field-aligned current is reduced under the loading influence of the field-aligned potential.

In the real magnetosphere, the source is likely to be a hybrid of the constant current and constant voltage generators, rather than one or the other. The source on open field lines at the magnetopause is shown in chapter 3 to be approximately a constant voltage generator. The source on closed field lines at the near-Earth plasma sheet may be viewed as a current generator,

as will be shown in appendix C. A continuous transition, from a constant voltage generator on open field lines to a constant current generator at the near Earth plasma sheet, can lead to a reasonable convection pattern as shown by Kan and Sun [1985]. Combining their results with the results in this study, we suggest that field-aligned potential drops are most likely to occur on close field lines than on open field lines. This is consistent with the widely accepted belief that the discrete auroral arcs occur mostly on closed field lines.

When the field-aligned potential drop is included in the steady state M-I coupling, the magnetosphere-ionosphere system behaves like a current circuit with the field-aligned current closure through the ionospheric currents and with two resistive-like elements— the ionospheric conductance and the loading of the potential drop along the field lines. The potential structure is characterized by a typical transverse spatial scale $\lambda_c = \sqrt{\alpha \Sigma_p} \sim 100 \text{ km}$. In the time dependent magnetosphere-ionosphere coupling, the time-dependent field-aligned current propagates toward the ionosphere by the Alfvén waves. As an alternative to the static situation with ionospheric current closure, one can consider a continuation of field-aligned current by transverse polarization currents to which one can attach the Alfvén wave conductivity Σ_A (see equation 2.4 in Chapter 2). This defines a much smaller scale $\lambda_A = \sqrt{\alpha \Sigma_A}$ of the order of 10 km above the polar ionosphere since the Alfvén wave conductivity Σ_A is usually much smaller than the ionospheric Pedersen conductivity Σ_p . The characteristic length λ_A is comparable to the arc's scale. Therefore, one may expect that the auroral arc structure can be significantly modified by the Alfvén waves when it is coupled with the field-aligned potential. A further study on the interaction between Alfvén waves and field-aligned potentials remains to be done to improve our understanding of the time dependent magnetosphere-ionosphere coupling.

CHAPTER 5

A 3-D Tearing Model for the Dayside Reconnection

In the previous chapters I discussed internal characteristics of the magnetosphere and ionosphere coupling system. It was argued that an enhancement of magnetospheric convection can lead to the generation of Alfvén waves that are bouncing between the magnetopause and the ionosphere. The enhanced magnetospheric convection is mainly due to the reconnection process in which energy can be transferred from the solar wind to the magnetosphere. Magnetic field reconnection can occur in magnetized plasma where the magnetic field exhibits a reversal. The existing reconnection models and observation evidence have been reviewed recently by Heikkila [1990]. In this chapter I will discuss an oblique tearing instability, which is believed to be important in initiating the dayside magnetic reconnection.

In the first section I will give a brief review on the tearing instability and discuss the importance of this study as a first step toward understanding the patchy and intermittent reconnection at the dayside magnetopause. In the second section, the basic equations and the numerical results for the oblique resistive tearing will be presented. In the third section, implications of our results for the patchy and intermittent reconnection of a finite-size current sheet at the dayside magnetopause will be discussed.

5.1 Introduction

In the absence of nonideal magnetohydrodynamic effects such as resistivity or inertia, the current sheet in a magnetic reversal layer, as shown in Figure (5.1a), is stable since all perturbations in which the plasma remains frozen to the magnetic field lines result in an increase

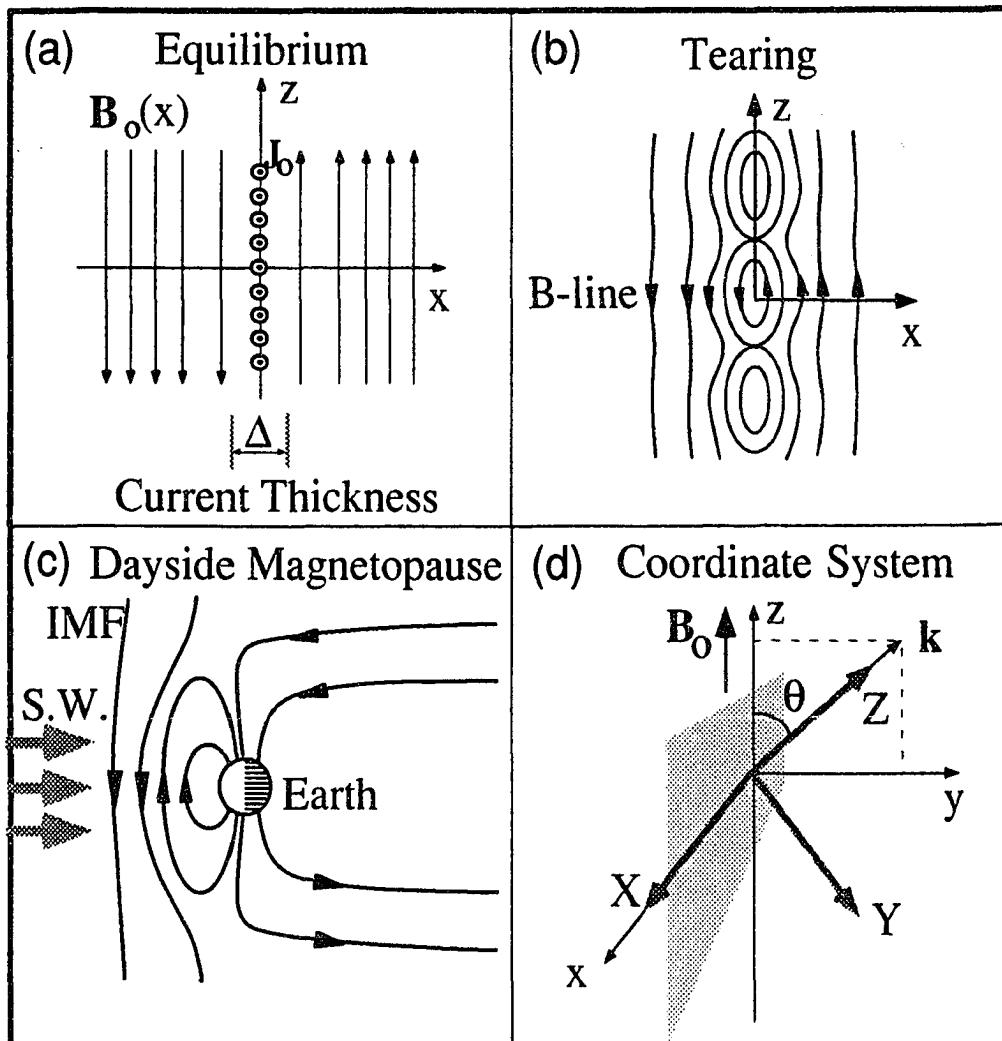


Figure 5.1 Geometrical configuration of a magnetic reversal layer and the coordinate system. Panel (a) displays a thin current sheet J_0 in the magnetic reversal layer. Δ denotes the current thickness. Panel (b) shows the magnetic field configuration in a tearing mode. Panel (c) is a schematic draw of dayside magnetopause. Panel (d) shows the two coordinate systems (x, y, z) and (X, Y, Z) . In the coordinate system (x, y, z) , x is the coordinate normal to the magnetic gradient and z axis is parallel to the reversal magnetic field. The wave vector of oblique tearing is denoted by the vector k with an angle θ measured from the z axis. In the coordinate system (X, Y, Z) , which is formed by rotating the (x, y, z) system around x -axis for an angle of θ , Z axis is parallel to the wave vector k and Y axis is normal to the X - Z plane.

in the magnetic energy of the system. Finite resistivity or inertia, however, allows the tearing instability to relax the system to a lower magnetic energy state. In particular, the tearing mode results in the current filaments at X lines, and the B field lines tear and reconnect near the central layer self-consistently forming the characteristic magnetic islands shown in Figure (5.1b). The tearing instability can be expected to develop at the dayside magnetopause where there exists a current sheet with a magnetic reversal layer when the magnetic field lines in the solar-wind turn southward, as shown in Figure (5.1c).

The tearing mode instability is commonly considered to be closely related to the magnetic field reconnection in a plasma. Since the first investigation by Furth, Killeen, and Rosenbluth [1963], the resistive tearing instability has attracted considerable attention [Killeen and Sheshtakov, 1978; Terasawa, 1983; Quest and Coroniti, 1985; Lee and Fu 1986].

The tearing instability investigated by Furth *et al.* [1963] is based on the MHD approximation that the current sheet thickness is much larger than the scale length of the plasma such as inertial length and gyroradius. When the thickness of the magnetic reversal layer becomes as thin as the ion inertial length, a non-MHD effect, *i.e.*, the finite-ion-inertial-length (FIIL) effect, is expected to be important in determining the growth rate [Vasyliunas, 1975; Sonnerup, 1979]. Since the magnetic reversal layer at the dayside magnetopause can be as thin as the ion inertial length when the reconnection process is supposed to occur [Sonnerup *et al.*, 1981; Berchem and Russell, 1982], the FIIL effect should have an observable consequence. Figure (5.1d) shows a geometry of oblique tearing with a two-dimensional wave vector $\mathbf{k} = k_z \hat{e}_z + k_y \hat{e}_y = k(\cos \theta \hat{e}_z + \sin \theta \hat{e}_y)$, where θ is the angle between the wave vector \mathbf{k} and the z axis parallel to the equilibrium magnetic field \mathbf{B}_0 . Assuming a parallel propagation ($\theta = 0$), Terasawa [1983] and Hassam [1984] found that the FIIL effect leads to the enhancement of the tearing instability and results in a vortex electric current in the tearing

plane (*i.e.*, in the k - x plane). Associated with the vortex electric current, the field B_y perpendicular to the tearing plane is generated. On the other hand, an oblique tearing ($\theta \neq 0$) mode in the MHD limit also leads to the vortex electric current in the tearing plane, but its growth rate is less than that in a parallel tearing ($\theta = 0$) [Furth et al, 1963]. The B_y component and the twisting of magnetic field lines in the flux transfer events (FTEs) have been observed at the dayside magnetopause [Russell and Elphic, 1978; 1979; Saunders *et al.*, 1984; Berchem and Russell, 1984; Rijnbeek *et al.*, 1984; Farrugia *et al.*, 1987]. The appearance of B_y can be interpreted in terms of the three-dimensional MHD reconnection. However, as proposed by Terasawa [1983], the FILL effect of a thin current sheet may provide an alternative mechanism to explain the appearance of B_y component. Therefore, it is interesting to see what is the FILL effect on the oblique tearing mode and its associated B_y component.

As pointed out by Quest and Coroniti [1981, 1985], the finite extent of the dayside magnetopause precludes the existence of a tearing mode with only one-dimensional wave vector. The finite current sheet at the dayside magnetopause assures that the spatial extent of the tearing mode will be bounded in the y direction (dawn-dusk), so that the tearing mode will grow only as a localized wave packet. Only the tearing mode wave packet composed of maximally growing wave numbers can survive for more than an e -folding period to produce an interconnection of the oppositely directed field lines. Thus, the tearing mode at the dayside magnetopause is a three-dimensional problem, involving a two-dimensional wave vector tangential to the magnetopause. Coupled with the drifting nature of tearing modes, tearing-reconnection will be spatially inhomogeneous and temporally unsteady. Such a 3-D tearing mode, which is the normal mode of tearing on a finite current sheet of the dayside magnetopause, has been proposed by Kan [1988] for the patchy and intermittent reconnection for the elbow-shaped FTEs [Russell and Elphic, 1979].

In this study, I shall investigate the obliquely propagating tearing mode in a thin magnetic reversal layer with thickness down to the ion inertial length. The vortex electric current due to the FIIL effect enhances the tearing instability, while the vortex electric current due to the oblique propagation reduces the growth rate. The primary motive of this study is to examine their relative importance and their combined effects. The growth rate will be calculated numerically for an oblique tearing mode $\exp[ik(z \cos \theta + y \sin \theta)]$ where θ is the propagation angle between the wave vector \mathbf{k} and the z axis parallel to the reversal magnetic fields. In the MHD limit, it is known that the maximally growing mode is centered about $\theta = 0$, and the growth rate decreases monotonically with increasing $|\theta|$. When the finite-ion-inertial-length (FIIL) effect is included, the tearing instability is either enhanced or suppressed depending on the propagation angle θ . It is found that only waves in several relatively narrow bands of the angle θ are unstable and that the unstable oblique tearing mode has a significant phase velocity. The 3-D magnetic field structure associated with the oblique tearing modes will be carefully examined. Finally, I will also discuss the relevance of 3-D tearing to the patchy and intermittent reconnection at the dayside magnetopause.

5.2 Oblique Resistive Tearing of a Thin Current Sheet

The present study of the resistive tearing instability is based on one-fluid equations that retain a Hall current term in the generalized Ohm's law.

5.2.1 Basic Equations

The fluid is assumed to be incompressible and isothermal. The basic equations are given as follows

$$\rho \frac{d\mathbf{V}}{dt} = -\nabla(P_i + P_e) + \frac{1}{c} \mathbf{J} \times \mathbf{B} \quad (5.1)$$

$$\nabla \cdot \mathbf{B} = 0, \quad \nabla \cdot \mathbf{V} = 0 \quad (5.2)$$

$$\frac{\partial \mathbf{B}}{\partial t} = -c \nabla \times \mathbf{E}, \quad \mathbf{J} = \frac{c}{4\pi} \nabla \times \mathbf{B} \quad (5.3)$$

$$\mathbf{E} + \frac{1}{c} \mathbf{V} \times \mathbf{B} = \eta \mathbf{J} - \frac{1}{ne} \nabla P_e + \frac{1}{nec} \mathbf{J} \times \mathbf{B} \quad (5.4)$$

With a quasineutrality approximation and neglecting the electron mass m_e , the above one-fluid equations are equivalent to the two-fluid equations, which are rigorous consequences of the Vlasov equation except the particle-wave interaction [Vasyliunas, 1975]. In the generalized Ohm's law (5.4), the simple resistivity term $\eta \mathbf{J}$ represents the effect of ion-electron collisions. The resistivity η and the number density n are taken to be constant, since I consider only the tearing instability whose growth rate is much faster than the resistive diffusion time [Furth *et al.*, 1963; Killeen and Shestakov, 1978; Lee and Fu, 1986]. The applicability of collisional one-fluid model to a highly collisionless magnetospheric plasma depends on the existence of anomalous resistivity caused by microinstabilities [e.g., Huba *et al.*, 1981; Winske *et al.*, 1990]. With the finite anomalous resistivity, a resistive evolution of tearing islands may occur even in the collisionless system.

The last term in the generalized Ohm's law (5.4) is known as the Hall current term. When the Hall current term is replaced by the momentum equation (5.1), one can see that the generalized Ohm's law (5.4) is nothing more than the ion equation of motion in a collisional plasma since the assumption of negligible electron mass ensures the equivalence of the total fluid flow \mathbf{V} and the ion flow.

$$\mathbf{E} + \frac{1}{c} \mathbf{V} \times \mathbf{B} = \eta \mathbf{J} + \frac{1}{ne} \nabla P_i + \frac{M_i}{e} \frac{d\mathbf{V}}{dt} \quad (5.4a)$$

Except for the additional resistive term, the above equation is the same as equation (2.11) in chapter 2. The tearing instability involves a breakdown of the frozen-in MHD approximation. It can be readily seen from Equation (5.4a) that the frozen-in condition can be modified due to effects other than resistivity, *i.e.*, due to the effects associated with last two terms. The last term in equation (5.4a) is due to a finite ion inertia and its associated non-MHD effect is referred to as the finite-ion-inertial-length (FIIL) effect, while the second to the last term is due to the finite ion temperature (FIT) effect. The Hall current term in the generalized Ohm's law (5.4) contains both the FIIL and FIT effects. These non-MHD effects are expected to play an important role in a thin current sheet whose thickness is of the order of the ion inertial length. In order to achieve analytical tractability and to focus on the FIIL effect on the tearing instability, the plasma is assumed to be incompressible and isothermal so that the finite-ion-temperature effect associated with the ion pressure term $\nabla(P_i/n)$ in equation (5.4a) is neglected.

It is known that the compressibility has no effect on the purely growing tearing mode in the MHD limit [Furth et al, 1963], even when the FIIL effect is included if $\theta = 0$ [Terasawa, 1983]. When the propagation angle θ is small, it is found that the tearing phase velocity, caused by the FIIL effect on oblique modes, is much smaller than the Alfvén speed, so that the incompressible approximation is reasonable. However, in an extremely thin current sheet whose thickness is smaller than the ion inertial length, the phase velocity of highly oblique mode will become comparable to the Alfvén speed and the compressibility may become important. Consider an equilibrium magnetic field given by

$$\mathbf{B}_0(x) = \hat{e}_z B_{z0} \tanh\left(\frac{x}{\Delta}\right) \quad (5.5a)$$

From the pressure balance, one obtains

$$P = P_0 \operatorname{sech}^2\left(\frac{x}{\Delta}\right) \quad (5.5b)$$

where P is the plasma pressure.

I then linearize the basic equations assuming perturbations of the form $f_1(x, t) \exp[i(k_x z + k_y y)]$. The analysis can be simplified by choosing a coordinate system (X, Y, Z) , which is formed by rotating the (x, y, z) system around the x -axis for an angle of θ as shown in Figure (5.1d). In this new coordinate system with Z axis parallel to the wave vector \mathbf{k} and Y axis normal to the X - Z plane, there is no variation along Y axis and all perturbation quantities vary only in the X - Z plane. With the incompressible and the constant resistivity η approximations, the linearized equations can be written in dimensionless form as

$$\frac{\partial}{\partial \tau} \psi_X = S^{-1} \nabla^2 \psi_X - F W_X - h \alpha^2 \left(F \psi_Y + i \frac{\tan \theta}{\alpha} F' \psi_X \right) \quad (5.6)$$

$$\frac{1}{\alpha^2} \frac{\partial}{\partial \tau} \nabla^2 W_X = F \nabla^2 \psi_X - F'' \psi_X \quad (5.7)$$

$$\frac{\partial}{\partial \tau} \psi_Y = S^{-1} \nabla^2 \psi_Y - F W_Y + i \frac{\tan \theta}{\alpha} F' W_X - h (F \nabla^2 \psi_X - F'' \psi_X) \quad (5.8)$$

$$\frac{1}{\alpha^2} \frac{\partial}{\partial \tau} W_Y = F \psi_Y + i \frac{\tan \theta}{\alpha} F' \psi_X \quad (5.9)$$

where the Laplace operator $\nabla^2 = \partial^2 / \partial x^2 - k^2$ and the prime denotes the derivative of the x coordinate. Following Furth *et al.* [1963], I define the normalized perturbed quantities in equations (5.6)-(5.9) as

$$\begin{aligned}
\psi_X &= B_{X1}/B_{z0}, & W_X &= -iV_{X1}k\tau_A, \\
\psi_Y &= B_{Y1}/B_{z0}, & W_Y &= -iV_{Y1}k\tau_A, \\
F &= \mathbf{k} \cdot \mathbf{B}_0(\mathbf{x})/kB_{z0}, & k &= \sqrt{k_x^2 + k_y^2}, \\
\alpha &= k\Delta, & \tau_R &= 4\pi\Delta^2/(c^2\eta), & \tau_A &= \Delta\sqrt{4\pi\rho_0}/B_{z0}, \\
S &= \tau_R/\tau_A, & h &= c\sqrt{m_i/(4\pi n_0 e^2)}/\Delta
\end{aligned}$$

where the subscript 0 denotes the unperturbed equilibrium quantities and the subscript 1 denotes the first order perturbations. τ_R is a characteristic diffusion time and τ_A is an Alfvén transit time. The distance x is normalized to the current sheet thickness Δ and the time t to the Alfvén transit time τ_A ($\tau = t/\tau_A$). S , known as the Lundquist number or the magnetic Reynolds number, measures the relative importance of diffusion and convection. The Hall coefficient h is equal to the ion inertial length [$l_i = c/\omega_i = c\sqrt{m_i/(4\pi n_0 e^2)}$] normalized by the current sheet thickness Δ . The Hall coefficient h measures the relative importance of Hall current term in the generalized Ohm's law (5.4) and determines the FIIL effect on the tearing instability. In Equations (5.6)-(5.9), the combination of the variables (ψ_X, W_X) represents a tearing (slow) mode perturbation, and (ψ_Y, W_Y) an Alfvén mode perturbation. The FIIL effect introduced by a nonzero Hall coefficient h leads to coupling between these two modes. When the resistive term is neglected, the dispersion of the Alfvén mode including the FIIL effect can be obtained by solving the linear equations (5.6)-(5.9) in the region $|x| > \Delta$

$$\left(\frac{\omega^2}{k^2 V_a^2} - \cos^2 \theta \right)^2 = \frac{\omega^2}{\Omega_i^2} \cos^2 \theta = \frac{\omega^2}{k^2 V_a^2} k^2 l_i^2 \cos^2 \theta$$

where l_i is the ion inertial length and Ω_i is the ion gyrofrequency. In the incompressible limit ($\beta_\infty \rightarrow \infty$), the above dispersion is the same as the general dispersion relation (2.12) derived

in chapter 2 [Stringer, 1963; Cao and Kan, 1987]. In the MHD limit ($h \rightarrow 0$), these two modes are decoupled, and equations (5.6) and (5.7) are reduced to the usual Furth-Killeen-Rosenbluth (FKR) equations [Furth *et al.*, 1963]. When $k_y = 0$ ($\theta = 0$), one recovers the equations given by Terasawa [1983].

5.2.2 Numerical Results

I numerically integrate Equations (5.6)-(5.9) by the Crank-Nicholson scheme as described by Killeen and Shestakov [1978] in solving an initial value problem. At the start of each run, I specify S , h , $\alpha_z (= k_z \Delta)$, $\tan \theta (= k_y/k_z)$, and give an initial perturbation in W_X . For an unstable current sheet, the fastest growing mode in the plane wave assumption $\exp(\nu t - i\omega t)$, will dominate the numerical solution as time progresses. A complex frequency with growth rate ν and real frequency ω can be obtained from

$$\nu - i\omega = \partial_t \ln A$$

where A is for ψ or W . This complex frequency is calculated numerically at each grid point for ψ and W in a region $|x/\Delta| \leq 10$. Whenever the growth rate and real frequency converge for all variables over the entire domain to four figures, the calculation is terminated. The numerical schemes, for solving the equations (5.6)-(5.9) as an initial value problem, are given in appendix B.

The numerical results will be shown in graphic form in which effects of the Lundquist number S , the Hall coefficient h and the propagation angle θ on growth rates are presented. Unless specifically noted, all the results are obtained using $\alpha_z = k_z \Delta = 0.3$, near which the parallel tearing mode ($k_y = 0$) has a maximum growth rate.

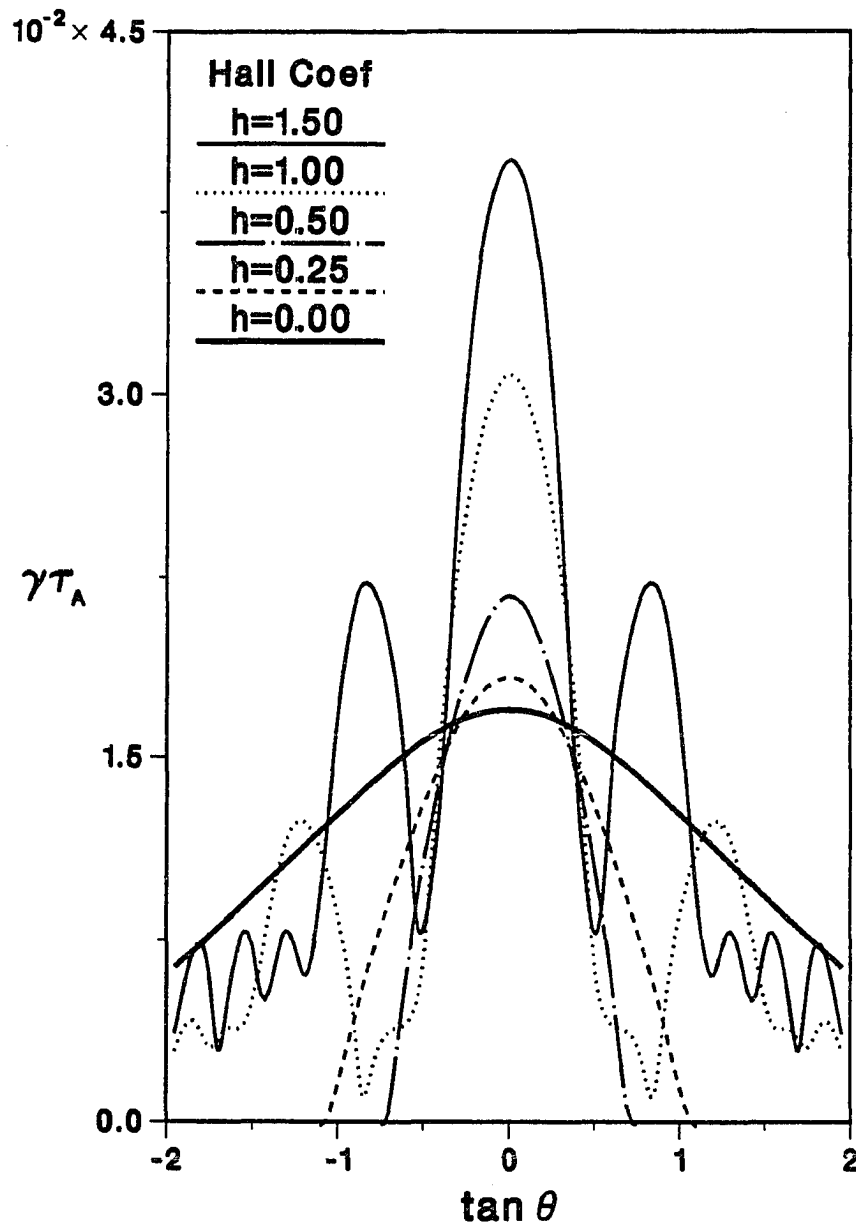


Figure 5.2 The normalized growth rate $\nu \tau_A$ as a function of $\tan \theta$ for several Hall coefficients $h = l_i / \Delta = 0, 0.25, 0.5, 1., 1.5$. The thick solid curve for $h = 0$ reproduces the FKR result. The normalized z component of wave vector $\alpha_z (= k_z \Delta)$ is 0.3. The Lundquist number S is set to 1000. The numerical method for calculating the complex frequency is described in the text (from Cao and Kan, 1991)

Figure (5.2) shows the θ dependence of the normalized growth rate $\gamma\tau_A$ for several values of h . The Lundquist number S ($=1000$) is constant in Figure (5.2). The thick solid line with $h = 0$ reproduces the FKR growth rate that decreases monotonically with increasing $|\theta|$. With the FIIL effect ($h > 0$), the growth rate is raised about $\theta = 0$, but is reduced when $|\theta|$ is further increased. The tearing mode becomes unstable only in a relatively narrow band of angles about $\theta = 0$, and the width of the main peak in the growth rate decreases as h increases. This result differs from FKR case where all waves propagating at an angle to the magnetic field other than the right-angle are unstable. When the current sheet thickness Δ is equal to or smaller than the ion inertial length l_i (Hall coefficient $h = l_i/\Delta \geq 1$), the tearing mode becomes unstable in several bands of the angle θ in addition to the main one about $\theta = 0$.

Figure (5.3) shows the θ dependence of the normalized phase velocity for several values of h . All other parameters are the same as in Figure (5.2). The normalized phase velocity is defined as $\omega/(kV_A) = \omega\tau_A/\alpha < h$, where ω is the real frequency of growing tearing modes and the Alfvén velocity $V_A = B_{z0}/\sqrt{4\pi\rho_0}$. It is shown in Figure (5.3) that a purely growing tearing mode in the MHD limit begins to drift when the FIIL effect is included. For the parallel propagation ($\theta = 0$) or without the FIIL effect ($h = 0$), the phase velocity is zero and the tearing instability is a purely growing mode. For the oblique tearing mode ($\theta \neq 0$), the FIIL effect leads to a nonzero phase velocity that increases steadily with h and $\tan\theta$. The drifting of oblique tearing modes in a thin current sheet can be responsible for magnetic reconnection sites to relocate and may be a cause of the intermittent reconnection at the dayside magnetopause. In order for a tearing mode to reconnect significant fluxes, however, the real frequency ω associated with the drifting velocity of oblique tearing modes must be smaller than the growth rate γ at which the reconnected flux is generated. Otherwise, the reconnected flux can be swept away from the source region where the tearing instability is triggered. At the finite dayside magnetopause, the reconnection sites of tearing may be limited to the nose

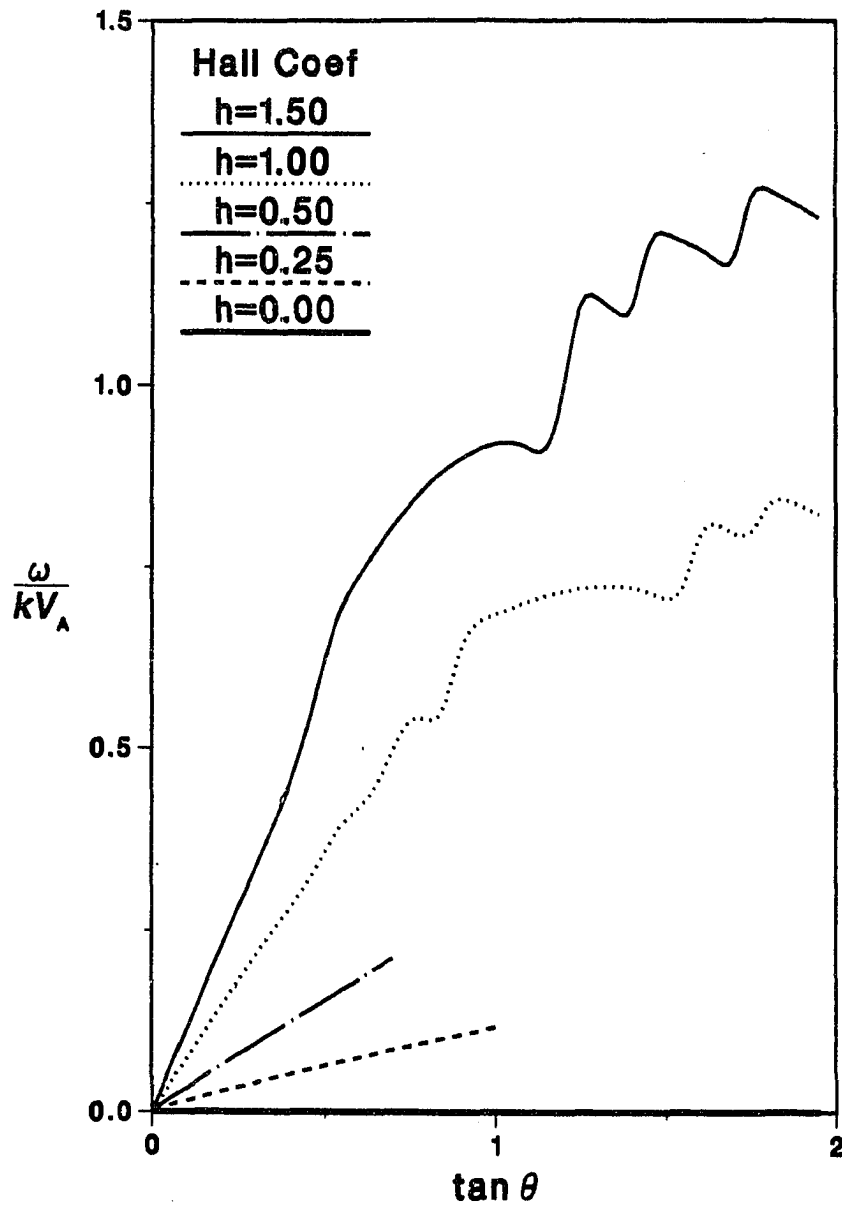


Figure 5.3 The normalized phase velocity $\omega/(kV_A)$. ω is the real frequency of an oblique tearing mode and $V_A = B_{z0}/\sqrt{4\pi\rho}$ is the Alfvén speed. All other parameters are the same as in Fig. (5.2) (from Cao and Kan, 1991).

of the dayside magnetopause, where the tearing mode is more unstable due to a thinner current sheet and takes more time to travel to the edge of the current sheet.

It will be shown in the next chapter that the tearing instability is triggered by squeezing the current sheet against the X-lines. The magnetic fluxes and the associated current density near the X-lines build up until the rate of resistive diffusion, which leads to slip of the field lines with respect to the plasma, matches the rate at which the magnetic fluxes are being swept into the region. The FIIL effect, which also marks the breakdown of the frozen-in MHD approximation, plays an important role in an intermediate region scaled by the ion inertial length around the magnetic field null. The existence of the FIIL effect in the intermediate region may facilitate the magnetic field lines to slip with respect to the plasma, and hence can cause the enhancement of the tearing instability. As indicated by the generalized Ohm's law (5.4a), part of the electric field must be taken to drive an additional ion flow along the electric field, so that the current density associated with the resistive term must be reduced. This means that "effective conductivity" is increased. Therefore, the growth rate of parallel tearing ($\theta \approx 0$) will be raised when the FIIL effect is included. Either the FIIL effect or the oblique propagation can bring about the vortex electric current in the tearing plane (X - Z plane) and the associated B_Y component. Nevertheless, in the MHD limit these Y-components associated with the vortex current in the tearing plane are not a cause, but an effect of the oblique MHD tearing process, since they are decoupled with the plasma flow and magnetic field in the tearing plane as indicated in the governing equations (5.6)-(5.9). When the FIIL effect is included, the Y-components generated by the oblique MHD tearing process will be coupled to the flow and field in the tearing plane. As a result, the growth rate of oblique tearing is reduced and the tearing mode becomes drifting. It can be concluded that the generation of Y-components by the FIIL effect alone tends to enhance the instability, while the generation of Y-components due to the oblique propagation tends to suppress it. When the current sheet thickness becomes

equal to or smaller than the ion inertial length, the FIIL effect on oblique tearing not only takes place in the inner region around the magnetic field null, but also modifies the MHD plasma flow and the magnetic field in the outer region. For drifting oblique tearing, the plasma flow and the magnetic field in the outer region, where the ambient magnetic field is strong and the resistive effect is negligible, are inclined to propagate with a local Alfvén speed, while the X- and O-lines of magnetic islands tend to move slowly because of the significance of resistivity effects in the inner region around the magnetic field null. Thus the drift velocity of oblique tearing is a hybrid of the rapid propagation of the Alfvén mode wave and the relatively slow process related to the resistivity near the field null. Since the plasma flow and the magnetic field in the outer region tend to drift along the wave vector k faster than those in the inner region, the classic plasma flow pattern and the magnetic island structure associated with MHD tearing will be distorted for oblique tearing with the FIIL effect. The plasma flow, which is towards X-lines in MHD tearing, may be shifted to above the next O-lines where the plasma flow is supposed to be outward, so that the tearing mode can be suppressed. However, as the propagation angle $|\theta|$ is further increased, the differential drifting motion between the inner and outer regions may become so large that the inward plasma flow above one X-line can be shifted to above the next X-line (see flow patterns in Figure 5.6). As a result, the growth rate will be raised again. Therefore, it is possible for the multiple peaks in growth rates to occur in an extremely thin current sheet for the highly oblique mode.

Figure (5.4) shows the normalized growth rate for several Lundquist numbers S . The Hall coefficient h ($= 1.0$) is constant in Figure (5.4). The Lundquist number or magnetic Reynolds number S , which is inversely proportional to the resistivity η and measures the relative importance of diffusion and convection, would have a major impact on the magnitude of growth rates, but little effect on the θ dependence. As shown in Figure (5.4), the normalized growth rates increase with decreasing values of S , but the positions of the peaks and dips

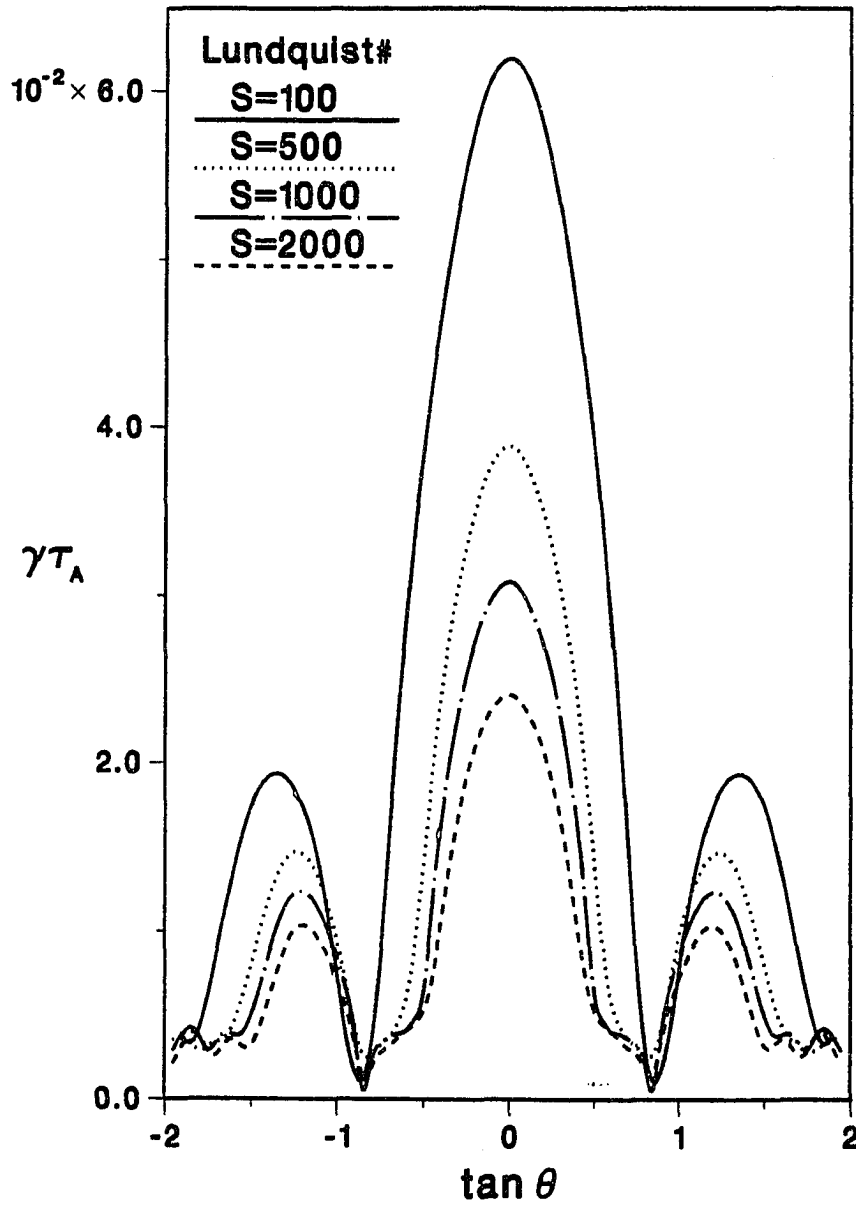


Figure 5.4 The normalized growth rate $\nu\tau_A$ as a function of $\tan\theta$ for several Lundquist numbers $S = 100, 500, 1000, 2000$. The Hall coefficient h and the normalized z component of wave vector α_z are set to 1 and 0.3, respectively (from Cao and Kan, 1991).

in growth rates are somewhat independent of S . In contrast, the Hall coefficient h , which measures the importance of the FIIL effect, is a key parameter in determining the θ dependence of growth rates as shown in Figure (5.2).

Figure (5.5) shows the magnetic field lines and B_Y components for several values of h and $\tan \theta$. The total magnetic field shown in Figure (5.5) is a linear eigen-function evaluated at finite amplitude and added to the background reversal magnetic field $B_0(x)$. Panel (A) is for an oblique tearing mode in the MHD limit. The magnetic island structure, which is one of a classic tearing mode in a magnetic reversal layer, is displayed on the left side of Panel (A). Contours of self-generated B_{Y1} components, which also stand for the vortex current lines in the tearing plane $X-Z$, are shown on the right side of Panel (A). Panel (B) is for parallel tearing ($\theta = 0$) including the FIIL effect ($h = 1$). It has been known that B_{Y1} and V_{Y1} components for a tearing mode in the MHD limit are zero in a case of parallel propagation ($\theta = 0$). However, when the FIIL effect is included, the B_{Y1} components are generated even at $\theta = 0$. The magnetic island structure shown in Panel (B) is similar to that in Panel (A). The extent of nonzero B_{Y1} components in Panel (B) is approximately scaled by the ion inertial length, which is equal to Δ ($h = l_i/\Delta = 1$). In comparison, the characteristic length of B_{Y1} gradient normal to the reversal magnetic field is of the diffusion layer width, as indicated in Panel (A). One can also notice that the B_{Y1} components in Panel (A), which are generated due to the oblique propagation in the MHD limit, have a $\pi/2$ phase difference relative to those in Panel (B) due to the FIIL effect. Panels (C) and (D) show the magnetic field for the oblique tearing mode including the FIIL effect. Two specific propagation angles ($\tan \theta = 0.3$ and $\tan \theta = 1.2$) are assumed in Panels (C) and (D), respectively. The FIIL effect on oblique tearing results in a distortion of the magnetic islands and B_{Y1} components. This distortion reflects both the FIIL and the oblique propagation effects. Panels (C) and (D) display a two-layer structure in B_{Y1} components. The B_{Y1} in the inner layer, which has a width of the

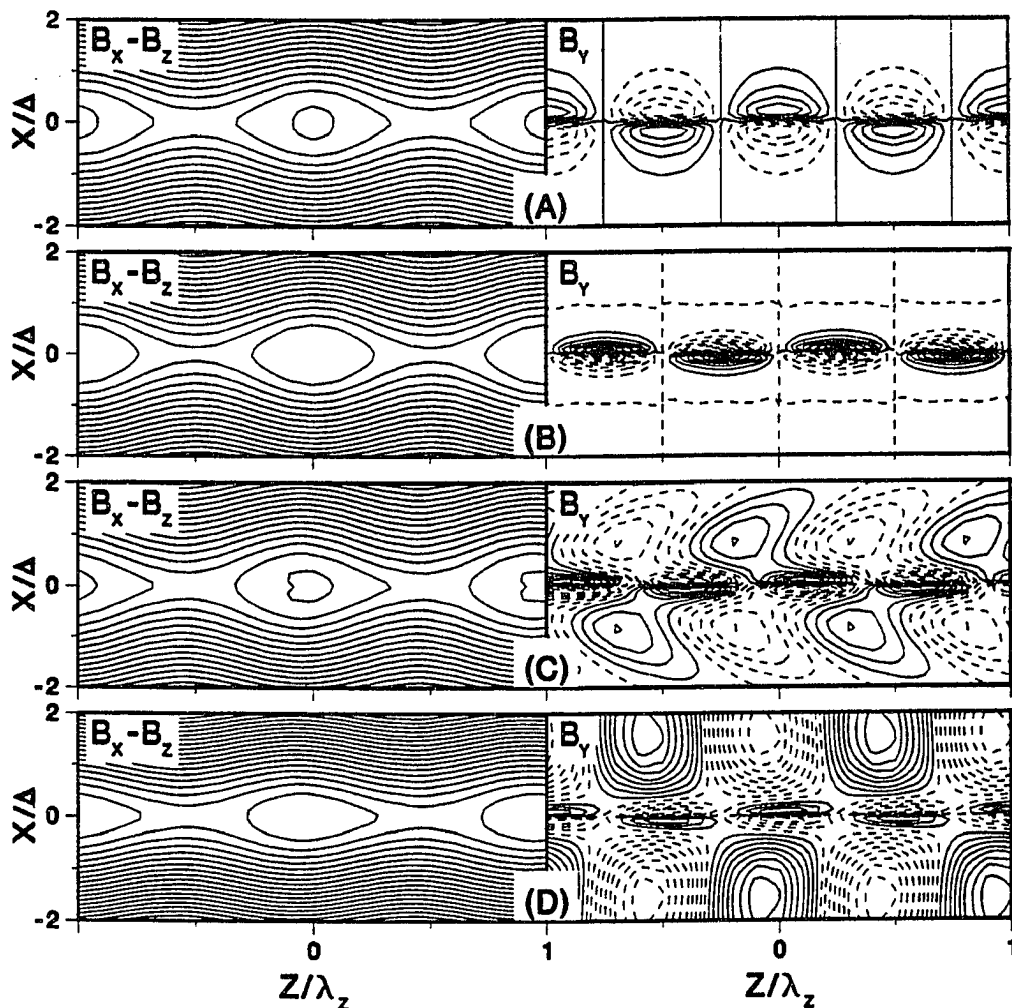


Figure 5.5 Magnetic field lines and B_Y components for several values of h and $\tan \theta$. The Lundquist number S is set to 1000. X is normalized by the current sheet thickness Δ and Z by the wavelength $\lambda = 2\pi/k$. Panels on the left side show the magnetic field lines in the tearing plane X - Z , while Panels on the right side show contours of the magnetic B_{Y1} components. The solid and dash contour lines are for positive and negative B_{Y1} value. (A) For the oblique tearing mode in the MHD limit; $h = 0$, $\tan \theta = 0.3$. (B) For the parallel tearing mode including FIIL effect; $h = 1$, $\tan \theta = 0$. (C) For the oblique tearing mode including FIIL effect; $h = 1$, $\tan \theta = 0.3$. (D) Same as Panel (C), except $\tan \theta = 1.2$ (from Cao and Kan, 1991).

diffusion layer, gradually changes its sense to one in the outer layer scaled by the ion inertial length, when crossing the magnetic reversal layer.

When k_y becomes comparable to k_z or the current sheet thickness becomes comparable to the ion inertia length, the B_{Y1} component is found to be of the same order as the other perturbation components, so that 3-D deformation of the field structure turns out to be significant. The magnetic structure shown in Panel (A) and (B) can be transferred to a 3-D structure. The B_{Y1} magnetic component shown in Panel (B) will cause the field lines around the O-lines are pulled in the y -direction, while the B_{Y1} in Panel (A) will result in that the magnetic field lines between X- and O-lines around $z/\lambda = -0.25$ and 0.25 are pulled in the $-y$ and $+y$ directions.

Figure (5.6) shows the plasma flow patterns with all parameters and notations kept to be the same as in Figure (5.5). Panels on the left side show the velocity streamlines (V_X, V_Z) in the tearing plane. Panels on the right side show contours of V_Y component, which is responsible for the generation of the vorticity in the tearing plane. Panel (A) is for an oblique MHD tearing mode, in which the plasma flows towards the X-line, is then being swept into the magnetic island and expelled at the O-line. The V_Y component generated in the MHD limit by the oblique propagation is confined in the diffusion layer around the magnetic null. Panel (B) shows the plasma flow for a parallel tearing ($\theta = 0$) including the FIIL effect ($h = 1$). The flow pattern shown on the left side of Panel (B) is similar to that in Panel (A), except for the difference in the characteristic gradient length. In Panel (B) V_{Y1} components, whose extent is scaled by the ion inertial length, are zero at the center of the magnetic reversal layer and have a $\pi/2$ phase difference with those in Panel (A). Panels (C) and (D) show the plasma flow pattern for the oblique tearing mode including the FIIL effect. Two specific propagation angles ($\tan \theta = 0.4$ and $\tan \theta = 1.2$) are taken in Panels (C) and (D), respectively. The deformation of plasma flow patterns results from both the FIIL and oblique propagation effects. The tilted flow pattern shown in Panel (C) can no longer effectively provide the magnetic flux for the

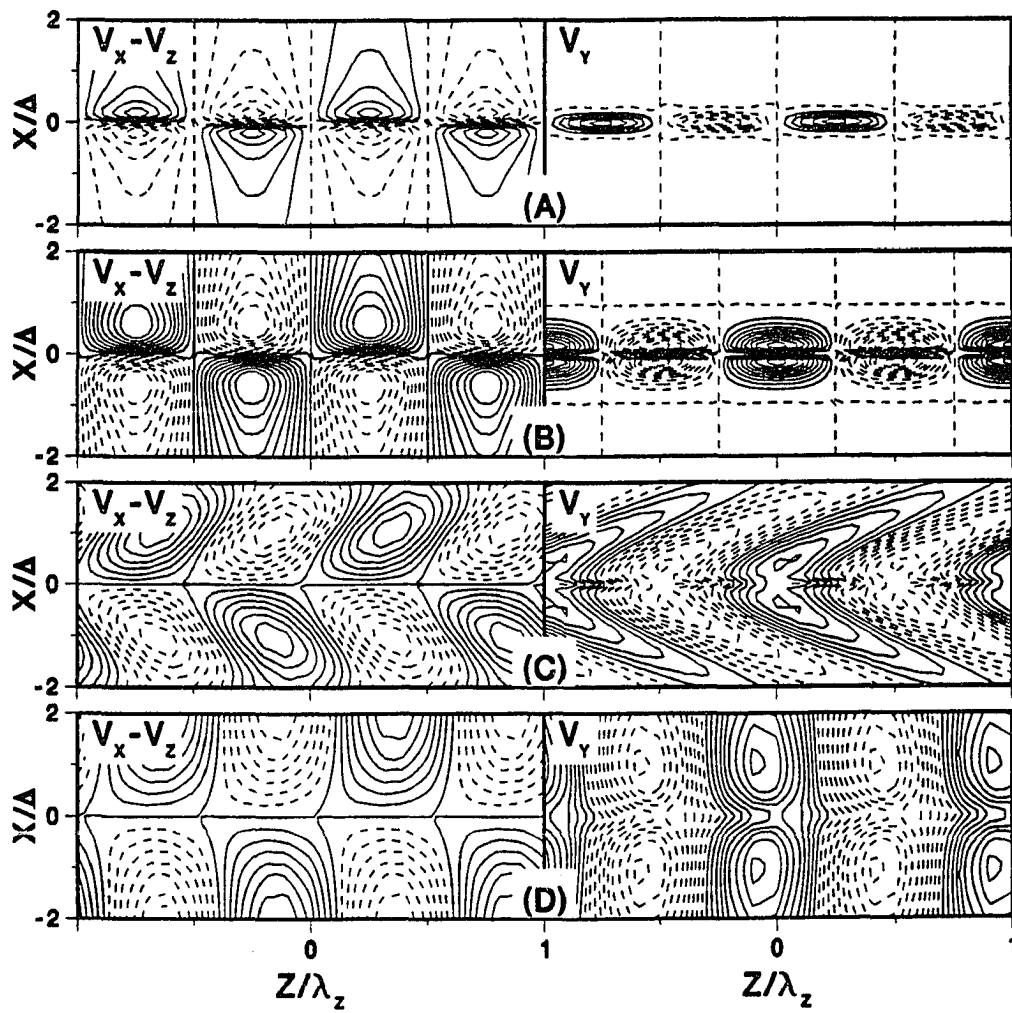


Figure 5.6 Stream lines and V_Y components. All parameters and notations are kept the same as in Fig. (5.5).

magnetic diffusion at $x = 0$ so that the growth rate of the tearing mode in a thin current sheet decreases dramatically with θ increase as shown in Figure (5.2). When further increasing θ , a second peak in the growth rate will occur as indicated in Figure (5.2). Panel (D) shows The corresponding flow pattern. The flow pattern on the left side of Panel (D) is similar to those in Panels (A) and (B). However, there exists a $\pi/2$ phase difference and the flow velocity is reduced significantly in latter case.

5.3 Implications for Patchy and Intermittent Reconnection

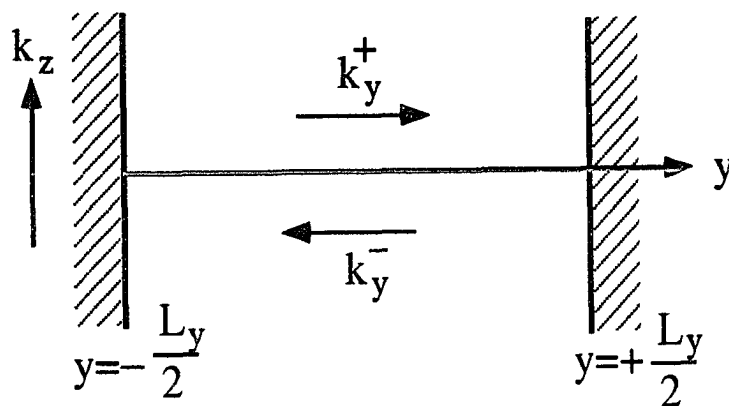


Figure 5.7 Tearing instability in a finite system. It is assumed that the tearing mode is confined within spatial boundaries at $y = \pm L_y/2$.

The oblique tearing mode discussed in the previous section is related to the current sheet of infinite extent in both y and z directions. Since the dayside magnetopause is a spatially finite system, the actual form of the 3-D tearing mode must incorporate the spatial inhomogeneity of the magnetopause. For applications of the results in the previous section to actual bounded systems, effects due to the reflection of waves from the boundaries have to be included. The

characteristic 3-D tearing mode of a finite system results from superposition of travelling tearing modes reflected by the two boundaries in the y -direction [Lifshitz and Pitaevskii, 1981]. As suggested by Quest and Coroniti [1981], the finite extent of the dayside magnetopause assures that the spatial extent of the tearing mode is bounded in the y direction (dawn-dusk), so that the tearing mode will grow only as the localized wave packet. A three-dimensional, full-wave solution for the tearing mode in a finite current sheet is beyond the scope of the present study. However, as a first crude model, the 3-D tearing mode may be treated as a superposition of two oblique modes, which have the same wavelength and growth rate, but propagate in the opposite y direction ($\psi_1 \sim \exp[i(k_y y + k_z z)]$ and $\psi_2 \sim \exp[i(-k_y y + k_z z)]$) as shown in Figure (5.7). Such a superposition, which corresponds to a perfect reflection at the boundaries and neglects the other wave modes, is admittedly not self-consistent, it will serve as a first approximation in illustrating the physics of such spatially bounded modes.

Figure (5.8) shows a localized wave packet produced by the oblique tearing instability. Figure (5.8A) is in the MHD limit, while Figure (5.8B) includes the FIIL effect. In comparison with Figure (5.5) which shows a single tearing mode related to unbounded systems, Figure (5.8) shows the characteristic tearing instabilities of a finite system resulting from superposition of travelling tearing modes reflected by the two boundaries in the y direction. The 3-D magnetic island structures depicted in Figure (5.8) are simply results of a superposition of the background magnetic field B_0 and the two oppositely propagating tearing modes as shown in Figure (5.7). It has been known that the linear exponential growth terminates at small amplitudes and the small magnetic island formed in the linear stage is confined in a narrow tearing layer near the field null. Since an island of the size of the tearing layer in the linear stage would not be visible on a normal field line plot, the magnetic field of tearing wave packets in Figure (5.8) is evaluated at a small but finite amplitude (about two percent of the ambient magnetic field), so that the island structure and the isolated X-segment can be clearly shown. The meshed surface

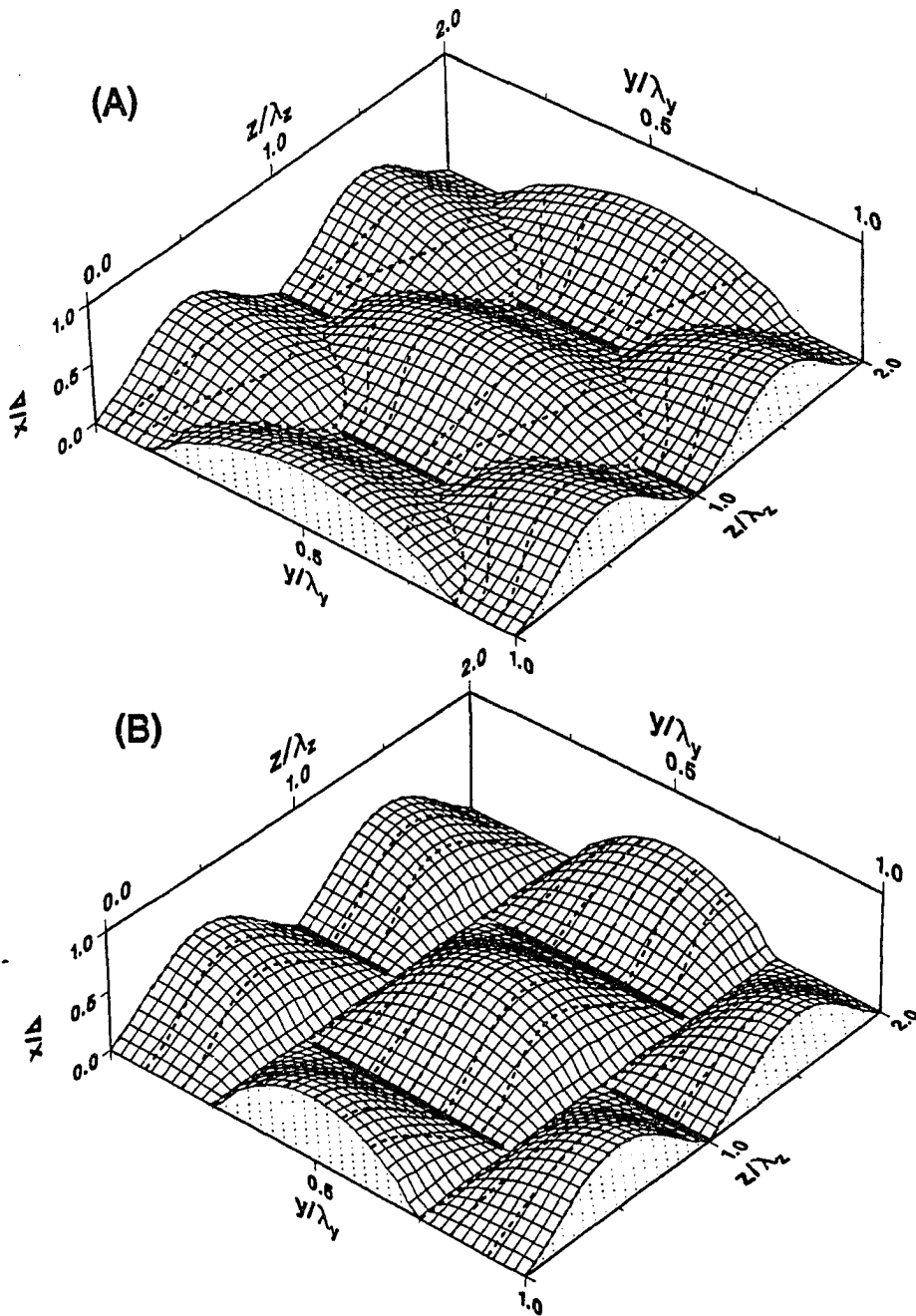


Figure 5.8 3-D magnetic island structure produced by a tearing wave packet. The current sheet is represented by the dotted $y-z$ plane. The top grid mesh indicates a magnetic surface on which magnetic field lines drape around. The bold line segments located at the bottom of valleys are the X-segments associated with localized reconnection sites. The dash lines on the mesh surface are the magnetic field lines, which are interconnected at the X-segments to the field lines on the other side of the current sheet to form the isolated magnetic islands. The wavelengths in the y and z directions are set to be $\lambda_y \approx \lambda_z \approx 20\Delta$, and the Lundquist number S is 1000. (A) In the MHD limit ($h = 0$); (B) Including the finite-ion-inertial-length effect ($h = 1$) (from Cao and Kan, 1991).

in Figure (5.8) is a magnetic separatrix surface between regions occupied by the closed and open field lines. The closed field lines form an isolated magnetic island that is bounded by the magnetic separatrix surface, topologically a sphere that intersects with the current sheet along X-segments indicated by the bold line segments.

In contrast with 2-D tearing ($k_y = 0$) which has one infinite y dimension resulting in the X-lines and infinite cylinders containing the magnetic islands, 3-D tearing leads to isolated reconnection regions and bounded magnetic island surfaces on which the magnetic field lines drape around, as shown in Figure (5.8). The characteristic features of 3-D magnetic island structures depicted in Figure (5.8) are similar to those captured by Russell and Elphic [1979] in the flux transfer event (FTE), in which the isolated flux tubes rotate across the dayside magnetopause with the magnetosheath field lines draping around on one side and magnetospheric field lines on the other side.

The wavelength λ_y of tearing mode wave packets is expected to be smaller than the characteristic width of the finite dayside magnetopause in the y direction, *i.e.*, $\lambda_y \leq L_y$ or $k_y \geq 2\pi/L_y = k_{min}$ where L_y is the width of current sheet in the y direction and k_{min} is a corresponding minimum wave vector required by the finite current sheet at the dayside magnetopause. Only a tearing mode with a maximally growing wave number should survive for more than an e -folding period to produce a significant interconnection of the oppositely directed field lines. If the growth rate decreases monotonically with k_y increase as in the case of MHD tearing, the maximally growing wave number of the finite current sheet is equal to $k_{min} = 2\pi/L_y$ ($\lambda_y = L_y$). As shown in Figure (5.8A), an X-line in 2-D tearing is broken up into X-segments in 3-D tearing. These X-segments are represented in Figure (5.8A) by the dark line segments at the bottom of valleys. The length of X-segments corresponding to the dimension of the isolated reconnection sites is expected to be smaller than a half width of the dayside magnetopause in the dawn-dusk direction.

Figure (5.8B) shows the 3-D magnetic island structures including the FIIL effect. The degree of patchiness increases as the dimension of reconnection sites decreases with decreasing thickness of the magnetopause current sheet. It has been shown in Figure (5.2) that there are several peaks in growth rates with increasing k_y , when the current sheet thickness is equal to or smaller than the ion inertial length. Thus, for the thin current sheet, the tearing wave packet with $k_y > k_{min} = 2\pi/L_y$ may become more unstable than the $k_y = k_{min}$ mode. If so, the maximally growing tearing packet with a wavelength $\lambda_y < L_y$ will bring about the multiple X-segments and multiple magnetic islands in the y direction. When $\lambda_y < L_y$, one can expect that the structure in Figure (5.8B) with one wavelength λ_y will extend in the dawn-dusk (y) direction periodically to cover the whole dayside magnetopause. Therefore, the finite dayside magnetopause with a thin current sheet not only makes it possible for the multiple X-lines to occur in the z direction as argued by Lee and Fu [1985], but also raises the possibility of several localized X-segments in the y direction as proposed by Kan [1988] and Nishida [1989]. It should be noted that the magnitudes of two oppositely propagating modes in Figure (5.8B) are chosen to be the same, so that the wave packet behaves like a standing wave without drifting. In reality, the configuration shown in Figure (5.8B) can be expected to change with time.

5.4 Discussion and Summary

I have presented the results of oblique resistive tearing in a thin current sheet. The results indicate that due to the FIIL effects the tearing instability is enhanced for parallel propagations ($\theta = 0$), but is suppressed for oblique propagations. For a thin current sheet whose thickness is equal to or smaller than the ion inertia length ($h \geq 1$), the tearing mode is unstable in several bands of the angle θ and also has a significant phase velocity.

These results may provide a support for the theoretical idea that elbow-shaped FTEs at the dayside magnetopause can be produced by 3-D tearing, resulting in the patchy and intermittent reconnection as proposed by Kan [1988]. For a thin current sheet, the FIIL effect may lead to several isolated X-segments in the dawn-dusk direction. However, the plasma flow and the drift of the tearing instability toward the boundary of the dayside current sheet, may limit 3-D tearing to the equatorial plane as discussed by Kan [1988]. The drifting nature of 3-D tearing in a thin current sheet, coupled with the unsteady solar wind, may provide a possible explanation for the intermittent reconnection at the dayside magnetopause. The 3-D tearing wave packet displays a finite magnetic island structure consistent with the elbow-shaped FTE signatures. The patchiness of dayside reconnection, originated in 3-D tearing, should be determined by the dimension of the X-segments associated with the most unstable tearing wave packet. The z-dimension of FTEs is about 20 times the current sheet thickness for the most unstable tearing mode. The y dimension of the FTEs, depending on the size of the current sheet, is generally smaller than the half width of the magnetopause current sheet in the y direction. Both dimensions can be estimated to range up to one or two R_E .

Either the FIIL effect or the oblique propagation can lead to a vortex current responsible for the B_y component and twisting of the magnetic field lines in FTEs. Nevertheless, the 3-D deformations of magnetic field lines are usually contrary in two cases. For the wave packets of 3-D MHD tearing, the magnetic field lines shown by the dashed lines in Figure (5.8A), spread out from the top of the magnetic surface, while those due to the FIIL effects are piled up in Figure (5.8B). These peculiar features of B_y and associated vortex currents may serve as a tool in a further observational analysis of B_y components, and in determining the relative importance of proposed B_y generation mechanisms.

It should be noted that the FIIL effects in the fluid approximation may not carry over directly into the particle simulations due to the different dissipation mechanisms of the resistive

and collisionless plasmas. Because of its larger inertia, the ion always lags behind the electron. The difference in the ion and electron motions leads to a vortex current with the B_y component normal to the tearing plane. The separation between the electrons and ions can also produce an electrostatic potential. It has been found in the particle simulations that the allowance for a finite B_y has little effect on the linear tearing growth rate [Swift, 1986; Hoshino, 1987]. It seems that the B_y is the consequence rather than the cause of the FIIL effect on the tearing instability. In contrast, the electrostatic field due to the FIIL effect can affect the resonant current in the collisionless plasma, to modify the linear tearing growth rate. Hoshino [1987] found that the electrostatic field reduces the tearing growth rate in an antiparallel magnetic field configuration, but raises the growth rate in a strong sheared magnetic field configuration. In the antiparallel magnetic field configuration, the reduction of the growth rate is due to the generation of an additional ion resonant current, which results from the ion concentration in the neutral sheet. This resonant phenomenon in particle simulations is not expected to manifest in the fluid description. The fluid description should be more meaningful in the strong shear magnetic field configuration, in which the electron and ion gyroradius are small compared to the current sheet thickness. The particle simulations in the case of the strong shear magnetic fields [Hoshino, 1987; Katanuma and Kamimura, 1980] have shown the enhancement of the tearing instability, consistent with the results of fluid theory described in this chapter.

CHAPTER 6

Coalescence of Magnetic Islands Created by Tearing Modes

In the previous chapter I have examined the linear tearing instability in a thin current sheet. It is found that the tearing instability in a thin current sheet can be responsible for the patchy and intermittent reconnection at the dayside magnetopause. The study in this chapter is to discuss the possibility of nonlinear tearing evolution in terms of magnetic island coalescence.

It has long been believed that the current line attraction leads to the tearing instability that reorganizes the current sheet into a series of current filaments, each of which produces a magnetic O-line; then the adjacent pairs of current filaments are attracted each other and the two magnetic islands later merge by the coalescence instability as schematically shown in Figure (6.1). In contrast with this usual picture, it is found that the tearing instability creates the stretched magnetic islands with current maxima at X-lines, which seems against the island coalescence. The sequence of the nonlinear tearing evolution is also not yet totally clear. In the resistive MHD simulations, there is no indication of the magnetic island coalescence and the stretched magnetic islands with current filaments at X lines are the peculiar features of the nonlinear tearing. In the particle simulations, one has frequently observed the two peculiar phenomena of island coalescence: the small island and large island coalescence. The width of small islands is much smaller than the current sheet thickness, while that of large islands is comparable to the current sheet thickness.

In this chapter, I shall show that the tearing-created small islands with the current maxima at X-lines can coalesce into large ones. However, the small island coalescence is not due to the attraction between the current maxima and thus is quite different from the large island coalescence. I try to make clear the consequence and the relative importance of the small and

large island coalescence in the nonlinear evolution of the tearing instability. It is argued that the role of the small and large island coalescence in the collisionless plasma depends on the current sheet thickness relative to the tearing layer width. When the current sheet thickness is much larger than the tearing layer width, the small island coalescence occurs with the current density concentrated along the separatrix surface. When the current sheet thickness is smaller than the tearing layer width, the large island coalescence will dominate. It will be also pointed out that the lack of the large island coalescence in the resistive plasma is due to its inability to move the current filaments from the X-lines to O-lines.

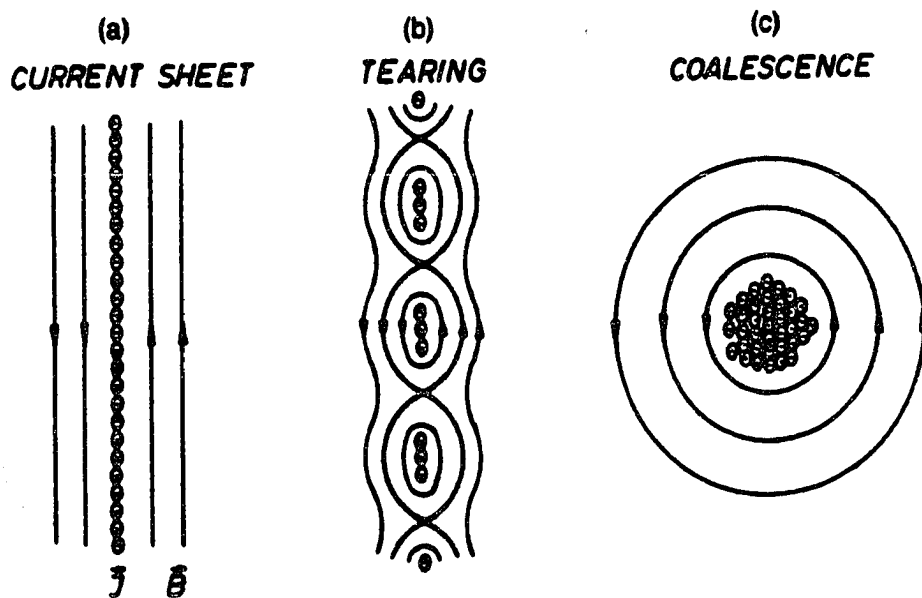


Figure 6.1 Three possible magnetic field topologies (solid lines) resulting from (a) current that flows in a neutral sheet and (b) a tearing mode that reorders the neutral sheet current into filaments, each of which produces a magnetic O-line. The X-lines separate neighboring current channels (c), a circular cross section of current that could be the result of a merging of pairs of filaments [Gekelman and Pfister 1986]

6.1 Introduction

It is well known that a current sheet with a reversal magnetic field is unstable due to the tearing instability to form a chain of magnetic islands [Furth *et al.*, 1963; Drake and Lee, 1977a]. As a result of nonlinear saturation, the chain of magnetic islands produced by tearing modes may be either at equilibrium or in a stage varying slowly over time [Rutherford, 1977]. On the other hand, it is also known that adjacent islands associated with the parallel currents tend to attract each other and to coalesce into larger ones [Finn and Kaw, 1977; Pritchett and Wu, 1979; Biskamp and Schindler, 1971; Biskamp and Welter, 1980]. The attractive force between two neighboring current-carrying islands is essentially an ideal MHD effect, and it is therefore not surprising that the coalescence instability corresponds to a rapid growth on MHD time scales, while the tearing instability is a slow process associated with the diffusion of magnetic field lines by the finite resistivity or inertia. Thus, the nonlinear evolution of tearing instabilities by coalescence of magnetic islands is important for the study of magnetic reconnection. It bridges the gap between the tearing instability and the fast reconnection.

Although the coalescence of magnetic islands associated with the parallel current have been confirmed both analytically and numerically [Finn and Kaw, 1977; Pritchett and Wu, 1979], it is not at all certain that the chain of islands originally created by the tearing instability will coalesce. In all previous studies of coalescence instabilities, both analytic and numerical, an exact class of MHD equilibrium with magnetic islands [Fadeev *et al.*, 1965; Kan, 1972] has been taken as a starting point. Each of these equilibria is characterized by a periodic chain of magnetic islands within which there is a nonuniform current density peaked at the center of each island. The tendency to coalesce can be understood on physical grounds since it simply means that parallel currents (and therefore the O-lines) attract one another. It is beyond dispute that given the presence of several islands with current filaments they will indeed coalesce due

to the current attraction of filaments. Nevertheless, it is not clear if the magnetic islands created by the tearing instability are subject to the island coalescence.

The tearing instability, triggered by squeezing the current sheet against the X-lines, produces a chain of magnetic islands with the maximum current density at X-lines and the minimum current density at O-lines. The current distribution in the magnetic islands produced by the tearing instability is opposite to that required for islands to coalesce, and thus seems unfavorable for initiating the coalescence instability. The nonlinear development of tearing by the coalescence of magnetic islands is considered to be responsible for the fast reconnection and has been widely observed in the particle simulation studies [Katanuma and Kamimura, 1980; Ambrosiano *et al.*, 1986; Ding *et al.*, 1986; Price and Swift, 1986; Swift, 1986; Hewett, *et al.*, 1988]. However, in the resistive MHD simulation, there is no indication that the island coalescence plays a major role in the nonlinear development of tearing instability [Matthaeus and Montgomery, 1981; Steinolfson and Hoven, 1984; Scholer and Roth, 1987; Shi *et al.*, 1988]. For the case of the random-noise initial conditions, the stretched magnetic islands with current filaments at X-lines are always observed for the evolution of nonlinear tearing in an MHD simulation. Although many theoretical and numerical studies have been conducted on the nonlinear tearing in the resistive MHD model, it seems uncertain what role the island coalescence might play in the nonlinear tearing.

In the next section I begin with a brief discussion about the current filamentation and the island structure associated with the tearing and coalescence instability, in an attempt to give a primitive physical picture for tearing instabilities. It is argued that a current filament associated with the tearing instability is a result of the current sheet pinch at X-lines rather than due to the parallel current line attraction. Then, I raise the question about what role the island coalescence can play in the nonlinear development of tearing mode. In section (6.3) an energy principle is used to analyze the stability of a quasi-equilibrium configuration with the small

periodic magnetic islands, which are created by the nonlinear evolution of one tearing mode perturbation. It is shown that under certain conditions the adjacent magnetic islands in the tearing mode can coalesce into larger ones. For a small island chain the question of stability is related to the external region and the unfavorable current distribution within the magnetic islands in tearing modes has little effect on the stability of magnetic island configurations. Our results will be compared with those in recent numerical simulation studies. Finally, the possibility of the large-amplitude islands with the current filaments at the O-lines will be discussed.

6.2 Tearing and Coalescence Instabilities

Tearing Instabilities

As shown in the previous chapter, the tearing instability can occur in a reversal magnetic field configuration, resulting in the current filamentation and a chain of small magnetic islands. The basic features of the instability are summarized in Figure (6.2), which shows a single magnetic island and current distribution produced by the tearing instability. The current filamentation at the X-line is localized only to a narrow tearing layer, where the existence of the resistivity or electron inertia can result in slip of the field lines with respect to the plasma, producing an induced electric field. Outside the tearing layer, the field lines remain frozen into the plasma and the fluid strongly resists detachment from flux lines, so that the induced perturbed current J_1 is always in a direction in which the resultant motor force $\mathbf{J}_1 \times \mathbf{B}_0$ opposes the fluid motion caused by the current attraction force $\mathbf{J}_0 \times \mathbf{B}_1$. The induced perturbed current J_1 results from the bending of the magnetic field lines that moves with the plasma. It is known that the tearing instability occurs only for the long-wavelength mode ($k\Delta < 1$), i.e., when the current thickness Δ is short compared with the wavelength of the mode. The physical origin

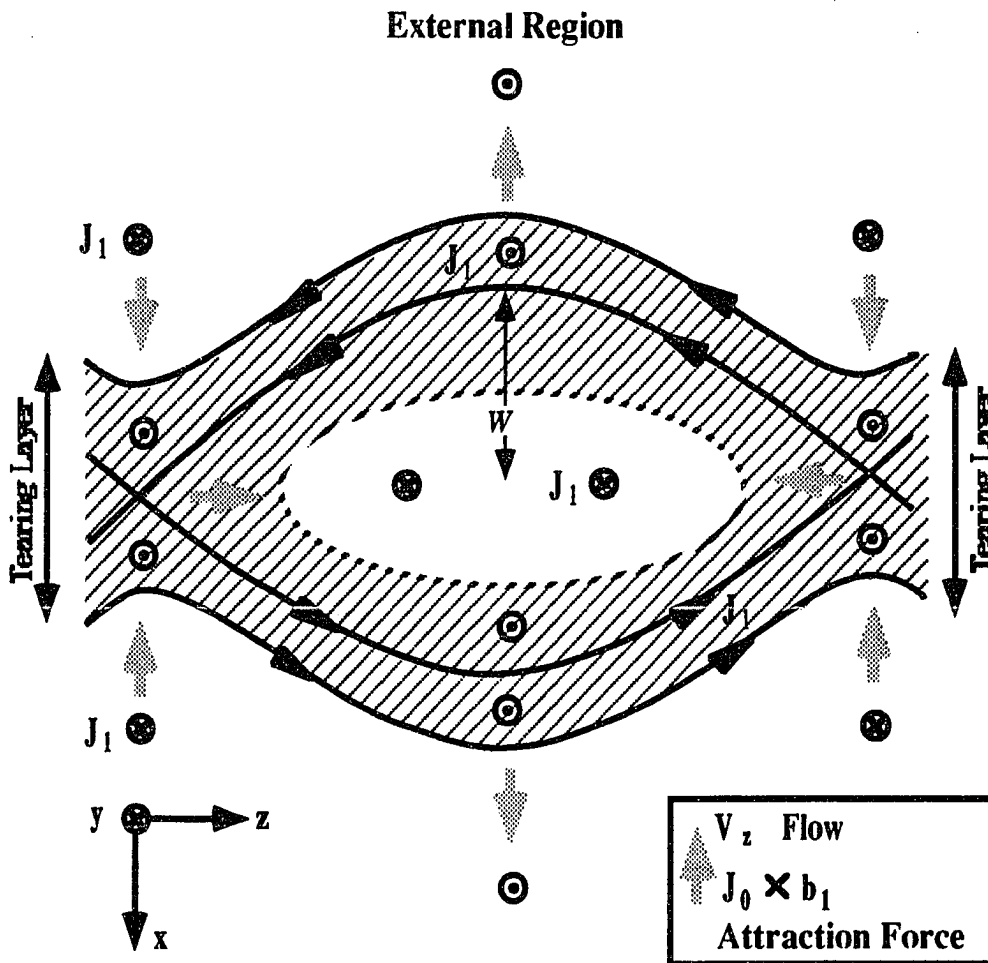


Figure 6.2 A sketch of a single magnetic island produced by a finite amplitude tearing mode perturbation. Magnetic field lines are shown by the dark lines. The perturbation current density is shown by vector heads and tails directed in and out of the page. In the central region of the island, the perturbed current J_1 is directed antiparallel to the equilibrium current J_0 . In the shaded region, J_1 is directed parallel to J_0 . The plasma flow is shown by the shaded arrows; Note that flow direction is the same as that of the current attraction force $J_0 \times b_1$ [reproduced from Coroniti and Quest, 1984].

of this effect is that the short-wavelength modes cause too much field line bending, which is stabilizing and brings about a strong motor force $\mathbf{J}_1 \times \mathbf{B}_0$, compared to the current attraction force $\mathbf{J}_0 \times \mathbf{B}_1$.

The current filamentation caused by the tearing instability may be understood in a physical picture as described below [Dungey, 1958; Matthaeus and Montgomery, 1981]. It is known that two fluid elements carrying currents of the same sign exert attractive forces on each other, even though the current distribution is not frozen in to the fluid as the magnetic field distribution is. The current density in a tearing mode is concentrated in the shaded area in Figure (6.2) and the maximum current density occurs near the X-line. The enhanced current distribution exerts an attraction force on like-signed elements, which are toward the X-line at the strong field corners above and below the X-line and away from it at weak field corners along the $B = 0$ line. As the magnetic field lines embedded in the fluid that is dragged into the strong field corners are stretched near the center of the current sheet, the local current density (proportional to $\nabla \times \mathbf{B}$) is raised. This obviously enhances the strength of the current filaments, which then exert a greater attractive force, and so on. The local current density at the X-line builds until the rate of Ohmic dissipation (or electron acceleration) matches the rate which one of the magnetic fluxes is being swept into the region. The effect is not compensated for by anything that happens at the weak field corners of the X-line. There, fluid is expelled, but not in a way that stretches the embedded field lines or raises the local current density. A minimum of current density is found at an O-line. The fluid elements, however, are prohibited by the incompressibility of the material from flowing radially inward in such a situation. A mechanical pressure builds up which resists the flow toward the O-line. The magnetic fluxes are brought in at the weak field corners and expelled at the strong field corners. This results in a decrease of current density at the O-line.

The time evolution of nonlinear tearing modes has been theoretically investigated both in a resistive MHD [Rutherford, 1977; White *et al.*, 1977 Carreras *et al.*, 1979; Thyagaraja, 1981; Priest, 1985; Norris, 1989], and in a collisionless plasma [Drake and Lee, 1977b; Galeev, 1978; Coroniti and Quest, 1984]. All calculations found that linear exponential growth terminated at small perturbation amplitudes and was followed by a slower growth that was algebraic in time. The physical nature of the nonlinear evolution is transparent. At the linear-nonlinear transition, the perturbed O-line current density $J_1(0)$, which is oppositely directed to the equilibrium current density J_0 , increases and is nearly equal to the J_0 . The X-line perturbed current essentially equals the equilibrium current J_0 ; in time the region of enhanced current shaded area in Figure (6.2) expands outward. One does not expect $J_1(0)$ to exceed $-J_0$, and thus reverse the sense of the magnetic field lines near the O-line. The balance $J_1 \approx -J_0$ should first be achieved at the O-line, and then in time J_1 should approach $-J_0$ throughout the spatial region within the island over which $J_1 < 0$. Therefore the spatial extent of the $J_1 \approx J_0$ region in z should grow slowly in time as the island grows, through the vanishing of the source of magnetic energy driving the instability. When the magnetic island width exceeds the width of the tearing layer, the total current in the island is reduced and the induction electric field near O-lines vanishes, so that the tearing mode effectively saturates with an algebraic growth rate and the reduced current density is approximately constant within the island [Rutherford, 1977].

In summary, the tearing instability is triggered by squeezing the current sheet against the X-line and results in a current density maximum at the X-line and a minimum at the O-line. The formation of current filaments at the X-lines enhances the electromagnetic force that drives the tearing instability, while the current density decrease at the O-line will generate a repellent force that pushes the plasma out of the island and makes the island grow. The finite resistivity or electron inertia is responsible for the slip of the field lines with respect to the plasma, and

makes it possible for plasma to escape from the X-line so that the pressure will not be built up at the X-line against the electromagnetic driving force. Although the tearing instability has been well studied, the physical picture for the current filamentation in the tearing instability is still not very clear. The driving force for the tearing instability comes from the free energy stored in the magnetic field outside the tearing layer, and the instability results from the collapse of the sheet current to break up into a set of parallel pinches. The enhanced current density in the tearing instability is concentrated in a narrow tearing layer that is usually much smaller than the current sheet thickness in an early stage of the tearing instability. Therefore, it seems inappropriate to treat the current sheet as the series of current lines, which attract one another and bring about the current filamentation of the tearing instability as depicted in Figure (6.2). Furthermore, the tearing current distribution with the maximum at the X-line and the minimum at the O-line is in contrast with that in Figure (6.1), in which the current filament in the island produces a magnetic O-line.

Coalescence Instabilities

In comparison with the tearing instability that relies on the finite resistivity or electron inertia, the coalescence instability is expected to occur in an MHD equilibrium consisting of a chain of magnetic islands. The instability originates from the tendency of two parallel current lines to attract one another. The existence of coalescence instability was first proved by Finn and Kaw [1977] theoretically. The linear dynamics of the instability and the nonlinear process were demonstrated in a resistive MHD plasma [Pritchett and Wu, 1979; Biskamp and Welter, 1980; Bhattacharjee *et al.*, 1983] and in a collisionless plasma [Biskamp and Schindler, 1971; Taktakishvili and Zeleny, 1986].

Figure (6.3) shows the equilibrium configuration characterized by the chain of magnetic islands and the current density distribution, which is concentrated inside each of the magnetic

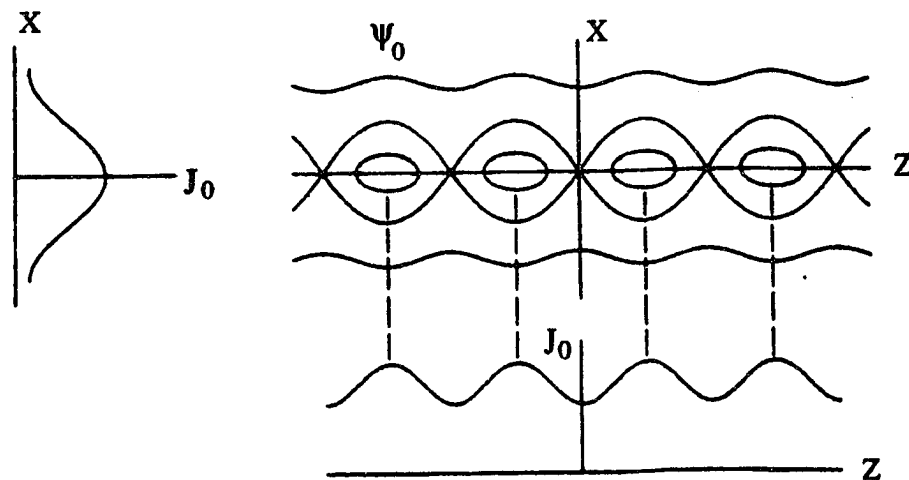


Figure 6.3 Equilibrium flux surfaces and current distributions in slab geometry [Finn and Kaw, 1977].

islands. The magnetic islands and the current density distribution in Figure (6.3) belong to an exact hydromagnetic equilibrium [Fedeev *et al.*, 1965; Kan, 1972], which satisfies the following equations

$$\begin{aligned} \psi_0 &= \ln(\cosh kx + \epsilon \cos kz) \\ J_0 &= \nabla^2 \psi_0 = (1 - \epsilon^2)k^2 \exp(-2\psi_0) \end{aligned} \quad (6.1)$$

where ψ_0 is the magnetic flux function, ϵ is a free parameter that determines the island width, and J_0 is the self-consistent current. Note that the magnetic island structure in Figure (6.3) can be interpreted as an array of current filaments superposed on a basic minimum current. The O-lines are the lines with the peak current in the filament and the X-lines are the lines with minimum current. The tendency to coalescence is now easy to understand on physical grounds since it simply means that parallel currents (and therefore the O-lines) attract each other. In

an ideal MHD a moving fluid carries flux with it. Since the flux cannot move through X-lines (where the resultant electric fields would drive infinite current in the zero resistivity limit), the instability will result in a distortion on the current maxima toward each other. The closer current filaments in turn lead to a greater attraction force, which will bring two current filaments even closer. In the linear stage, the coalescence instability should proceed on hydromagnetic time scales and therefore be quite rapid. The tendency of two O-lines to coalescence produces a piling up of flux on both sides of the X-line. This produces a stabilizing magnetic pressure that opposes the tendency to coalescence. Inclusion of resistivity should permit the merging process of two islands to proceed smoothly to completion with two O-lines and one X-line disappearing and an O-line emerging. The above physical argument of the coalescence mode where two magnetic islands spontaneously coalesce to form a larger island, was also supported by the MHD simulation as shown in Figure (6.4).

Comparison between the tearing and the coalescence instabilities

The tearing and coalescence instabilities are quite different in their associations with the current filamentation and the magnetic island formations. For the tearing instability, the current filaments at the X-lines and the associated magnetic islands are the products of squeezing the current sheet and reconnecting of magnetic field, while for the coalescence instability the current filaments at the O-lines of magnetic islands are prerequisite for the current attraction force that leads to the instability. Figure (6.5) shows two magnetic island structures associated with the tearing and coalescence instabilities. The total magnetic field in Figure (6.5) is treated as a small magnetic field b_1 due to the current filaments superposed on a background reversal magnetic field B_0 . Panel (A) depicts the magnetic field lines of the tearing instability, while Panel (B) displays the magnetic island responsible for coalescence instability. With a current filament at the X-line, the magnetic island generated by the tearing instability is stretched out

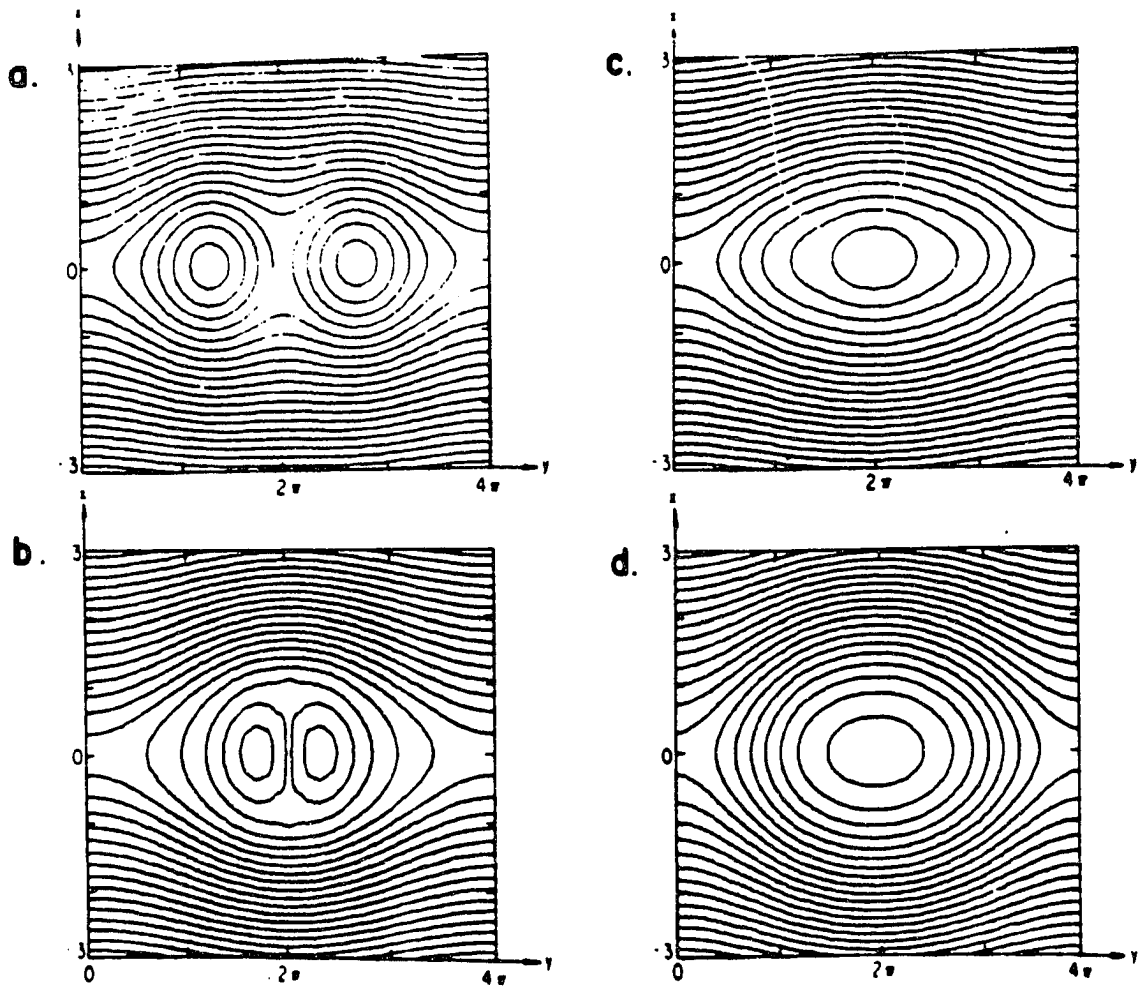
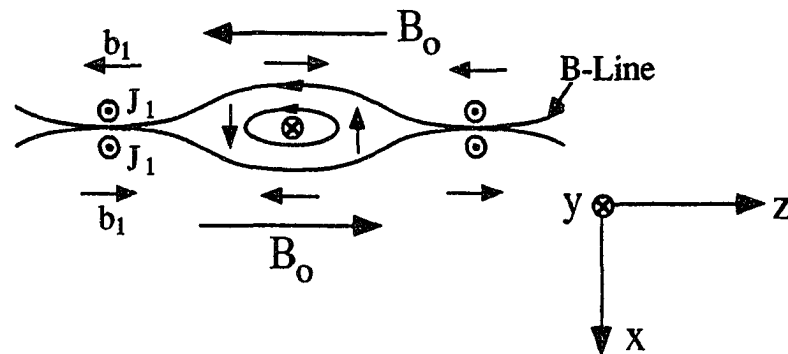


Figure 6.4 Nonlinear evolution of flux surfaces by the coalescence of magnetic islands [Pritchett and Wu, 1979].

along the z -axis as shown in Panel (A). In comparison, Panel (B) shows the fattened magnetic island, which is favorable for the coalescence instability, with the current filaments at the O-lines.

(a) Tearing: $\psi = -\ln \cosh x - \varepsilon \cos(kz)$



(b) Coalescence: $\psi = -\ln (\cosh kx + \varepsilon \cos kz)$

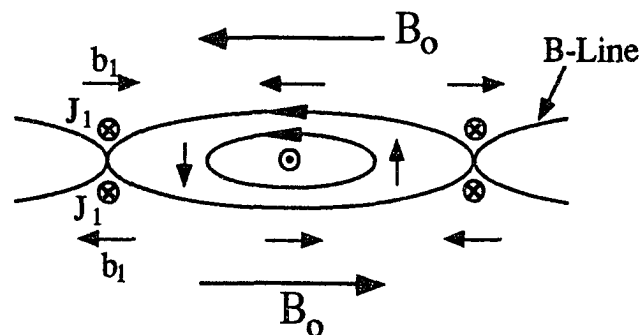


Figure 6.5 The magnetic island structure associated with the tearing and coalescence instabilities. (a) for the tearing instability, (b) for the coalescence instability.

Either tearing or coalescence instabilities may evolve into each other. When the coalescence instability develops, the current sheet at the interface between two approaching islands becomes thin and may then go unstable to secondary tearing on a much smaller scale [Biskamp,

1982]. Also, the primary tearing mode may produce many islands that are then attracted towards one another by the coalescence instability. The nonlinear development of tearing by the coalescence instability is long considered to be responsible for the fast reconnection and has been confirmed numerically in a collisionless plasma [Katanuma and Kamimura, 1980; Ambrosiano, *et al.*, 1986; Swift, 1986; Hewett, *et al.*, 1988]. With no initial perturbation except for an initialization noise due to finiteness of the simulation particle number, the most unstable tearing mode grows rapidly. After this mode grows and produces magnetic islands, a coalescence process follows in a rapid cascade to make the small-scale magnetic islands into larger ones whose dimension is comparable with the finite length of current sheet or the simulation box. If the wavelength of the most unstable tearing mode is comparable to the dimension of the current sheet of the simulation box, the nonlinear tearing is expected to evolve as a single mode without the coalescence.

It is noteworthy that the coalescence instability requires a series of magnetic islands within which there is a nonuniform current density with a maximum current filament at the O-line [Finn and Kaw, 1977]. Thus it appears that the current distribution during the nonlinear tearing growth phase, in which the current filament of the tearing mode is at an X-line and the minimum current density at an O-line, is unfavorable for the island coalescence. Even the saturated state of the nonlinear tearing mode, in which the current in the island becomes strongly uniform [Rutherford, 1977], may not be unstable to coalescence perturbations. In the next section I will use the energy principle to analyze the stability of the magnetic islands in a quasi-equilibrium that may arise in a saturated state of nonlinear tearing. It will be shown that the small magnetic islands can coalesce into larger ones and the question of stability is related to the external region. The negative current distribution within the magnetic islands in the tearing modes may reduce the growth rate of coalescence, but it is not strong enough to stabilize the system.

6.3 Coalescence of Magnetic Islands Created by Tearing Modes

In this section, I consider the stability of a quasi-equilibrium with periodic magnetic islands indicated in Figure (6.5a). This quasi-equilibrium could be the saturated state for the nonlinear evolution of the tearing mode perturbations. It has been known that the linear tearing terminates at a very early stage and the electron motion has already become adiabatic (apart from the vicinity of the X and O-lines) for very small islands. In the absence of the islands, the electron inertia or resistivity is required for relaxation of the current sheet system. The presence of the magnetic island, with a nonzero B_{0x} at $x = 0$ allows the plasma convection in the current sheet except near the X and O-lines. Therefore, it is possible to use the MHD energy principle in analyzing the stability [Pellat, 1983; Bondeson, 1983]. The analysis to follow will be restricted to two-dimensional, incompressible magnetohydrodynamics. The velocity and magnetic fields are represented in terms of the stream function ϕ and the magnetic flux function ψ ,

$$\mathbf{v} = \mathbf{e}_y \times \nabla \phi, \quad \mathbf{B} = \mathbf{e}_y \times \nabla \psi \quad (6.2)$$

and the ideal magnetohydrodynamic equations take the form

$$\frac{\partial \psi}{\partial t} + \mathbf{v} \cdot \nabla \psi = 0 \quad (6.3)$$

$$\frac{\partial \omega}{\partial t} + \mathbf{v} \cdot \nabla \omega = \mathbf{B} \cdot \nabla J \quad (6.4)$$

where $\omega = \nabla^2 \phi$ is the vorticity and $J = \nabla^2 \psi$ is the electrical current density. Rationalized Gaussian units with $c = 1$ are used throughout. The mass density is taken to be uniform ($\rho = 1$) in space and time. The distance from the center of the current sheet x is normalized to the width of the current sheet Δ .

In terms of the functions ϕ and ψ , the linearized ideal hydromagnetic equations for perturbations around the island equilibrium are

$$\frac{\partial \psi_1}{\partial t} = \mathbf{B}_e \cdot \nabla \phi_1 \quad (6.5)$$

$$\frac{\partial}{\partial t} \nabla^2 \phi_1 = \mathbf{B}_e \cdot \nabla J_1 + \mathbf{b}_1 \cdot \nabla J_e \quad (6.6)$$

where the subscript e denotes the equilibrium and the subscript 1 is for the perturbation.

The growth rate γ of an eigenmode can then be calculated in the standard manner of Bernstein *et al.* [1958] as the ratio of the potential energy δE and the integral K related to the kinetic energy

$$\gamma^2 = -\delta E/K \quad (6.7)$$

$$\begin{aligned} \delta E &= \frac{1}{2} \int \int (|\nabla \psi_1|^2 - \mathbf{J}_e \times \mathbf{b}_1 \cdot \xi_1) dx dz \\ &= \frac{1}{2} \int \int \left(|\nabla \psi_1|^2 + \frac{dJ_e}{d\psi_e} \psi_1^2 \right) dx dz \end{aligned} \quad (6.8)$$

$$K = \frac{1}{2} \int \int |\nabla \xi_1|^2 dx dz \quad (6.9)$$

The first term in (6.8), which is always positive and thus is stabilizing, is associated with the motor force encountered in trying to squeeze the flux surfaces up against the X-lines. The second term, which is destabilizing, is due to the term $\mathbf{J}_e \times \mathbf{b}_1$ in the equation of motion and represents the attraction of the current filaments. ξ_1 in (6.8) is the plasma displacement, and K stands for the kinetic energy integral. Therefore, the energy principle (6.7) simply states that the work done by the current attraction force (the term associated with $\mathbf{J}_e \times \mathbf{b}_1 \cdot \xi_1$) is equal to the sum of the magnetic energy (the term $|\nabla \psi_1|^2$) and the kinetic energy.

Now let us start with a two-dimensional periodic quasi-equilibrium created by one tearing mode.

$$\psi_e = \psi_0(\mathbf{x}) - \psi_t(\mathbf{x}) \cos(kz) \quad (6.10)$$

$$J_e = J_0(\mathbf{x}) - \psi_t''(\mathbf{x}) \cos(kz) \quad (6.11)$$

where ψ_0 and J_0 denote respectively the magnetic flux function and the current density without the magnetic islands. ψ_t represents the contribution to the magnetic field topology caused by the tearing mode and is assumed to be small. For the simple reversal magnetic field described in chapter 5, the magnetic flux function and the current density without the magnetic islands are given by

$$\psi_0 = -\ln \cosh x \quad (6.12)$$

$$J_0 = \nabla^2 \psi_0 = -\frac{2}{\cosh^2 x} \quad (6.13)$$

The quasi-equilibrium in equations (6.10) and (6.11) describes a chain of small magnetic islands with the current density maximum at the X lines and minimum at the O-lines, as schematically shown in Figure (6.2). In comparison, the equilibrium (6.1) represents a chain of magnetic islands with the current concentrated inside the magnetic islands, as shown in Figure (6.3). The features of the magnetic island structure associated with the two equilibria have been summarized in Figure (6.4).

I chose the following particular perturbations that are expected to cause two neighboring islands to approach each other.

$$\psi_1(\mathbf{x}, kz) = \sum_{n=1}^{\infty} \tilde{\psi}_{\frac{2n-1}{2}}(\mathbf{x}) \cos\left(\frac{2n-1}{2} kz\right) \quad (6.14)$$

The above expansion is chosen so that the perturbed flux function is an even function in z and is equal to zero at the O-lines, where $kz = (2i+1)\pi$, $i = 0, \pm 1, \pm 2, \dots$. The constraint

$\psi_1 = 0$ at the X-lines, where $kz = 2i\pi$, $i = 0, \pm 1, \pm 2, \dots$, gives that

$$\sum_{n=1}^{\infty} \tilde{\psi}_{2n-1}^2(0) = 0 \quad (6.15)$$

Without loss of generality, I will only retain the first two modes, which are important ones. Neglecting the other high order harmonics, I have the trial flux function

$$\psi_1 = \tilde{\psi}_{1/2}(x) \cos(kz/2) + \tilde{\psi}_{3/2}(x) \cos(3kz/2) \quad (6.16)$$

with $\tilde{\psi}_{1/2}(0) + \tilde{\psi}_{3/2}(0) = 0$.

The driving energy for the instability comes from the gross configuration, which is able to lower its magnetic energy content so that the potential energy integral $\delta E < 0$. Using the quasi-equilibrium [equations (6.10) and (6.11)] and the coalescence perturbation [equation (6.16)], I shall divide the integral δE into two ranges of integration: one is inside the magnetic island, the other is outside the magnetic island. For the small magnetic island, the constant ψ approximation prevails and the current nonuniformity inside the magnetic island is mainly due to the formation of magnetic island (ψ_t). Outside the magnetic island, ψ_t may be neglected in comparison with the ψ_0 . Therefore, the current nonuniformity $dJ_e/d\psi_e$ associated with the potential energy can be approximated by

$$\frac{dJ_e}{d\psi_e} = \begin{cases} \frac{d(\psi_t'' \cos kz)}{d(\psi_t \cos kz)} = \frac{\psi_t''}{\psi_t} > 0 & \text{Inside the island;} \\ \frac{dJ_0}{d\psi_0} = -\frac{4}{\cosh^2 x} < 0 & \text{Outside the island.} \end{cases} \quad (6.17)$$

Using the constant ψ approximation, one can write the coalescence perturbation inside the magnetic island as

$$\psi_1 = \alpha(\cos kz/2 - \cos 3kz/2)$$

where $\alpha = \tilde{\psi}_{1/2}(0) = -\tilde{\psi}_{3/2}(0)$. The integration inside the magnetic island can be expressed

as

$$\begin{aligned}\delta E_{inside} &= \int_{<w} dx dz \left(\psi_1'^2 + \frac{\psi_t''}{\psi_t} \psi_1^2 \right) \\ &= 4\pi\alpha^2 \frac{\psi_t'}{\psi_t} \Big|_{-w}^{+w} = 4\pi\alpha^2 \Delta_t'\end{aligned}\quad (6.18)$$

where w is the width of the magnetic island and Δ_t' is a discontinuous derivative across the magnetic island. When the island width w normalized by the current thickness is much smaller than 1, it is readily found [e.g., Furth *et al.*, 1963; White, 1986] that for the small magnetic islands created by the tearing mode $\sim \cos kz$

$$\Delta_t' = \frac{\psi_t'(0+) - \psi_t'(0-)}{\psi_t(0)} = 2 \left(\frac{1}{k} - k \right) \quad (6.19)$$

Note that Δ_t' is positive for $k < 1$. Since the magnetic island configuration described by equation (6.10) is a result of an unstable tearing mode, the corresponding k should be smaller than 1 and $\Delta_t' > 0$. The above equation states that the current distribution inside the magnetic island is against the coalescence of magnetic islands.

Outside the magnetic islands, the induced magnetic field ψ_t by the tearing mode is negligible compared with the background reversal magnetic field. The m th mode $\tilde{\psi}_m \cos mkz$ has the solution [Furth *et al.*, 1963]

$$\tilde{\psi}_m(x) = \exp(\mp mkx)[1 \pm \tanh x/mk] \quad (6.20)$$

which has a discontinuous derivative across the magnetic island

$$\Delta_m' = \frac{\psi_m'(0+) - \psi_m'(0-)}{\psi_m(0)} = 2 \left(\frac{1}{mk} - mk \right) \quad (6.21)$$

The change of the potential energy outside the magnetic islands can be estimated [Furth,

1963]

$$\begin{aligned}
\delta E_{outside} &= \int_{>w} dx dz \left[(|\nabla \psi_1|^2 + \frac{dJ_0}{d\psi_0} \psi_1^2) \right] \\
&= -2\pi\alpha^2 \left[\frac{\tilde{\psi}'_{1/2}}{\tilde{\psi}_{1/2}} + \frac{\tilde{\psi}'_{3/2}}{\tilde{\psi}_{3/2}} \right]_{-w}^{+w} = -2\pi\alpha^2 (\Delta'_{1/2} + \Delta'_{3/2})
\end{aligned} \tag{6.22}$$

The total change of the potential energy

$$\begin{aligned}
\delta E &= \delta E_{inside} + \delta E_{outside} \\
&= -2\pi\alpha^2 (\Delta'_{1/2} + \Delta'_{3/2} - 2\Delta'_1) = -\frac{2\pi\alpha^2}{3k} < 0
\end{aligned} \tag{6.23}$$

The negative potential energy change implies the instability. It is clear that the chain of magnetic islands created by the tearing mode can coalesce into larger islands. The free energy for the coalescence of magnetic islands is related to the external region. The negative current distribution inside the tearing-related islands provides a positive change of the potential energy δE and thus is against the coalescence. However, the positive potential energy from the unfavorable current distribution inside the island is not strong enough to stabilize the system, in comparison with the large negative change of the potential energy from the external region.

Figure (6.6) shows the results of the magnetic island coalescence. Figure (6.6a) displays a simple island configuration created by one tearing mode. Shown in Figure (6.6b) is a plot of the current density $J_e(0, kz)$ at the center of the current sheet. The X-lines are the places with the maximum current density and the O-lines are the places with the minimum current density. Note that the current distribution in Figure (6.6b) is opposite to that in Figure (6.3). Figures (6.6c) and (6.6d) are for the flux function $\psi_1(0, kz)$ and the z component of the plasma displacement $\xi_{1z}(0, kz)$, associated with the coalescence of the two neighboring islands. The displacement inside the magnetic island is localized near the O-lines and reverses sign in the neighborhood of the X-lines in the z direction. Figure (6.6e) shows the perturbed flux surfaces. The island coalescence in the early-linear stage results in a distortion of the island configuration. As expected, the magnetic fluxes are piled up at the X-line between the two

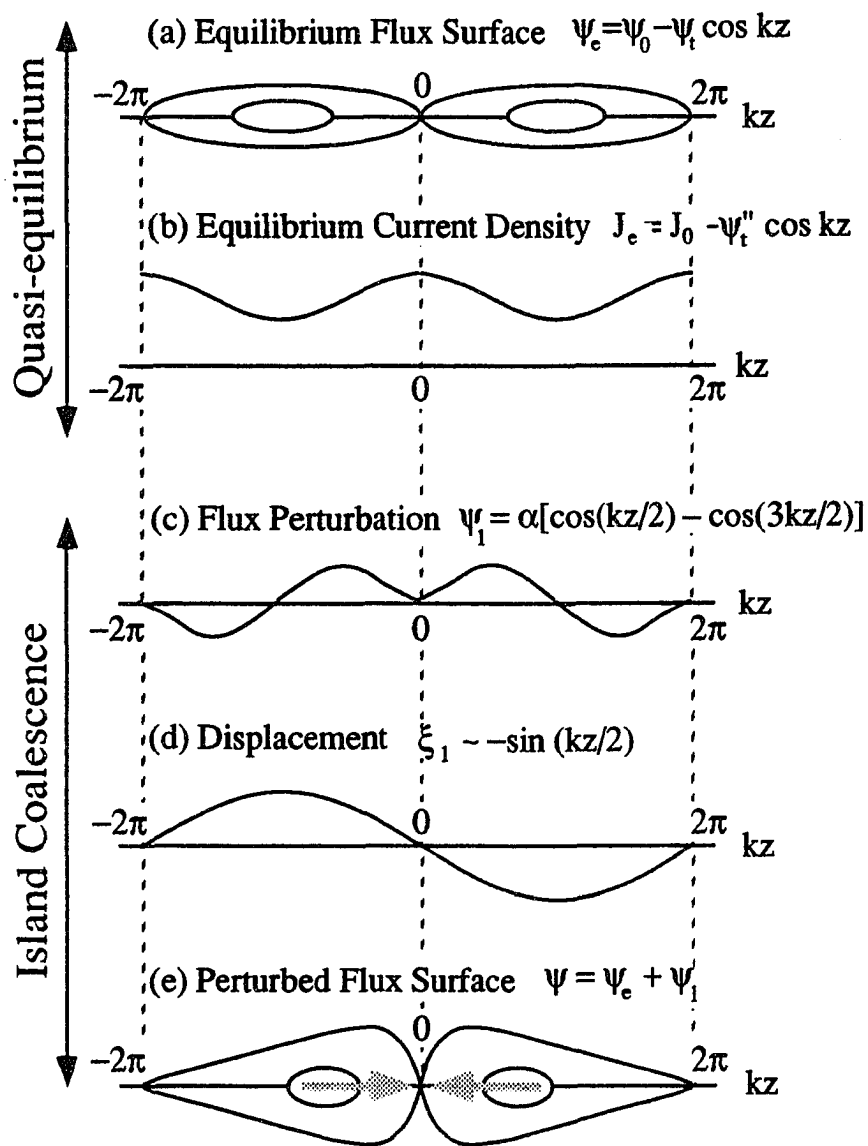


Figure 6.6 Results of the magnetic island coalescence. (a) Quasi-equilibrium flux surfaces created by the tearing mode ψ_t . (b) The current density distribution in the quasi-equilibrium. (c) The flux function perturbation ψ_1 for the island coalescence. (d) The z component of the displacement perturbation ξ_{1z} associated with the island coalescence. (e) The perturbed flux surfaces in the early stage of the island coalescence. The shaded arrow represents the plasma flow.

neighboring islands and the O-lines move toward each other. Inclusion of resistivity or electron inertia will allow the merging of the two neighboring islands into a single island. The whole coalescence process should be similar to that in Figure (6.4).

The kinetic energy integral (6.9) is determined primarily by the z component of the plasma velocity in the magnetic islands.

$$\xi_{1z} = -2 \frac{\alpha}{k\psi_t} \sin\left(\frac{kz}{2}\right) \quad (6.24)$$

$$K \simeq |\xi_1^2| \cdot w \simeq \frac{\alpha^2}{k^2\psi_t^2} \cdot w \simeq \alpha^2 k^{-2} (\psi_0'')^{-2} w^{-3} \quad (6.25)$$

where w is the width of the magnetic island as defined in Figure (6.2). For the tearing-created islands (6.10), $w = 2\sqrt{-(\psi_t/\psi_0'')}$. Thus, the growth rate for the coalescence of the magnetic islands can be estimated as

$$\gamma = \sqrt{\delta E/K} \simeq k^{1/2} |\psi_0''(0)| w^{3/2} \quad (6.26)$$

The growth rate scales as the island width to the 3/2 power and is also proportional to the current density ($J_0 = \psi_0''$) of the background reversal magnetic field.

The energy principle calculation shows that the magnetic island coalescence can occur in an island configuration created by the tearing mode and the free energy for the island coalescence is mainly from the external region. The driving force for the small island coalescence is the same as that for the tearing instability. As I have argued in the previous section, the driving force for the tearing instability is due to collapse of the magnetic field structure in the external regions; *i.e.*, the tendency of the sheet current to break up into a set of parallel pinches. It is noteworthy that the basic driving force for the tearing instability also exists in the infinite-conductivity equation and is responsible for the coalescence of the small magnetic islands. The difference between the tearing and the island coalescence lies in the mechanism by which the magnetic flux is swept into the magnetic islands. The tearing instability depends

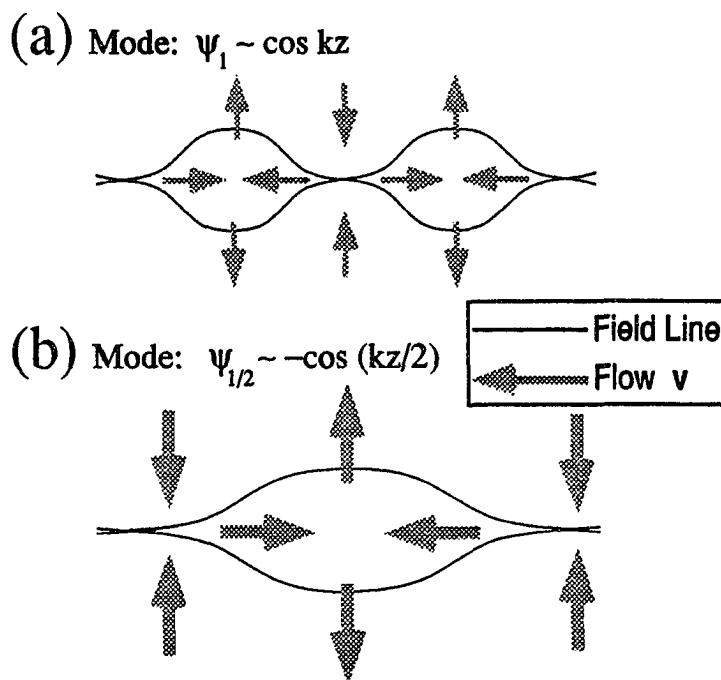


Figure 6.7 Magnetic islands and flow patterns associated with $\psi_t \sim -\cos kz$ and $\tilde{\psi}_{1/2} \sim \cos kz/2$ tearing modes.

on the finite resistivity or the electron inertia to relax the system, while the existence of the B_x component associated with the magnetic islands allows the plasma flow freely across the magnetic field lines into the islands. The mechanism for the coalescence of tearing-created small islands is also different from that of the coalescence instabilities described in the previous section. The coalescence instability is due to the attraction of parallel current lines associated with the magnetic O-lines, while the coalescence of the tearing-created islands can be attributed more to the mode-mode coupling. Figure (6.7) schematically shows the magnetic islands and flow patterns produced by two unstable tearing modes ($\psi_t \sim -\cos kz$ and $\tilde{\psi}_{1/2} \sim \cos kz/2$ modes). When the magnetic field in the external region collapses to form the flow pattern of the $\tilde{\psi}_{1/2}$ mode (long wavelength) as shown in the upper panel, the plasma flow of $\tilde{\psi}_{1/2}$ mode can push the two preexisting islands of ψ_t mode towards each other. Different from

the coalescence instability that is driven by the current attraction force between two adjacent islands, the coalescence of the ψ_t mode islands is due to the driven flow provided by the $\tilde{\psi}_{1/2}$ mode and thus has no prerequisite for the current filaments at the O-lines.

6.4 Discussion and Summary

By an energy principle calculation I have shown that a chain of small magnetic islands created by the tearing mode is unstable to an ideal hydromagnetic perturbation that corresponds to a tendency toward coalescence of two neighboring islands. I have emphasized the differences of the physical mechanisms among the tearing instability, the coalescence instability and the instability that leads to the coalescence of the tearing-generated islands. The tearing instability is caused by the collapse of the current sheet, and the current filaments are the result of the current sheet pinching at the X-lines. The coalescence instability, based on the preexisting current filaments inside the magnetic island, results from the current line attraction between two neighboring islands. The coalescence of the tearing-created small islands is mainly due to the mode-mode coupling.

In the simulation studies of the collisionless tearing instabilities, the nonlinear development of tearing instability by the island coalescence has been frequently observed. With the initial thermal noise, the most unstable tearing modes grow above the thermal level corresponding to the linear growth rate. The tearing mode usually evolves into a nonlinear stage in an early time, then follows a rapid coalescence of the small magnetic islands, a result consistent with our theory in section (6.3). In a number of simulations and experiments [Katanuma and Kamimura, 1980; Hewett *et al.*, 1988; Gekelman and Pfister, 1988], however, the current filaments are observed to move from X-line in the early stage of tearing mode to the O-line, resulting in the current concentration inside the magnetic islands. The magnetic island then continues to

grow exceeding the current sheet thickness and the coalescence of the large magnetic islands occurs due to the current line attraction according to the discussion in section (6.2).

In contrast with the particle simulations, the MHD simulations have shown no indication, for the case of random initial conditions, that the magnetic configuration is ever dominated by chains of multiple islands, which later coalesce. Neither have the MHD simulations shown any trend of nonlinear tearing evolution that may be favorable for the coalescence instability. Instead, the position of the current maximum remains relatively fixed, and is the nominal X-line during the evolution of the nonlinear tearing mode. The magnetic island is further stretched in the tearing layer, which leads to a long and thin current layer near X-lines. Under some favorable conditions, the long current layer near X-lines could lead to a secondary tearing and generate a new magnetic island centered at the initial X-line [Steinolfson and Hoven, 1984; Scholer and Roth, 1987; Matthaeus, 1985].

The lack of the magnetic island coalescence in MHD was explained by Bondeson [1983] as due to the invisibility of a small island, which is of the size of the tearing layer. The growth rate for the island coalescence is proportional to $w^{3/2}$, where w is the island width. This growth rate for the island coalescence is the same as the dependence of the resistive tearing mode growth rate on the tearing width x_t , $\gamma \sim x_t^{3/2}$ [Furth *et al.*, 1963]. Thus, if the island chain originally results from a short-wavelength tearing mode, the island coalescence should have a growth rate comparable to the tearing mode, when the island width is of the order of the tearing width. An increase in island size decreases the growth rate of the tearing mode, but increases that for the island coalescence. Consequently, the evolution of a tearing unstable equilibrium with random, small-amplitude perturbations can hardly lead to magnetic islands of less than the maximum periodic length, wider than a few tearing widths, before coalescence into larger islands would take place. This seems to explain the observation in the resistive MHD simulations that islands due to high-wavenumber tearing modes did not usually occur

in a multiple-mode resistive MHD simulation with random small perturbations. An island of the size of the tearing layer would not be visible on a normal field line plot. However, for the large amplitude fluctuations, the island coalescence can be observed in an early stage of the tearing instability, as Matthaeus [1985] demonstrated in his the resistive MHD simulation.

In order for the large magnetic island to be unstable to coalescence perturbations, somehow the current filament at an X-line must move to the vicinity of the O-lines during the saturated state of the tearing mode, so that the stretched magnetic islands in the tearing mode become much thicker producing more favorable conditions for the coalescence instability by the current line attraction. In a collisionless plasma, the cause of the current filamentation in the linear phase is the acceleration of electrons by the induced electric field. The nonlinear growth phase occurs when the initial current changes its profile and becomes diffuse. After the magnetic island has grown to some degree, the electrons in the tearing layer become trapped in the magnetic island and are not accelerated when the electron bounce frequency is nearly equal to the growth rate of the instability. In this phase, the induced electric field will lead to the $\mathbf{E} \times \mathbf{B}$ drift of the electrons into the final O-line through the X-line, and the current does not even occupy the same volume as the electric field. Thus, the electrons that carry the current move away from the X-lines, and subsequent currents may flow near the O-lines so that the coalescence instability will be triggered. Since the current filaments are not frozen in the plasma, the flow moving from the X-line to the O-line in a resistive plasma is not expected to carry away the current filaments at the X-lines. Instead, the current filament is always associated with the induced electric field at the X-line, where $\mathbf{B} = 0$ and $\mathbf{E} = \eta\mathbf{J}$. When the induced electric field continues to increase, the current sheet at the X-line will become so thin that the small magnetic island can be generated due to the short-wavelength tearing mode.

Our results and discussions may shed some light on the nonlinear development of the tearing mode in terms of the island coalescence, and clarify some misleading conceptions.

However, most of our arguments are primitive, and they should be carried out in further studies. The quasi-equilibrium and the constant ψ approximation in the previous section are valid for the small magnetic island configuration, in which the tearing layer should be much thinner than the current sheet thickness. Thus, our results may not be applicable for some devices or magnetic configurations in which the current sheet thickness is comparable to the tearing layer width. I have shown that for the thick current sheet the small island coalescence can occur and the current density is concentrated along the separatrix surface as depicted in Figure (6.2). In the collisionless plasma, the tearing layer is expected to be comparable to the current thickness when the electron inertia length or electron gyroradius is of order of the current sheet thickness. For such a thin current sheet, the constant ψ approximation is not applicable and the island created by the tearing instability can continue growth over the current sheet thickness. At this point, the large islands, within which the current density is concentrated, can form because of the current filaments moving from the X lines to the O-lines. These large islands then coalesce due to the current line attraction as shown in the particle simulation and experiments [Katanuma and Kamimura, 1980; Hewett *et al.*, 1988; Gekelman and Pfister, 1988].

CHAPTER 7

Discussions and Conclusions

The magnetosphere-ionosphere (M-I) coupling, as part of the solar-terrestrial interactive system, has developed toward the stage of quantitative understanding. The M-I coupling model is evolving from studying local effects to global synthesis. An attempt is made in this thesis to address several unsolved issues and provide some insight into the physical mechanism in magnetosphere-ionosphere coupling processes. I have investigated in detail the five specific topics described in Chapters 2, 3, 4, 5 and 6. The considerations of these topics are given as if in isolation from each other, but these physical processes are integral parts of the M-I coupling process.

Figure 7.1 shows a schematic view of the magnetosphere and a summary diagram. Each solid box in the summary diagram represents one research topic studied in this thesis with the number indicating the chapter number. The arrows indicate the relationships of these topics to the M-I coupling process.

Solar wind energy can enter the magnetosphere by reconnection processes to establish the magnetospheric convection. The plasma motion in the magnetosphere is line-tied by the conducting ionosphere and is intimately coupled with the ionosphere by waves, field-aligned currents and parallel electric fields. As shown in the summary diagram of Figure 7.1, the three-dimensional tearing model in Chapter 5 provides a basic mechanism for initiating the patchy and intermittent reconnection at the dayside magnetopause. As the tearing instability fully develops in a nonlinear stage, a significant magnetic flux can reconnect to induce the large magnetospheric convection. The study of magnetic island coalescence in Chapter 6 is important for the nonlinear tearing and fast magnetic reconnection theories. The enhanced

Schematic View of the Magnetosphere

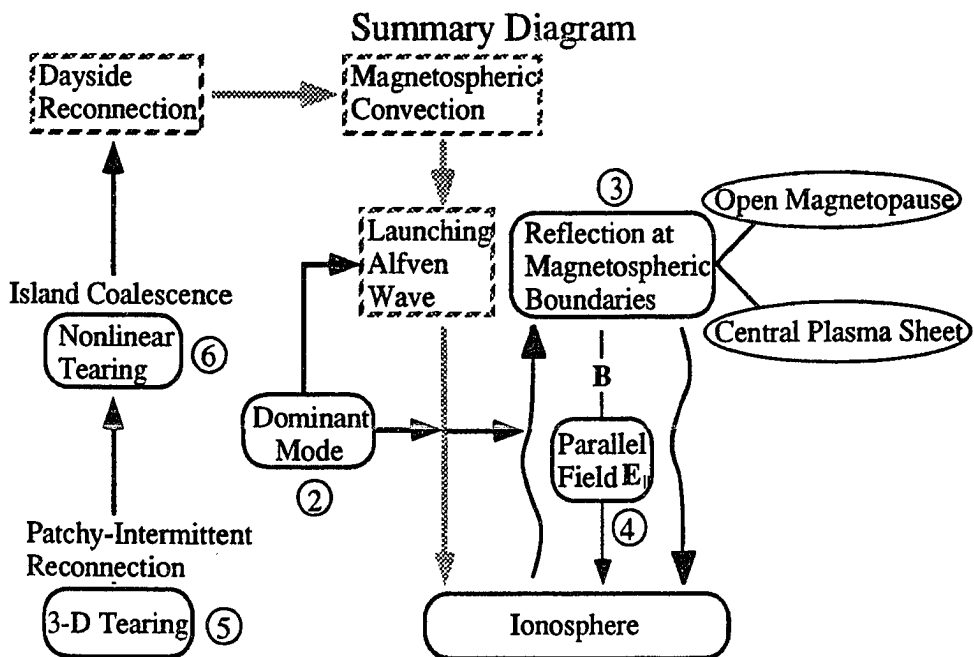
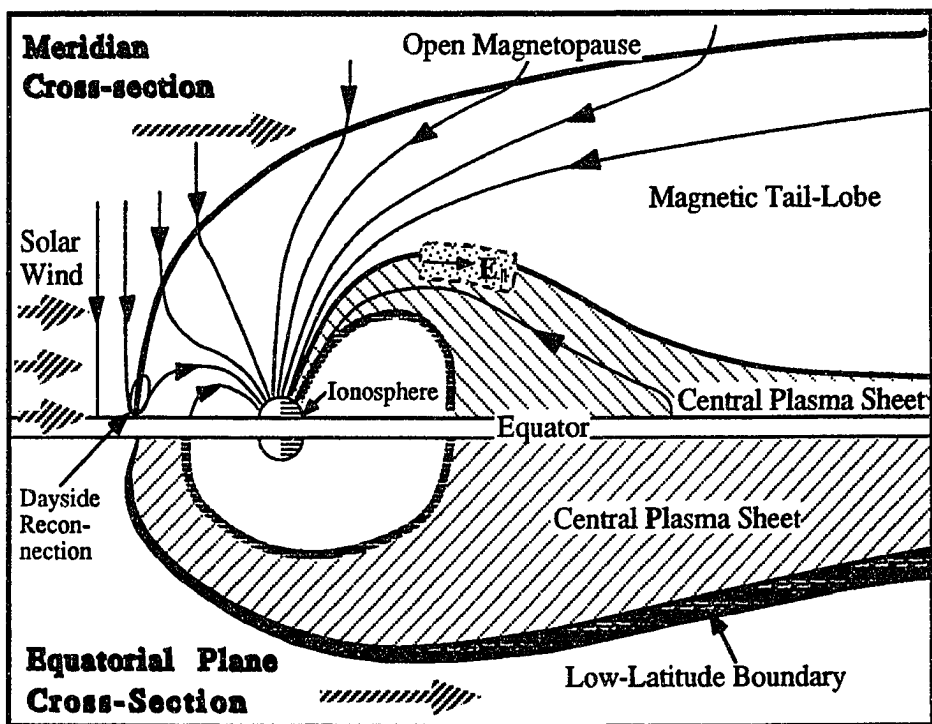


Figure 7.1 Schematic view of the magnetosphere and the summary diagram of research domains.

magnetospheric convection due to the dayside magnetic reconnection must propagate toward the ionosphere by the hydromagnetic waves. The study in Chapter 2 serves as a purpose to determine which wave mode is the dominant one in magnetosphere-ionosphere coupling processes. The dynamic M-I coupling may well be modeled by the Alfvén wave bouncing between the magnetosphere and ionosphere. The study in Chapter 3 determines the reflection of Alfvén waves at the magnetospheric source regions. As the Alfvén waves propagate back and forth along the magnetic field lines, the field-aligned currents are established to link the magnetosphere and ionosphere. The increasing field-aligned current can lead to an enhancement of ionospheric conductances and a parallel potential drop along the magnetic field lines. The study in Chapter 4 describes the relationship among the field-aligned current, parallel potential drop, ionospheric conductance and convection.

The results in chapter 2 indicate that the group velocity of Alfvén waves is well guided along the magnetic field lines and the shear stress in the Alfvén waves associates with a large field-aligned current. It can be concluded that the Alfvén wave mode plays a major role in the time-dependent M-I coupling, even in the auroral arc scale length. The long-wavelength Alfvén wave is incompressible, so that the energy can be transmitted by the Alfvén wave without large-scale exchanges of the fluid elements. In the auroral arc scale length, however, the Alfvén wave becomes compressible due to the finite ion inertial length or ion gyroradius effects and may interact strongly with the surrounding plasma.

Reflection of Alfvén waves at the magnetospheric source regions depends mainly on the plasma density and the magnetic field jumps across the source regions. Across the open magnetopause, which separates the solar wind and the magnetospheric plasma, the plasma density in the solar wind is much larger than that in the magnetosphere so that a large portion of incident wave electric field will be reflected due to the large solar wind inertia. The existence of the current sheets at the open magnetopause and at the plasma sheet results in a significant

bending of the magnetic field lines. The bending of the magnetic field lines can couple the incompressible Alfvén waves to the compressional waves, resulting in the partial reflection of Alfvén waves. The study in chapter 3 shows that the amplitude reflection coefficient of the Alfvén wave electric field can range from 0.8 to -1 at the open magnetopause and the open magnetopause may be viewed as a constant voltage source. Reflection of the Alfvén waves at the plasma sheet depends on which portion of the plasma sheet is considered and the amplitude reflection coefficient may be extended to a wide range from 0 to -1 . In the near-earth plasma sheet where the curvature of magnetic field lines is weak, the incident Alfvén wave from the ionosphere can propagate across the plasma sheet almost without reflection. In the magnetotail region, however, the incident Alfvén wave negotiating a strong curvature of field lines can result in the total reflection.

As the field-aligned current builds up by the bouncing Alfvén waves, the potential drop along the magnetic field lines is expected to develop. It is pointed out in chapter 4 that the generation of field-aligned potential drops will filter the small scale magnetospheric field out of the ionospheric field, while large scale fields are fully impressed on the ionosphere. The existence of the field-aligned potential can smooth out and distort the intermediate-scale magnetospheric structures, such as the convection reversals and Harang discontinuity. The upward field-aligned current may also be significantly limited due to the additional loading of field-aligned potentials. The field-aligned potential drop is powered by the magnetospheric energy source, which is assumed in chapter 4 to be either a constant voltage or a constant current source. The difference between the constant current and voltage generators lies on their ability to adjust the vorticity of the magnetospheric convection. It is found that the constant current generator can adjust the vorticity of the magnetospheric convection to support a larger field-aligned current and to make a more significant distortion of the ionospheric convection pattern than the constant voltage generator.

The magnetic reconnection at the dayside magnetopause is responsible for setting up the magnetospheric convection and providing energy to the dynamic magnetosphere-ionosphere coupling processes. There exists ample evidence that the dayside magnetic reconnection is patchy and intermittent. The study in chapter 5 of the tearing instability of a thin current sheet may provide a possible mechanism for the patchy and intermittent nature of the dayside magnetic reconnection. As the current sheet thickness is comparable to the ion inertial length, the finite-ion-inertial-length (FIIL) effect becomes very important in the resistive tearing instability. Compared with the resistive MHD tearing without the FIIL effect, the oblique tearing of a thin current sheet may become unstable over a wide range of wave normal angles with respect to the field direction and has finite phase velocities. The three-dimensional tearing produced by the oblique wave packet displays a finite magnetic island structure consistent with the observed FTE signatures. The FIIL effect associated with the thin current sheet increases the patchiness of the dayside reconnection and may also provide a possible explanation of the intermittent nature for the dayside magnetic reconnection.

The purpose of chapter 6 is to discuss the possibility of nonlinear tearing evolution in terms of magnetic island coalescence and to solve the puzzles related to the tearing and coalescence instabilities. It is shown that the small magnetic islands created by the tearing mode during its nonlinear saturation stage are unstable and intend to coalesce into the large ones. The mechanism for the coalescence of tearing-created small islands is due to the mode-mode coupling, which is quite different from those of tearing and coalescence instabilities. The tearing instability is a result of combined effects of the external current sheet collapse and the internal dissipating processes, which can result in relative motion of the field lines with respect to the plasma. The coalescence instability is a natural consequence of the attraction among the preexisting current filaments. It is noted that the nonlinear tearing development in the resistive MHD simulations is quite unlike that in the particle simulations. In the resistive

MHD simulations, the stretched magnetic islands with current filaments at X lines are the peculiar features of the nonlinear tearing. In the particle simulations, the island coalescence seems to be a natural consequence of the nonlinear tearing development. It is argued that there exist two distinguishable physical mechanisms for the island coalescence in the particle simulations, depending on the current sheet thickness. For the thick current sheet, whose thickness is much larger than the tearing layer width, the small island coalescence occurs due to the mode-mode coupling and the current density is concentrated along the separatrix surface. For the thin current sheet, whose thickness is comparable to the tearing layer width, the large magnetic islands can form with the current filaments moving from the X lines to the O lines and then coalesce due to the current line attraction.

As indicated by the shaded boxes and arrows in the summary diagram of Figure 7.1, it is not clear quantitatively what is the relationship between the patchy reconnection and M-I coupling by the Alfvén wave. However, I shall outline qualitatively how the change in the dayside magnetopause boundary conditions following the patchy reconnection can communicate by the Alfvén wave to the rest of the magnetosphere and ionosphere.

As the magnetic field lines reconnect in the dayside magnetopause, a disruption of the current sheet should arise. The current disruption is accompanied by the generation of the MHD waves. These waves may propagate, interfere and essentially affect the whole plasma flow and magnetic field pattern. The Alfvén wave should be of great importance, since it produces closure currents that consist of the field-aligned currents, connected to the disrupted magnetopause current sheet, and polarization currents at the fronts of the Alfvén waves. Thus, the Alfvén wave, carrying the information of change at the magnetopause, propagates down newly opened field lines from the reconnection region to the ionosphere, where it is partially reflected. The reflected wave then propagates back up the field line to the magnetopause. This reflection process continues, until the local ionospheric electric field reaches a value consistent

with the modified reconnection potential. The characteristic of the patchy and intermittent reconnection is the isolation of the reconnected flux tubes known as FTEs, which have a dimension of one or two R_E . The enhanced connection channel in the reconnected flux tube determines the initial field pattern of the Alfvén wave, which propagates to the ionosphere and may produce an electric field spike as an FTE footage (~ 100 km) in the ionosphere.

In summary, the study in this thesis has indicated that the Alfvén wave is the dominant mode in transmitting energy and field-aligned currents. Both the ionosphere and the magnetospheric boundaries can serve as the good reflectors to the Alfvén wave. Therefore, dynamic M-I coupling can be modeled by the Alfvén wave bouncing between the ionosphere and the magnetospheric boundaries. The ionosphere acts as a reflector because of the large ionospheric conductance. The open magnetopause boundary behaves like a near perfect reflector to the Alfvén wave because of the large solar wind inertia. Reflection of the Alfvén wave on the closed field lines in the plasma sheet is due to the strong curvature of increasingly distended field lines in the magnetotail. As the Alfvén wave propagates back and forth between the ionosphere and the magnetospheric boundaries, the increasingly field-aligned current can cause the field-aligned potential drops, which subsequently limit the further increase of the upward field-aligned current. The patchy and intermittent reconnection, initiated by the 3-D tearing instability at the dayside magnetopause can lead to the isolated magnetic flux tubes. The change of magnetic stresses in the dayside magnetopause following the patchy and intermittent reconnection provides the ultimate source for the Alfvén waves, which communicate from then on to the rest of the magnetosphere and ionosphere.

In this thesis, I have considered the five pressing issues related to the magnetosphere-ionosphere (M-I) coupling processes. I feel that considerable progress has been made in understanding the M-I coupling. Nonetheless, significant uncertainty remains. Further effort

has to be made to integrate these basic elements into a single global model to advance our understanding of the dynamic magnetosphere-ionosphere coupling processes.

APPENDIX A

Two-Fluid Equations and Dispersion Relation

The purpose of this appendix is to derive the dispersion relation for linear waves of all frequencies in a warm two-fluid plasma. Without loss of generality, the linearized two-fluid equations [e.g., Krall and Trivelpiece, 1973] can be combined into the one-fluid equations

$$\frac{\partial \rho}{\partial t} + \rho_0 \nabla \cdot \mathbf{V} = 0 \quad (A1)$$

$$\rho_0 \frac{d\mathbf{V}}{dt} = -\nabla p + \frac{1}{c} \mathbf{J} \times \mathbf{B}_0 \quad (A2)$$

$$\frac{\partial p}{\partial t} + \rho_0 C_s^2 \nabla \cdot \mathbf{V} - \frac{\gamma_e T_e}{e} \nabla \cdot \mathbf{J} = 0 \quad (A3)$$

$$\frac{\partial}{\partial t} \left[\frac{m_e}{n_0 e^2} \frac{\partial \mathbf{J}}{\partial t} - \mathbf{E} - \frac{1}{c} \mathbf{V} \times \mathbf{B}_0 + \frac{1}{n_0 e c} \mathbf{J} \times \mathbf{B}_0 - \frac{1}{n_0 e} \frac{\gamma_e T_e}{\gamma_e T_e + \gamma_i T_i} \nabla p \right] = a^2 \nabla (\nabla \cdot \mathbf{J}) \quad (A4)$$

where $p = p_e + p_i$, $\mathbf{J} = n_0 e (\mathbf{V}_i - \mathbf{V}_e)$, $\rho = m_i n_i + m_e n_e$, $\mathbf{V} = (m_i \mathbf{V}_i + m_e \mathbf{V}_e) / (m_i + m_e)$, $C_s^2 = (\gamma_i T_i + \gamma_e T_e) / m_i$, and $a^2 = [\gamma_i T_i / (\gamma_e T_e + \gamma_i T_i)] \cdot [\gamma_e T_e / (n_0 e^2)]$. Equations (A1) through (A4) are equivalent to the two-fluid equations except m_e / m_i terms have been neglected compared with unity.

The $\nabla \cdot \mathbf{J}$ terms in equations (A3) and (A4) are due to the effects associated with the charge separation and are important only when the wavelength is comparable to the plasma Debye length. Under the quasi-neutrality approximation, the $\nabla \cdot \mathbf{J}$ terms in equations (A3) and (A4) can be neglected, and equations (A1)-(A4) are reduced to the usual one-fluid equations. The first term on the left side of equation (A4) represents the electron inertial effect. With the quasi-neutrality and incompressible approximations and neglecting the electron inertia, equations (A1)-(A4) are reduced to those in chapter 5 as given in equations (6.1)-(6.4).

Combining (A1)-(A4) with the Maxwell's equations, one obtains

$$\vec{D} \cdot \mathbf{J} = 0 \quad (\text{A5})$$

where

$$\begin{aligned} D_{11} &= -\frac{V_A^2}{c^2} \sin^2 \theta - 1 + \frac{\omega^2 (1 - k^2 C_e^2 / \omega^2)(1 - k^2 C_i^2 / \omega^2)}{\omega_{pe}^2 (1 - k^2 C_s^2 / \omega^2)} \\ D_{12} &= D_{21} / (k^2 c^2 / \omega^2 - 1) = i \frac{V_A^2}{c^2} \frac{\omega}{\Omega_i} \frac{1 - k^2 C_i^2 / \omega^2}{1 - k^2 C_s^2 / \omega^2} \sin \theta \\ D_{13} &= -i D_{31} (k^2 c^2 / \omega^2 - 1) = \frac{V_A^2}{c^2} \sin \theta \cos \theta \\ D_{22} &= \left[-\left(\frac{k^2 c^2}{\omega_{pe}^2} + 1 \right) + \left(1 - \frac{\omega^2}{k^2 c^2} \right) \frac{k^2 V_A^2}{\omega^2} \frac{1 - k^2 C_s^2 \cos^2 \theta / \omega^2}{1 - k^2 C_s^2 / \omega^2} \right] \left(1 - \frac{\omega^2}{k^2 c^2} \right) \\ D_{23} &= -D_{32} = -i \left(1 - \frac{\omega^2}{k^2 c^2} \right) \frac{k^2 V_A^2}{\omega^2} \frac{\omega}{\Omega_i} \cos \theta \\ D_{33} &= -\left(\frac{k^2 c^2}{\omega_{pe}^2} + 1 \right) + \left(1 - \frac{\omega^2}{k^2 c^2} \right) \frac{k^2 V_A^2}{\omega^2} \cos^2 \theta \end{aligned}$$

The constants are defined as

$$C_s^2 = \frac{\gamma_e T_e + \gamma_i T_i}{m_i} \quad C_i^2 = \frac{\gamma_i T_i}{m_i} \quad C_e^2 = \frac{\gamma_e T_e}{m_e} \quad V_A^2 = \frac{B_0^2}{4\pi\rho_0} \quad \omega_{pe}^2 = \frac{4\pi n_0 e^2}{m_e}$$

where C_s is the sound speed, C_i is the ion thermal speed, C_e is the electron thermal speed, V_A is the Alfvén speed and ω_{pe} is the plasma frequency. The above equations are derived in a coordinate system in which $\mathbf{k} = (k, 0, 0)$, $\mathbf{B}_0 = (B_0 \cos \theta, 0, B_0 \sin \theta)$, $\mathbf{E} = (E_p \cos \phi, E_\perp, -E_p \sin \phi)$. E_p is the component of \mathbf{E} in the \mathbf{k} - \mathbf{B}_0 plane and E_\perp is the component perpendicular to the \mathbf{k} - \mathbf{B}_0 plane. θ is the angle between the wavevector \mathbf{k} and the background magnetic field \mathbf{B}_0 . The angle ϕ is between \mathbf{k} and \mathbf{E}_p .

The general dispersion relation is given by

$$\det |\vec{D}| = 0 \quad (\text{A6})$$

which is valid for linear waves of any frequency and any wavelength in a warm two-fluid plasma.

For low-frequency ($\omega \ll \omega_{pi}$) and long wavelength ($k\lambda_e \ll 1$) waves, the terms $(\omega/kc)^2$ and V^2/c^2 can be neglected. In this case, the quasi-neutrality condition holds so that $\nabla \cdot \mathbf{J} = 0$. Under these conditions, the general dispersion relation reduces to that of Stringer [1963] and Formisano and Kennel [1969] as given in (2.12) of chapter 2. $D_{11} = 0$ is the general dispersion relation of the electric static waves as given by Stringer [1963].

APPENDIX B

Numerical Scheme for the Initial Value Problem

The purpose of this appendix is to present the numerical scheme for solving the linearized equations in chapter 5, which describes the oblique resistive tearing of a thin current sheet. For convenience, the dimensionless governing equations (5.7)-(5.10) in chapter 5 are rewritten as follows

$$\frac{\partial}{\partial \tau} \psi_X = S^{-1} \nabla^2 \psi_X - F W_X - h \alpha^2 \left(F \psi_Y + i \frac{\tan \theta}{\alpha} F' \psi_X \right) \quad (B1)$$

$$\frac{1}{\alpha^2} \frac{\partial}{\partial \tau} \nabla^2 W_X = F \nabla^2 \psi_X - F'' \psi_X \quad (B2)$$

$$\frac{\partial}{\partial \tau} \psi_Y = S^{-1} \nabla^2 \psi_Y - F W_Y + i \frac{\tan \theta}{\alpha} F' W_X - h (F \nabla^2 \psi_X - F'' \psi_X) \quad (B3)$$

$$\frac{1}{\alpha^2} \frac{\partial}{\partial \tau} W_Y = F \psi_Y + i \frac{\tan \theta}{\alpha} F' \psi_X \quad (B4)$$

where the Laplace operator $\nabla^2 = \partial^2 / \partial x^2 - \alpha^2$ and the normalized perturbed quantities are defined as

$$\psi_X = B_{X1} / B_{z0}, \quad W_X = -i V_{X1} k \tau_A,$$

$$\psi_Y = B_{Y1} / B_{z0}, \quad W_Y = -i V_{Y1} k \tau_A,$$

$$F = \mathbf{k} \cdot \mathbf{B}_0(\mathbf{x}) / k B_{z0}, \quad k = \sqrt{k_z^2 + k_y^2},$$

$$\alpha = k \Delta, \quad \tau_R = 4\pi \Delta^2 / (c^2 \eta), \quad \tau_A = \Delta \sqrt{4\pi \rho_0} / B_{z0},$$

$$S = \tau_R / \tau_A, \quad h = c \sqrt{m_i / (4\pi n_0 e^2)} / \Delta$$

We wish to solve the above linear equations as an initial value problem. The equations (B1)-(B4) are the diffusion-type parabolic equations that have a simple form in one space dimension,

$$\frac{\partial u}{\partial t} = D \frac{\partial^2 u}{\partial x^2} \quad (B5)$$

Let u_j^n denotes the numerical approximation to u value at the grid point j and time step n .

The diffusion equation (B5) can be differenced by a Crank-Nicholson scheme.

$$\frac{u_j^{n+1} - u_j^n}{\Delta t} = \frac{D}{2} \left[\frac{(u_{j+1}^{n+1} - 2u_j^{n+1} + u_{j-1}^{n+1}) + (u_{j+1}^n - 2u_j^n + u_{j-1}^n)}{(\Delta x)^2} \right] \quad (B6)$$

Here the Crank-Nicholson scheme combines the stability of an implicit method with the accuracy of a method that is second-order in both space and time. Both the left and right hand sides in (B6) are centered at time step $n + 1/2$, so the method is second-order accurate in time as claimed. The usual second divided difference of u $[(\delta^2 u)_j = (u_{j+1}^n - 2u_j^n + u_{j-1}^n)/(\Delta x)^2]$ is also second-order accurate in space. The resulting difference equation is implicit and is unconditionally stable for any size Δt .

Now generalize Crank-Nicholson scheme for the simple diffusion equation (B5) to our governing equations (B1)-(B4). In order to keep the second order accuracy in both the time and space, the functions ψ and W are evaluated as the average of the time steps n and $n + 1$, e.g., $\psi = (\psi_j^{n+1} + \psi_j^n)/2$. The first term in equation (B2), which is evolved with the first derivative in time and the second derivative in space, can be discretized to second order by an analogue that takes the form

$$\frac{1}{\alpha^2 \Delta \tau} \left[\frac{(W_x)_{j+1}^{n+1} - 2(W_x)_j^{n+1} + (W_x)_{j-1}^{n+1}}{(\Delta x)^2} - \alpha^2 (W_x)_j^{n+1} \right. \\ \left. - \frac{(W_x)_{j+1}^n - 2(W_x)_j^n + (W_x)_{j-1}^n}{(\Delta x)^2} - \alpha^2 (W_x)_j^n \right] \quad (B7)$$

The implicit nature of the difference scheme involves solving the linear equations at each time step. After discretized by the Crank-Nicholson scheme, the difference equations corresponding to (B1)-(B4) can be expressed as

$$-A_j \mathbf{u}_{j+1}^{n+1} + B_j \mathbf{u}_j^{n+1} - C_j \mathbf{u}_{j-1}^{n+1} = \mathbf{d}^n \quad (B8)$$

where the vector $\mathbf{u}_j^{n+1} = [(\psi_x)_j^{n+1}, (W_x)_j^{n+1}, (\psi_y)_j^{n+1}, (W_y)_j^{n+1}]$ denotes the unknown variables in time step $(n+1)\Delta\tau$ and at the grid point $j\Delta x$, the vector \mathbf{d}^n contains the known values of the variables at the time step $n\Delta\tau$. A , B and C are the coefficient matrixes, none of which vary in time. The resulting difference equations (B8) are implicit. At each time step, one must solve a linear system for unknowns \mathbf{u} .

Since we are interested in the infinite domain $(-\infty \leq x \leq \infty)$, then for the finite difference domain we take $-x_{max} \leq x \leq x_{max}$. In our calculation, the boundaries are set at ten times the current sheet thickness Δ ($x_{max}/\Delta = 10$), and the finite domain is divided into M grid points ($j = 1, 2, \dots, M-1, M$). The imposed boundary conditions are given as following

$$\frac{\partial \mathbf{u}}{\partial x} - \alpha \mathbf{u} = 0 \quad \text{at } x = -x_{max} \\ \frac{\partial \mathbf{u}}{\partial x} + \alpha \mathbf{u} = 0 \quad \text{at } x = +x_{max} \quad (B9)$$

where the vector \mathbf{u} stands for the four variables as previously defined. The above boundary conditions can be discretized to the first order accuracy

$$\begin{aligned}
 \mathbf{u}_1 &= \frac{1}{1 + \alpha \Delta x} \mathbf{u}_2 & \text{at } x = -x_{max} \\
 \mathbf{u}_{M-1} &= \mathbf{u}_M (1 + \alpha \Delta x) & \text{at } x = +x_{max}
 \end{aligned}
 \tag{B10}$$

With an initial arbitrary perturbation \mathbf{u}^0 , the linear system of equations (B8) combined with the boundary conditions (B10) are then solved by the block tridiagonal method to advance the time integral. For an unstable current sheet, the fastest growing mode in the plane wave assumption $\exp(\nu t - i\omega t)$ will dominate the numerical solution as time progresses. The complex frequency with the growth rate μ and real frequency ω is calculated at each grid point by using

$$\nu - i\omega = \frac{\partial}{\partial t} \ln A = \frac{2}{\Delta t} \frac{A_j^{n+1} - A_j^n}{A_j^{n+1} + A_j^n}
 \tag{B11}$$

where A stands for any variable of ψ and W . The program is terminated when the growth rate converges over the entire domain to four figures.

REFERENCES

- Alfvén, H., 1942, Existence of electromagnetic-hydrodynamic waves, *Nature*, *150*, 405.
- Alfvén, H., and C. G. Fälthammar, *Cosmical Electrodynamics, Fundamental Principles*, Clarendon, Oxford, 1963.
- Ambrosiano, J., L. C. Lee, and Z. F. Fu, Simulation of the collisionless tearing instability in an anisotropic neutral sheet, *J. Geophys. Res.*, *91*, 113, 1986.
- Atkinson, G., A mathematical model of convection with distributed Birkeland currents, *J. Geophys. Res.*, *91*, 5831, 1986.
- Barbosa, D. D., Polar convection patterns under quiet conditions, *J. Geophys. Res.*, *90*, 9711, 1985.
- Barnes, A., Collisionless damping of hydromagnetic waves, *Phys. Fluids*, *9*, 1483, 1966.
- Berchem, J., and C. T. Russell, Magnetic field rotation through the magnetopause: ISEE 1 and 2 observations, *J. Geophys. Res.*, *87*, 8139, 1982a.
- Berchem, J. and C. T. Russell, The thickness of the magnetopause current layer: ISEE 1 and 2 observations, *J. Geophys. Res.*, *87*, 2108, 1982b.
- Berchem, J., and C. T. Russell, Flux transfer events on the magnetopause: Spatial distribution and controlling factors, *J. Geophys. Res.*, *89*, 6689, 1984.
- Bernstein, I. B., E. A. Frieman, M. D. Kruskal and R. M. Kulsrud, An energy principle for hydromagnetic stability problems, *Proc. Roy. Soc. (London)*, *A244*, 17, 1958.
- Bhattacharjee, A. F. Brunel, and T. Tajima, Magnetic reconnection driven by the coalescence instability, *Phys. Fluids*, *26*, 3332, 1983.
- Biskamp, D., Effect of secondary tearing instability on the coalescence of magnetic islands, *Phys. Lett.* *87A*, 357, 1982.
- Biskamp D., and H. Welter, Coalescence of magnetic islands, *Phys. Rev. Lett.* *44*, 1069, 1980.
- Biskamp, D., and K. Schindler, Instability of two-dimensional collisionless plasmas with neutral points, *Plasma Physics*, *11*, 1013, 1971.
- Bondeson, A., Linear analysis of the coalescence instability, *Phys. Fluids*, *26*, 1275, 1983.

- Böström, R., Mechanisms for driving Birkeland currents, in *Physics of the Hot Plasma in the Magnetosphere*, edited by B. Hultqvist and L. Stenflo, P. 341, Plenum, New York, 1975.
- Budden, K. G., *The Propagation of Radio Waves: the theory of radio waves of low power in the ionosphere and magnetosphere*, Cambridge University Press, 1985.
- Cao, F., and J. R. Kan, Finite-Larmor-radius effect on field-aligned currents in hydromagnetic waves, *J. Geophys. Res.*, *92*, 3397, 1987.
- Cao, F., and J. R. Kan, Reflection of Alfvén waves at an open magnetopause, *J. Geophys. Res.*, *95*, 4257, 1990.
- Cao, F., and J. R. Kan, Oblique tearing of a thin current sheet: Implications for patchy magnetopause reconnection, *J. Geophys. Res.*, *96*, 5859, 1991.
- Carreras, B., B. V. Waddell, and H. R. Hicks, Poloidal magnetic field fluctuations, *Nucl. Fusion*, *19*, 1423, 1979.
- Cheng, Q. C., J. E. Kan, and S.-I. Akasofu, Dependence of the region II field-aligned currents on the ionospheric conductivity gradients, *Planet Space Sci.*, *35*, 1405, 1987.
- Chiu, Y. T., and J. M. Cornwall, Electrostatic model of a quiet auroral arc, *J. Geophys. Res.*, *85*, 543, 1980.
- Coroniti, F. V., and C. F. Kennel, Magnetospheric reconnection, substorms, and energetic particle acceleration, in *Particle Acceleration Mechanisms in Astrophysics*, edited by J. Arons, C. Max and C. McKee, 169, American Institute of Physics, New York, 1979.
- Coroniti, F. V., and K. B. Quest, Nonlinear evolution of magnetopause tearing modes, *J. Geophys. Res.*, *89*, 137, 1984.
- Ding, D. Q., L. C. Lee, and Z. F. Fu, Multiple X line reconnection, 3: A particle simulation of flux transfer events, *J. Geophys. Res.*, *91*, 13384, 1986.
- Drake, J. F., and Y. C. Lee, kinetic theory of tearing instabilities, *Phys. Fluids*, *20*, 1341, 1977a.
- Drake, J. F., and Y. C. Lee, Nonlinear evolution of collisionless and semi-collisionless tearing modes, *Phys. Rev. Lett.*, *39*, 453, 1977b.
- Dungey, J. W., *Cosmic Electrodynamics*, p. 98, Cambridge University Press, 1958.

- Dungey, J. W., Interplanetary magnetic field and the auroral zones, *Phys. Rev. Lett.*, **6**, 47, 1961.
- Fadeev, V. M., I. F. Kvartskhava, and N. N. Komarov, *Nucl. Fusion*, **5**, 202, 1965.
- Farrugia, C. J., D. J. Southwood, S. W. H. Cowley, and R. P. Rijnbeek, Two-regime flux transfer events, *Planet. Space Sci.*, **35**, 737, 1987.
- Fejer, J. A., and J. R. Kan, A guiding center Vlasov equation and its application to Alfvén waves, *J. Plasma Phys.*, **3**, 331, 1969.
- Finn, J. M., and P. K. Kaw, Coalescence instability of magnetic islands, *Phys. Fluids*, **20**, 72, 1977.
- Formisano, V., and C. F. Kennel, Small Amplitude waves in high β plasmas, *J. Plasma Phys.*, **3**, 55, 1969.
- Frank, L. A., *J. Geophys. Res.*, **72**, 3753, 1967.
- Frank, L. A., and K. L. Ackerson, Observations of charged particle precipitation into the auroral zone, *J. Geophys. Res.*, **76**, 3612, 1971.
- Fridman, M., and J. Lemaire, Relationship between auroral electron fluxes and field-aligned electric potential deference, *J. Geophys. Res.*, **85**, 664, 1980.
- Furth, H. P., J. Killeen, and M. N. Rosenbluth, Finite-Resistivity instabilities of a sheet pinch, *Phys. Fluids*, **6**, 459, 1963.
- Furth, H. P., Hydromagnetic instabilities due to finite resistivity, *Propagation and Instabilities in Plasmas*, edited by W. I. Fetterman, p. 87, Stanford University Press, 1963.
- Galeev, A. A., Stationary magnetic field line reconnection in a tearing unstable plasma slab, *Phys. Fluids*, **21**, 1353, 1978.
- Gary, S. P., Low-frequency waves in a high-beta collisionless plasma: polarization, compressibility and helicity, *J. Plasma Physics*, **35**, 431, 1986.
- Gekelman, W., and H. Pfister, Experimental observations of the tearing of an electron current sheet, *Phys. Fluids*, **31**, 2017, 1988.
- Goertz, C. K., and R. W. Boswell, Magnetosphere-ionosphere coupling, *J. Geophys. Res.*, **84**, 7239, 1979.

- Haerendel, G., G. Paschmann, N. Sckopke, H. Rosenbauer, and P. C. Hedgecock, The frontside boundary layer and the problem of reconnection, *J. Geophys. Res.*, **83**, 3195, 1978.
- Hardy, D. A., M. S. Gussenhoven, R. Raistrick, and W. J. McNail, Statistical and functional representations of the pattern of auroral energy flux, number flux, and conductivity, *J. Geophys. Res.*, **92**, 12,275, 1987.
- Hardy, D. A., H. K. Hills, and J. W. Freeman, A new plasma regime in the distant geomagnetic tail, *Geophys. Res. Lett.*, **2**, 169, 1975.
- Harel, M., R. A. Wolf, P. H. Reiff, R. W. Spiro, W. J. Burke, F. J. Rich, and M. Smiddy, Quantitative simulation of a magnetospheric substorm 1. Model logic and overview, *J. Geophys. Res.*, **86**, 2217, 1981a.
- Harel, M., R. A. Wolf, R. W. Spiro, P. H. Reiff, C. K. Chen, W. J. Burke, F. J. Rich, and M. Smiddy, Quantitative simulation of a magnetospheric substorm 2: Comparison with observations, *J. Geophys. Res.*, **86**, 2242, 1981b.
- Hasegawa, A., and R. Sato, Generation of field aligned current during substorm, in *Dynamics of the Magnetosphere*, edited by S.-I Akasofu, p. 529, D. Reidel, Hingham, Mass., 1980.
- Hasegawa, A., and C. Uberoi, The Alfvén wave, *Rep. DOE/TIC11197*, U.S. Dep. of Commerce, Springfield, Va., 1982.
- Hassam, A. B., Collisional tearing in field-reversed configurations, *Phys. Fluids*, **27**, 2877, 1984.
- Heelis, R. A., The effects of interplanetary magnetic field orientation on dayside high-latitude ionospheric convection, *J. Geophys. Res.*, **89**, 2873, 1984.
- Heikkila, W. J., Magnetic reconnection, merging, and viscous interaction in the magnetosphere, *Space Sci. Rev.*, **53**, 1, 1990.
- Heppner, J. P., Empirical models of high latitude electric field, *J. Geophys. Res.*, **82**, 1115, 1977.
- Heppner, J. P., and N. C. Maynard, Empirical high latitude electric field models, *J. Geophys. Res.*, **92**, 4467, 1987.
- Hewett, D. W., G. E. Frances, and C. E. Max, New regimes of magnetic reconnection in collisionless plasmas, *Phys. Rev. Lett.*, **61**, 893, 1988.

- Hones, E. W., Jr., G. Paschmann, S. J. Bame, J. R. Asbridge, N. Sckopke, and K. Schindler, Vortices in magnetospheric plasma flow, *Geophys. Res. Lett.*, 5, 2069, 1978.
- Hones, E. W. Jr., J. Birn, S. J. Bame, and C. T. Russell, New observations of plasma vortices and insights into their interpretation, *Geophys. Res. Lett.*, 8, 674, 1983.
- Hoshino, M., The electrostatic effect for the collisionless tearing mode, *J. Geophys. Res.*, 92, 7368, 1987.
- Huba, J. N., N. T. Gladd, and J. F. Drake, On the role of the lower hybrid drift instability in substorm dynamics, *J. Geophys. Res.*, 86, 5881, 1981.
- Iijima, I., and I. A. Potemra, Large-scale characteristics of field-aligned currents associate with substorms, *J. Geophys. Res.*, 81, 3999, 1976.
- Kamide, Y., and S. Matsushita, Simulation studies of ionospheric electric fields and currents in relation to field-aligned currents, 2, Substorms, *J. Geophys. Res.*, 84, 4099, 1979.
- Kan, J. R., Nonlinear tearing structures in equilibrium current sheet, *Planet. Space Sci.*, 27, 351, 1978.
- Kan, J. R., Generation of field-aligned currents in magnetosphere-ionosphere coupling in a MHD plasma, *Planet Space Sci.*, 35, 903, 1987.
- Kan, J. R., A theory of patchy and intermittent reconnections for magnetospheric flux transfer events, *J. Geophys. Res.*, 93, 5613, 1988.
- Kan, J. R., and F. Cao, Effect of field-aligned potential drop in a global magnetosphere-ionosphere coupling model, *J. Geophys. Res.*, 93, 7571, 1988.
- Kan, J. R., D. U. Longnecker, and J. V. Olson, A transient response model of Pi 2 pulsations, *J. Geophys. Res.*, 87, 7483, 1982.
- Kan, J. R., and W. Sun, Simulation of the westward traveling surge and Pi 2 pulsations during substorms, *J. Geophys. Res.*, 90, 911, 1985.
- Kan, J. R., and Y. Kamide, Electrodynamics of the westward traveling surge, *J. Geophys. Res.*, 90, 7615, 1985.
- Kan, J. R., L. Zhu, and S.-I. Akasofu, A theory of substorms: Onset and subsidence, *J. Geophys. Res.*, 93, 5624, 1988.

- Karlson, E. T., Motion of charged particles in an inhomogeneous magnetic field, *Phys. Fluids*, 5, 476, 1962.
- Karlson, E. T., Streaming of a plasma through a magnetic dipole field, *Phys. Fluids*, 6, 708, 1963.
- Karty, J. L., R. A. Wolf, and R. W. Spiro, Region one Birkeland currents connecting to sunward convecting flux tubes, *Magnetospheric Currents, Geophys. Monograph*, vol. 28, p. 269, edited by T. A. Potemra, AGU, Washington, D. C., 1983.
- Katanuma, I., and T. Kamimura, Simulation studies of the collisionless tearing instabilities, *Phys. Fluids*, 23, 2500, 1980.
- Killeen, J., and I. Shestakov, Effect of equilibrium flow on the resistive tearing mode, *Phys. Fluids*, 21, 1746, 1978.
- Knight, S., Parallel electric fields, *Planet. Space Sci.*, 21, 741, 1973.
- Krall, N. A., and A. W. Trivelpiece, *Principles of Plasma Physics*, McGraw-Hill, New York, 1973.
- Kwok, Y. C., and L. C. Lee, Transmission of magnetohydrodynamic waves through the rotational discontinuity at the earth's magnetopause, *J. Geophys. Res.*, 89, 10,697, 1984.
- Landau, L. D., and E. M. Lifshitz, *Electrodynamics of Continuous Media*, Pergamon, New York, 1960.
- Lee, L. C., Transmission of Alfvén waves through the rotational discontinuity, *Planet. Space Sci.*, 30, 1127, 1982.
- Lee, L. C. and Z. Fu, A theory of magnetic flux transfer at the Earth's magnetopause, *Geophys. Res. Lett.*, 12, 105, 1985.
- Lee, L. C., and Z. F. Fu, Collisional tearing instability in the current sheet with a low magnetic Lundquist number, *J. Geophys. Res.*, 91, 3311, 1986.
- Lotko, W., and C. G. Schultz, Internal shear layers in auroral dynamics, in *Modeling Magnetospheric Plasma*, AGU Monogr. Ser., vol. 44, edited by T. E. Moore *et al.*, p. 121, AGU, Washington, D. C., 1988.
- Lotko, W., B. U. Ö. Sonnerup, and R. L. Lysak, Nonsteady boundary layer flow including ionospheric drag and parallel electric field, *J. Geophys. Res.*, 92, 8635, 1987.

- Lyons, L. R., Generations of large-scale regions of auroral currents, electric potentials and precipitation by the divergence of the convection electric field, *J. Geophys. Res.*, **85**, 17, 1980.
- Lysak, R. L., and C. T. Dum, Dynamics of magnetosphere-ionosphere coupling including turbulent transport, *J. Geophys. Res.*, **88**, 365, 1983.
- Lyu, L. H., and J. R. Kan, Structures of Alfvén shocks: S-shaped magnetic hodogram observed at the magnetopause, *Geophys. Res. Lett.*, **16**, 346, 1989.
- Mallinckrodt, A. J., and C. W. Carlson, Relations between transverse electric fields and field-aligned currents, *J. Geophys. Res.*, **83**, 1426, 1978.
- Maltsev, Y. P., S. V. Leovtyev, and W. B. Lyatsky, Pi-2 pulsations as a result of evolution of an Alfvén impulse origination in the ionosphere during a brightening of aurora, *Planet. Space Sci.*, **22**, 1519, 1974.
- Matthaeus, W. H., Rapid magnetic reconnection caused by finite amplitude fluctuations, *Phys. Fluids*, **28**, 33, 1985.
- Matthaeus, W. H., and D. Montgomery, Nonlinear evolution of the sheet pinch, *J. Plasma Physics*, **25**, 11, 1981.
- McKenzie, J. F., Hydromagnetic wave interaction with the magnetopause and the bow shock, *Planet. Space Sci.*, **18**, 1, 1970.
- McKenzie, J. F., and K. O. Westphal, Interaction of hydromagnetic waves with hydromagnetic shocks, *Phys. Fluids*, **13**, 630, 1970.
- Miura, A., and T. Sato, Numerical simulation global formation of auroral arcs, *J. Geophys. Res.*, **85**, 73, 1980.
- Miura, A., S. Ohtani, and T. Tamao, Ballooning instability and structure of diamagnetic hydromagnetic waves in a model magnetosphere, *J. Geophys. Res.*, 1990.
- Nisbet, J. S., M. J. Miller, and L. A. Carpenter, Currents and electric fields in the ionosphere due to field-aligned auroral currents, *J. Geophys. Res.*, **83**, 2647, 1978.
- Nishida, A., Can random reconnection on the magnetopause produce the low latitude boundary layer? *Geophys. Res. Lett.*, **16**, 227, 1989.

- Norris, J., The nonlinear saturation of a magnetic island, *Plasma Phys. Contr. Fusion* 31, 699, 1989.
- Paschmann, G., G. Haerendel, N. Sckopke, H. Rosenbauer, and P. C. Hedgecock, Plasma and magnetic field characteristics of the distant polar cusp near local noon: The entry layer, *J. Geophys. Res.*, 81, 2883, 1976.
- Pellat, R., Coalescence of magnetic islands, *Sov. J. Plasma Phys.*, 9, 124, 1983.
- Price, C. P., and D. W. Swift, Ion tearing mode simulations with open boundary conditions, *J. Geophys. Res.*, 91, 11993, 1986.
- Priest, E. R., The magnetohydrodynamics of current sheet, *Rep. Prog. Phys.*, 48, 955, 1985.
- Pritchett, P. L., and C. C. Wu, Coalescence of magnetic islands, *Phys. Fluids*, 22, 2140, 1979.
- Quest, K. B., and F. V. Coroniti, Tearing at the dayside magnetopause, *J. Geophys. Res.*, 86, 3289, 1981.
- Quest, K. B., and F. V. Coroniti, Collisional tearing in a field-reversed sheet pinch assuming nonparallel propagation, *J. Geophys. Res.*, 90, 1469, 1985.
- Rijnbeek, R. P., S. W. H. Cowley, D. J. Southwood, and C. T. Russell, A survey of dayside flux transfer events observed by ISEE 1 and 2 magnetometers, *J. Geophys. Res.*, 89, 786, 1984.
- Rosenbauer, H., H. Grünwaldt, M. D. Montgomery, G. Paschmann, and N. Sckopke, Heos 2 plasma observations in the distant polar magnetosphere: the plasma mantle, *J. Geophys. Res.*, 80, 2723 1975.
- Rostoker, G., and T. Eastman, A Boundary layer model for magnetospheric substorms, *J. Geophys. Res.*, 92, 12,187, 1987.
- Russell, C. T., and R. C. Elphic, Initial ISEE magnetometer results: Magnetopause observations, *Space Sci. Rev.*, 22, 681, 1978.
- Russell, C. T., and R. C. Elphic, ISEE observations of flux transfer events at the dayside magnetopause, *J. Geophys. Res.*, 6, 33, 1979.
- Rutherford, P. H., Nonlinear growth of the tearing mode, *Phys. Fluids*, 16, 1903, 1977.

- Sanchez, E. R., and G. L. Siscoe, Observations of rotational discontinuity- slow expansion fan structure of the magnetotail boundary, *J. Geophys. Res.* 95, 61, 1990a.
- Sanchez, E. R., et al., Downstream evolution of an open MHD magnetotail boundary, to be published, 1990.
- Sato, T., and T. Iijima, Primary sources of large-scale Birkeland currents, *Space Sci. Rev.*, 24, 347, 1979.
- Saunders, M. A., C. T. Russell, and N. Sckopke, Flux transfer events: Scale size and interior structure, *Geophys. Res. Lett.*, 11, 131, 1984.
- Saunders, M. A., D. J. Southwood, E. W. Jr. Hones, and C. T. Russell, A hydromagnetic vortex seen by ISEE 1 and 2., *J. Atmos. Terr. Phys.*, 43, 297, 1981.
- Saunders, M. A., D. J. Southwood, T. A. Fritz, E. W. Jr. Hones, Hydromagnetic vortices I: The 11 December 1977 event, *Planet. Space Sci.*, 31, 1099, 1983.
- Schild, M. A., J. W. Freeman, and A. J. Dessler, A source for field-aligned currents at auroral latitudes, *J. Geophys. Res.*, 74, 247, 1969.
- Scholer, M., On the motion of artificial ion clouds in the magnetosphere, *Planet. Space Sci.*, 18, 977, 1970.
- Scholer, M., and D. Roth, A simulation study on reconnection and small-scale plasmoid formation, *J. Geophys. Res.*, 92, 3223, 1987.
- Sckopke, N., and G. Paschmann, The plasma mantle. A survey of magnetotail boundary layer observations, *J. Atmos. Terr. Phys.*, 40, 261, 1978.
- Senior, C., and M. Blanc, On the control of magnetospheric convection by the spatial distribution of ionospheric conductivities, *J. Geophys. Res.*, 89, 261, 1984.
- Shi Y., C. C. Wu, and L. C. Lee, A study of multiple X line Reconnection at the dayside magnetopause, *Geophys. Res. Lett.*, 15, 295, 1988.
- Sibeck, D. G., and G. L. Siscoe, Magnetic field properties of the distant magnetotail magnetopause and boundary layer, *J. Geophys. Res.*, 90, 9561, 1985.
- Siscoe, G. L., and E. Sanchez, An MHD model for the complete open magnetotail boundary, *J. Geophys. Res.*, 92, 7405, 1987.

- Sonnerup, B. U. O., Magnetopause field reconnection, *Solar System Plasma Physics*, edited by C. F. Kennel, L. J. Lanzerotti and E. N. Parker, 3, 45, North-Holland Pub., 1979.
- Sonnerup, B. U. Ö., Theory of the low-latitude boundary layer, *J. Geophys. Res.*, 85, 2017, 1980.
- Sonnerup, B. U. O., and B. G. Ledley, OGO 5 magnetopause structure and classical reconnection, *J. Geophys. Res.*, 84, 399, 1979.
- Sonnerup, B. U. O., G. Paschmann, I. Papamastorakis, N. Sckopke, G. Haerendel, S. J. Bame, J. R. Asbridge, J. T. Gosling, and C. T. Russell, Evidence for magnetic field reconnection at the earth's magnetopause, *J. Geophys. Res.*, 86, 10,049, 1981.
- Southwood, D. J., The role of hot plasma in magnetospheric convection, *J. Geophys. Res.*, 82, 5512, 1977.
- Southwood, D. J., and M. A. Saunders, Courvature coupling of slow and Alfvén MHD waves in a magnetotail field configuration, *Planet. Space. Sci.*, 33, 127, 1985.
- Stéfant, R. J., Alfvén wave damping from fluids gyroradius coupling to the ion acoustic mode, *Phys. Fluids*, 13, 440, 1970.
- Steinolfson, R. S., and G. Van Hoven, Nonlinear evolution of the resistive tearing mode, *Phys. Fluids*, 27, 1207, 1984.
- Stepanov, K. N., Kinetic theory of magnetohydrodynamic waves, *Sov. Phys. JEPT*, 34, 892, 1958.
- Stix, T. H. *The Theory of Plasma Waves*, McGraw-Hill, New York, 1962.
- Stringer, T. E., Low-frequency waves in An unbounded plasma, *Plasma Phys.*, 5, 89, 1963.
- Sugiura, M., T. Iyemori, R. A. Hoffman, N. C. Maynard, J. L. Burch, and J. D. Winningham, Relationships between field-aligned currents, electric fields, and particle precipitation as observed by Dynamic Explorer-2, *Magnetospheric Currents, Geophys. Monograph*, vol. 28, p. 96, edited by T. A. Potemra, AGU, Washington, D. C., 1983.
- Swift, D. W., Numerical simulation of tearing mode instabilities, *J. Geophys. Res.*, 91, 219, 1986.
- Swift, D. W., and L. C. Lee, The magnetotail boundary and energy transfer process, *Geophys. Res. Lett.*, 9, 527, 1982.

- Swift, D. W., and L. C. Lee, Rotational discontinuities and the structure of the magnetopause, *J. Geophys. Res.*, **88**, 527, 1983.
- Taktakishvili, A. L., and L. M. Zeleny, Merging instability of magnetic islands, *Proceedings of the Joint Varenna-Abastumani International School & Workshop on PLASMA ASTROPHYSICS*, published by the European Space Agency, August 1986.
- Terasawa, T., Hall current effect on tearing mode instability, *Geophys. Res. Lett.*, **10**, 475, 1983.
- Thyagaraja, A., Perturbation analysis of a simple model of magnetic island structures, *Phys. Fluids*, **24**, 1716, 1981.
- Troshichev, O. A., Polar magnetic disturbances and field-aligned currents, *Space Sci. Rev.*, **32**, 275, 1982.
- Vasyliunas, V. M., Mathematical models of magnetospheric convection and its coupling to the ionosphere, in *Particles and Fields in the Magnetosphere*, edited by B. McCormac, p. 60, D. Reidel, Hingham, Mass., 1970.
- Vasyliunas, V. M., The interrelationship of magnetospheric processes, in *Earth's Magnetospheric Processes*, edited by B. McCormac, p. 29, D. Reidel, Hingham, Mass., 1972.
- Vasyliunas, V. M., Theoretical models of magnetic field line merging, 1, *Rev. Geophys. Space Phys.*, **13**, 303, 1975.
- Vasyliunas, V. M., Fundamentals of current description, in *Magnetospheric Currents, AGU Monogr. Ser.*, vol. 28, edited by T. A. Potemra, p. 63, AGU, Washington, D.C., 1984.
- Verzariu, P., Reflection and refraction of hydromagnetic waves at the magnetopause, *Planet. Space Sci.*, **21**, 2213, 1973.
- Weimer, D. R., C. K. Goertz, D. A. Gurnett, N. C. Maynard, and J. L. Burch, Auroral zone electric fields from DE 1 and 2 at magnetic conjunctions, *J. Geophys. Res.*, **90**, 7479, 1985.
- Weimer, D. R., D. A. Gurnett, C. K. Goertz, J. D. Menietti, J. L. Burch, and M. Sugiura, The current-voltage relationship in auroral current sheets, *J. Geophys. Res.*, **92**, 187, 1987.
- White, R. B., Resistive Reconnection, *Rev. Modern Phys.*, **58**, 183, 1986.
- White, R. B., D. A. Monticello, M. N. Rosenbluth, and B. V. Waddell, *Phys. Fluids*, **20**, 800, 1977.

- Winske, D., and S. P. Gary, and A. G. Sgro, Microinstabilities and diffusive transport at the magnetopause, 1990 Cambridge Workshop on *Magnetic Fluctuations, Diffusion and Transport in Geoplasmas*, 1990.
- Wolf, R. A., Ionosphere-magnetosphere coupling, *Space Sci. Rev.*, *17*, 537, 1975.
- Wolf, R. A., M. Harel, R. W. Spiro, G. H. Voigt, P. H. Reiff, and C. K. Chen, Computer simulation of inner magnetospheric dynamics for the magnetic storm of July 29, 1977, *J. Geophys. Res.*, *87*, 5949, 1982.
- Wolfe, A., and R. L. Kaufmann, MHD wave transmission and production near the magnetopause, *J. Geophys. Res.*, *80*, 1764, 1975.
- Yasuhara, F., R. Greenwald, and S.-I. Akasofu, On the rotation of the polar cap potential pattern and associated polar phenomena, *J. Geophys. Res.*, *88*, 5773, 1983.